

Dual-Energy Electromagnetic Modeling, with Application to Variable Reluctance Motor Analysis

by

Mary Tolikas

B.ENG., UNIVERSITY OF GLASGOW, 1990
S.M., MASSACHUSETTS INSTITUTE OF TECHNOLOGY, 1992
E.E., MASSACHUSETTS INSTITUTE OF TECHNOLOGY, 1993

Submitted to the Department of Electrical Engineering and Computer Science
in Partial Fulfillment of the Requirements for the Degree of

DOCTOR OF PHILOSOPHY

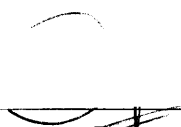
at the

MASSACHUSETTS INSTITUTE OF TECHNOLOGY

August 1995

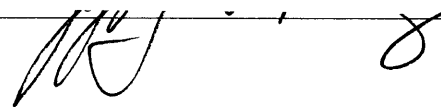
©1995 Massachusetts Institute of Technology
All rights reserved

Signature of Author



Department of Electrical Engineering and Computer Science

August 11, 1995

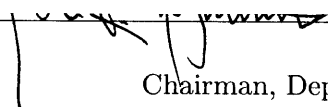
Certified by


Professor Jeffrey H. Lang
Thesis Supervisor

Certified by


Professor James L. Kirtley Jr.
Thesis Supervisor

Accepted by


Professor Frederick R. Morgenthaler
Chairman, Department Committee on Graduate Students

MASSACHUSETTS INSTITUTE
OF TECHNOLOGY

Barker Eng

NOV 02 1995

LIBRARIES

Dual-Energy Electromagnetic Modeling, with Application to Variable Reluctance Motor Analysis

by

Mary Tolikas

Submitted to the Department of Electrical Engineering and Computer Science
on August 11, 1995 in Partial Fulfillment of the Requirements for the Degree of Doctor of
Philosophy in Electrical Engineering

ABSTRACT

The design of electric motor drives requires accurate motor analysis to support the accurate prediction of drive performance. Currently, the most widely applied method of motor analysis is the finite-element method. Its advantage lies in the fact that arbitrarily shaped problems consisting of a variety of materials can be analyzed. However, dense discretization is necessary for accurate geometry representation and accurate analysis. The requirement for fine discretization has a direct impact on computational speed and time. In contrast, this thesis explores the application of the algebraic dual-energy method (ADEM) to the magnetic and thermal analysis of the variable reluctance motor (VRM). The motivation for considering the ADEM comes from its potential to offer both computational accuracy and speed. The goal of this thesis is not the development of sophisticated design models. Rather, given an acceptable magnetic or thermal model, emphasis is herein placed on its analysis, and more specifically on the applicability and performance of the ADEM in performing this task.

The algebraic dual-energy method is first employed in simple problems with known analytic solutions, in order to gain better understanding on the application, convergence behavior and issues associated with the method. The ADEM is then applied to the calculation of the stored magnetic energy of a simplified VRM geometry at the unaligned position. By simply averaging upper and lower energy bounds, energy and inductance values are accurately computed using a small number of degrees of freedom. Analytic expressions for the bounds are obtained using a symbolic manipulation package and these expressions can be translated into C to extract the minimum inductance of a motor in fractions of a second. The issue of equidistance of the bounds from the true solution is critical in the success of the method and is addressed in the thesis. The algebraic p-convergence of the method is shown to provide a criterion that guarantees that the distances of the upper and lower inductance bounds from the exact inductance value are approximately equal.

The ADEM is extended to the thermal analysis of the VRM. By employing the analogy that exists between electrostatics and steady-state heat conduction, bounds on the “thermal energy” of the system are shown to exist and are derived for several numerical examples. Bounding this energy does not guarantee bounds on the field quantities at each point in the geometry. Nonetheless, a simple algorithm is presented that uses the upper and lower “thermal energy” bounds of the ADEM to estimate the hot spot temperature of the VRM.

Thesis Supervisors: Jeffrey H. Lang, Professor of Electrical Engineering
James L. Kirtley Jr., Professor of Electrical Engineering

ACKNOWLEDGMENTS

I wish to thank Professors Jeffrey H. Lang and James L. Kirtley Jr. for supervising this work and for their guidance and constant encouragement over the last three years. I thank Prof. Jacob White for Reading the thesis; without his support and suggestions over the last six months this thesis would not have been completed. I thank the General Motors Research & Development Center, Warren, MI, and Delphi, Energy and Engine Management Systems, for financially supporting the majority of this work. I acknowledge the financial support of Lincoln Laboratories and ARPA Grant Number: J-FBI-92-196. I thank Ms. Karen Walrath for providing answers and alternatives when the computing facilities just seemed inadequate. I thank Ms. Vivian Mizuno, Ms. Barbara Connolly and Ms. Kathy McCue for helping me through all administrative panics and Ms. Marilyn Pierce, Ms. Peggy Carney and Ms. Monica Bell in the EECS Graduate Office for their support since my first day at MIT.

The development of a variable reluctance motor drive has motivated most of the work in this thesis, and has been a large part of the PhD experience. I thank my supervisors for guiding me through all the steps from design to implementation and testing. I am indebted to Mr. Wayne Ryan for all his technical support, machine-shop lectures and encouragement and to Prof. Steven B. Leeb for providing equipment and technical suggestions. I thank everyone at the Electrical & Electronics Department at GM, especially Dr. Nady Boules, Dr. Thomas Nehl, Dr. Aravind Bharadwaj and Mr. Randall Shafer for guiding me through the practical aspects of motor drive design and development.

My parents Stefanos and Carmen, and my brother Costas, have been my strongest supporters through nine years of adjusting to new cultures and facing new challenges. My gratitude, love and respect are extended to them for their continuous encouragement in the pursuit of my dream, and for their patience across the ocean.

My sincerest thanks and respect are also extended to Vivian Mizuno and Lisa Pickelsimer for their friendship and constant support through good and bad times. The LEES lab has been my second home over the last five years. It has been a privilege to have been a member of its community, to have met, worked and interacted with all its people. In particular, I want to thank my officemates Jeff Chapman and Joaquin Lacalle Melero for their stimulating discussions on power systems that I never understood, for putting up with my expensive taste in coffee, but more importantly for taking the time to listen. I thank Karen Walrath and Jeff Schiller for running their bread machine day and night for me, but also for making me feel welcome at their home. I am indebted to Barbara Connolly for providing the daily hugs and to Kathy McCue for sharing her insights on how to fight stress at MIT. I thank Kamakshi Sridhar and Marc Thompson for their encouragement, as well as their help on electromagnetics. Special thanks are also due to Wayne Hagman, John Ofori, Tracy Clark, Dave Perreault and Dr. Steve Umans for providing answers and suggestions of more practical nature. I thank Constantinos Boussios, George Kardaras, Yehia Massoud, Hsiou-Ping (Vincent) Chou, Prof. Pei-Hwa Huang, Dr. Ganesh Ramaswamy, Prof. Richard Tabors, Ahmed Mitwalli, Liana Alvarez, Julio Castrillon, Brian Eidson, and Ujjwal Sinha for their support all the way to the finish line.

Above all, I thank God.

Contents

- 1 Introduction 7**
 - 1.1 Motivation 7
 - 1.2 The Variable Reluctance Motor Drive 8
 - 1.3 Variable Reluctance Motor Analysis 12
 - 1.3.1 Minimum Inductance Calculation 12
 - 1.3.2 Hot Spot Estimation 13
 - 1.4 The Dual-Energy Method 14
 - 1.5 Thesis Objectives 18
 - 1.6 Thesis Organization 19

- 2 The Algebraic Dual-Energy Method 20**
 - 2.1 Introduction 20
 - 2.2 Resistance Estimation Using the ADEM 21
 - 2.2.1 Existence of Upper and Lower Resistance Bounds 22
 - 2.2.2 Example: Right-Angled Conductor 26
 - 2.3 Capacitance Estimation Using the Algebraic Dual-Energy Method . . 36
 - 2.3.1 Existence of Upper and Lower Capacitance Bounds 36
 - 2.4 Inductance Estimation Using the Algebraic Dual-Energy Method . . . 41
 - 2.4.1 Existence of Upper and Lower Inductance Bounds 41
 - 2.4.2 Application of the ADEM to Inductance Computation 45
 - 2.4.3 Example: T-inductor 48
 - 2.4.4 Example: Slot with Perfectly Conducting Walls 52

2.5	Further Thoughts on the Application of the Algebraic Dual-Energy Method	56
2.6	Appendix A: Maple Code for Resistance Bounds Calculation	58
2.7	Appendix B: Capacitance Bounds for Tubular Capacitor	59
2.8	Appendix C: Maple Code for T-slot Inductance Upper Bound Calculation	67
3	Minimum Inductance of the VRM	72
3.1	The Minimum Inductance Problem	72
3.2	The Minimum Inductance Model	74
3.2.1	The VRM Model in $x-y$ Coordinates	74
3.2.2	Error Analysis	81
3.2.3	The VRM Model in $r - \theta$ Coordinates	89
3.3	Conclusions	98
3.4	Appendix A: Integration Over a Quadrilateral Element	99
3.4.1	The Algorithm	99
3.4.2	Maple V Algorithm	100
3.5	Appendix B: Generation of Inter-Element Continuity	106
4	Thermal Analysis of the VRM	108
4.1	The Steady-State Heat Conduction Problem and its Analogy to Electrostatics	108
4.2	The dual-energy method extended to the thermal problem	110
4.2.1	Derivation of upper and lower thermal energy bounds	111
4.3	The VRM Thermal Problem	115
4.3.1	The VRM Thermal Model	115
4.4	Hot Spot Temperature Estimation	132
4.5	VRM Hot Spot Estimation Using the ADEM	133
4.6	Conclusions	140
5	Summary, Conclusions and Suggestions for Future Work	141
5.1	Thesis Summary	141

5.2	Thesis Conclusions	142
5.3	Suggestions for Future Work	145

List of Figures

1-1	Cross-section of a three-phase VRM	9
1-2	Variation of phase inductance with rotor position (ideal case)	10
1-3	Block diagram of the VRM drive	11
1-4	Typical magnetization curves for one phase of a VRM	12
2-1	Graphical interpretation of the algebraic dual energy method	21
2-2	Arbitrary resistor definition	22
2-3	Right-angled resistor problem	29
2-4	Resistance bounds vs. order of approximation	34
2-5	Resistance bounds vs. number of free coefficients	35
2-6	Arbitrary capacitor definition	37
2-7	General inductor definition	41
2-8	Geometry of the T-inductor problem	48
2-9	Six-element discretization for the T-slot problem	51
2-10	Rectangular slot with perfectly conducting walls	53
2-11	Field plot for rectangular slot with perfectly conducting walls	54
2-12	Tubular capacitor problem	62
3-1	Minimum inductance topology for phase A	73
3-2	Simplified VRM model in x-y coordinates	75
3-3	Single region representation for lower bound calculation	76
3-4	Subdivision for upper bound calculation	78
3-5	Energy bounds convergence to FEA solution	83

3-6	Error variation with increasing number of coefficients for upper bound. The parameter p defines the order of polynomial approximation. . . .	84
3-7	Error variation with increasing number of coefficients for lower bound. The parameter p defines the order of polynomial approximation. . . .	85
3-8	Error variation for varying number of elements in the p -extension . . .	88
3-9	The VRM geometry in polar coordinates	90
3-10	Minimum inductance model definition	91
3-11	Minimum inductance model definition	92
3-12	Field distribution for VRM model with curved boundaries	93
3-13	Field distribution for VRM model with straight boundaries	93
3-14	Element subdivision of the VRM model	95
3-15	Field continuity along element interface	96
3-16	Quadrilateral element in the $x - y$ coordinate system	99
4-1	Geometry definition for “thermal energy” bounds generation	111
4-2	Simplified geometry of a 6:4 VRM for thermal analysis	116
4-3	Simplified geometry of a 6:4 VRM for thermal analysis	117
4-4	Subdivision of geometry for upper bound calculation	120
4-5	“Thermal energy” bounds convergence to FEA solution	129
4-6	Error variation for upper “thermal energy” bound	130
4-7	Error variation for lower “thermal energy” bound	131
4-8	Heat flux vector plot for the simplified VRM geometry	133
4-9	Temperature map for the simplified VRM geometry, showing a varia- tion of 0-21.5K in steps of 2.15K. The darkest region is the hottest. . .	134
4-10	Isotherms for the simplified VRM geometry	135
4-11	The VRM model as a black box	136
4-12	Sample of various VRM geometries considered in hot spot calculations	137

List of Tables

1.1	Boundary value problems in different engineering disciplines	14
2.1	Resistance bounds for the right-angled conductor problem	33
2.2	Lower energy bounds for rectangular slot problem	55
2.3	Upper energy bounds for rectangular slot problem	55
3.1	Geometric and excitation values for inductance problem	80
3.2	Coordinates of the basic VRM geometry points	90
3.3	Geometric and excitation values for VRM geometry	92
4.1	Analogy between steady-state heat conduction and electrostatics	110
4.2	Geometric and excitation values for thermal model	127
4.3	Geometry A: Hot spot and “thermal energy” predictions using the ADEM	138
4.4	Geometry B: Hot spot and “thermal energy” predictions using the ADEM	138
4.5	Geometry C: Hot spot and “thermal energy” predictions using the ADEM	138

Chapter 1

Introduction

This chapter introduces dual-energy numerical analysis as presented and discussed in this thesis, and outlines the issues and challenges involved in the development of fast and accurate algebraic dual-energy analyses of variable-reluctance motors. First, the motivation for the thesis is given, together with a theoretical background of the structure and operation of variable-reluctance motor drives. Next the research challenges addressed herein are presented. These are directed towards two motor analyses: electromagnetic, involving the calculation of minimum motor phase inductance, and thermal, involving the estimation of the hot spot in a phase. Moreover, a brief introduction is given to the numerical analyses which are available and most frequently applied to the solution of variable-reluctance motor modeling problems. Emphasis is placed on the dual-energy method, which has already been successfully applied in simple linear resistance, capacitance and inductance calculations. Finally, the thesis objectives are defined.

1.1 Motivation

The design of electric motor drives requires the accurate determination of motor parameters and the prediction of the drive performance, subject to the specifications imposed by the application at hand. Monte Carlo synthesis has been applied in the last few years to the design of electric motor drives, including variable-reluctance

motor drives [1], [2]. This involves the random generation of a large number of candidate motor designs over short periods of time. Every new design is analyzed, based on fast and accurate thermal, mechanical, magnetic and electronic models. If the electromechanical performance of a candidate drive does not meet the imposed specifications then the design is discarded. Otherwise, the new design is compared to previous designs, based on the rules of multi-attribute dominance and only the best drives are retained. The output of this process is a feasibility frontier of superior designs that allows the motor designer to select an optimal motor drive within the design space.

Achieving an optimal motor drive design is not only dependent on comprehensive specifications. The design should be practical and implementable and this implies that the models adopted for its analysis and performance prediction should possess sufficient accuracy. In addition, model analysis must be fast since it is repeated many times. It is therefore crucial to develop algorithms that will be accurate enough to reflect reality, flexible enough to handle any geometry and possible specifications, and simple and hence fast enough to be incorporated in a Monte Carlo design-optimization framework. This will allow the evaluation of a very large number of candidate designs in short design time frames.

1.2 The Variable Reluctance Motor Drive

The Variable Reluctance Motor (VRM) has become increasingly popular in recent years [4], [5]. Advances in power electronics and computers have enabled the design, development and implementation of VRM drives that perform comparably to other drives. High speed and high starting torque are among the many advantages of a VRM which is finding wide application in adjustable speed drives. Simple motor and inverter construction have a direct effect on cost and reliability surpassing those of other drives. Among its most important disadvantages however, are those of high audible noise, high torque ripple under open-loop control and a requirement for a very small airgap [3].

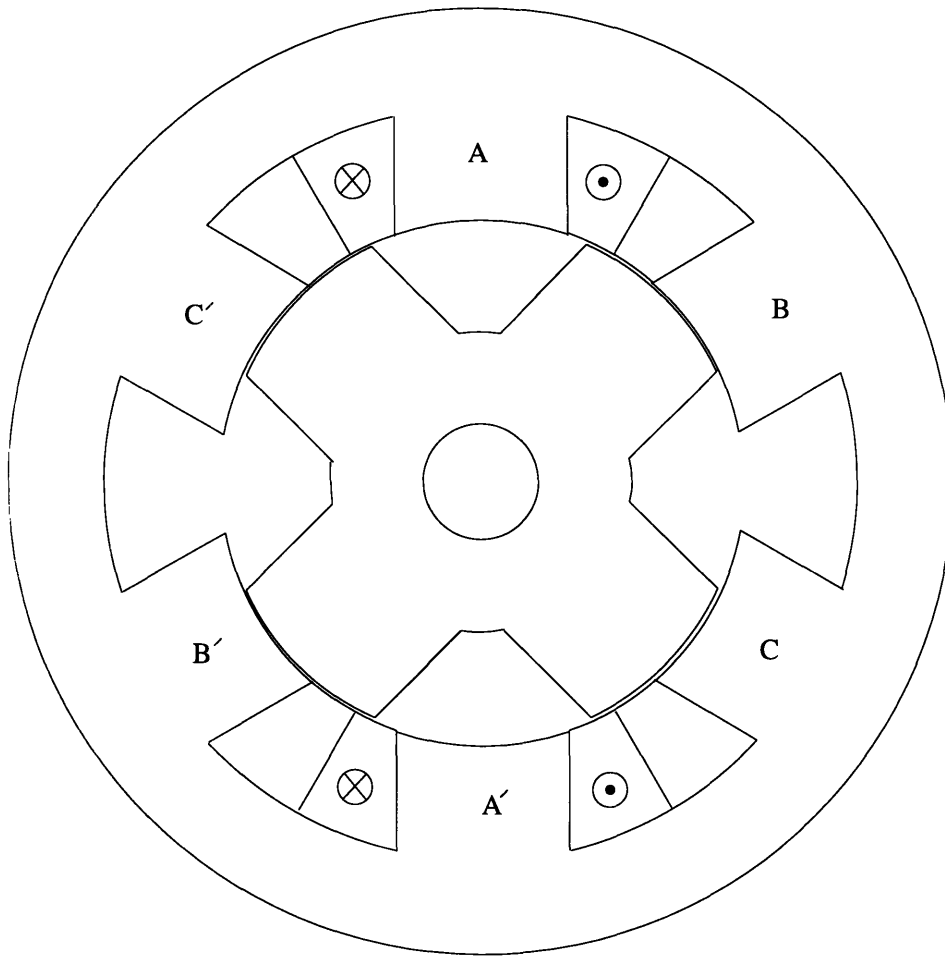


Figure 1-1: Cross-section of a three-phase VRM

The cross-section of a typical three-phase VRM is shown in Figure 1-1. Simple construction, double saliency and the presence of winding excitation only on the stator are the most characteristic features of such a motor. Diametrically opposite stator poles carry coils connected in series, defining a phase. When current is applied to a phase winding, the stator and rotor are both magnetized with opposing polarity, resulting in forces with both radial and tangential components. The radial components result in vibration of the stator frame and are the primary source of audible noise. The tangential components produce torque and result in rotor rotation, tending to align the neighboring rotor poles with the excited stator poles. Sequential excitation of the stator phases achieves continuous rotation.

As the rotor rotates, the inductance L of each phase varies between two extreme

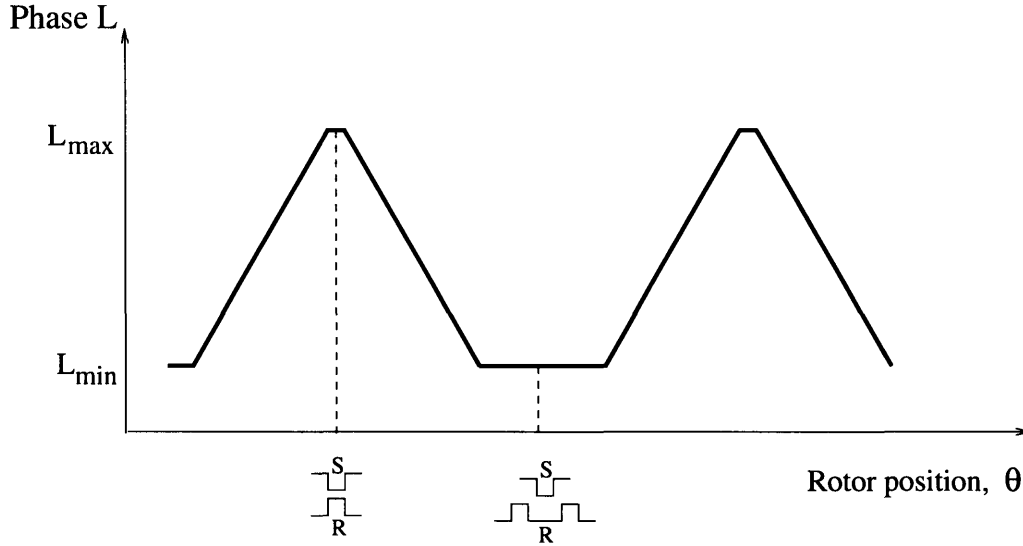


Figure 1-2: Variation of phase inductance with rotor position (ideal case)

values. This is illustrated in Figure 1-2, for the ideal case where no saturation is present; the minimum inductance occurs when the rotor interpolar axis is aligned with the stator poles, while the maximum occurs when the stator and rotor poles are aligned.

The instantaneous torque produced by the motor is given by [5]

$$T(\theta, i) = \left. \frac{\partial W'(\theta, i)}{\partial \theta} \right|_{i=\text{constant}} \quad (1.1)$$

where $W'(\theta, i)$ is the winding coenergy given by

$$W'(\theta, i) = \int_0^i \psi(\theta, i') \, di'. \quad (1.2)$$

Assuming a magnetically linear motor,

$$W' = \frac{1}{2} L i^2 \quad (1.3)$$

so that

$$T(\theta, i) = \frac{1}{2} i^2 \frac{dL}{d\theta}. \quad (1.4)$$

Hence, for motoring operation, current should be on during the interval where the inductance is increasing.

Figure 1-3 is a block diagram of a VRM drive. The DC supply voltage is switched across the windings of the motor, according to an appropriate switching sequence of the inverter. Control of a VRM amounts to ensuring phase currents occur at specific rotor angles in order to achieve continuous torque. As a result, switching is synchronized by the controller, based on the rotor shaft position and preset current chopping levels. Four parameters are critical in controller operation: the turn-on

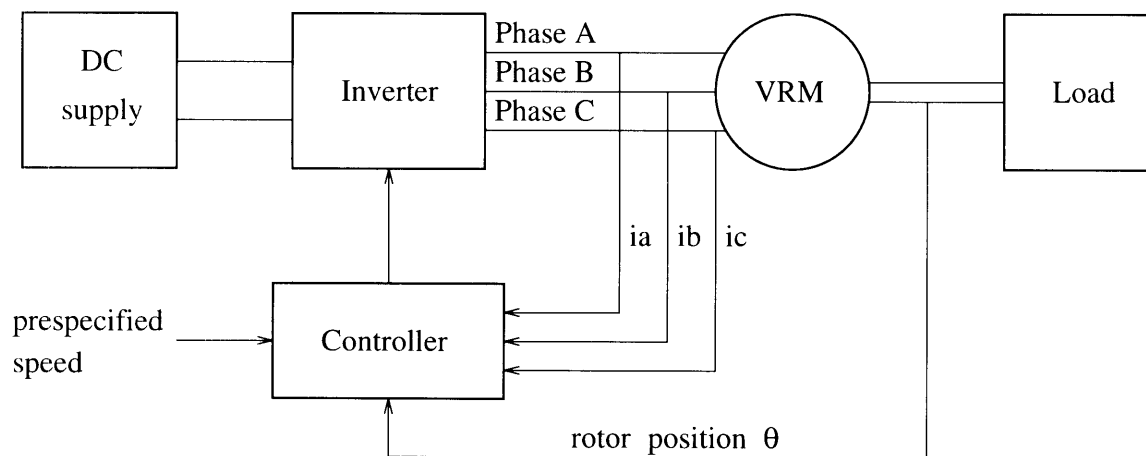


Figure 1-3: Block diagram of the VRM drive

angle, θ_{on} ; the turn-off angle, θ_{off} ; the chopping current level; and the supply voltage. The angles θ_{on} and θ_{off} define the position of the current pulse within a cycle of inductance variation. At low speeds, current control is employed by maintaining the current between upper and lower levels. The level of the supply voltage determines the rise and fall times of the phase current, constraining the values of θ_{on} and θ_{off} , the peak value that the current can reach during conduction, as well as the maximum speed that the VRM can attain [4], [5], [6].

1.3 Variable Reluctance Motor Analysis

The VRM analysis challenges considered in this thesis are the computation of minimum inductance, and the estimation of the hot-spot temperature of a phase. These issues are considered in more detail in the following sections.

1.3.1 Minimum Inductance Calculation

The flux linkage of each phase, $\lambda(\theta, i)$, is a nonlinear function of the current through the winding, due to magnetic saturation at high current levels, and varies periodically with rotor position. Figure 1-4 provides typical magnetization curves for each phase. Accurate determination of these characteristics is essential during VRM design in order to predict electromechanical performance. In particular, the accurate calculation of the minimum phase inductance, L_{min} , is critical to the prediction of this performance. It also affects the estimation of the peak currents present in the motor windings and hence the size and cost of the inverter switches.

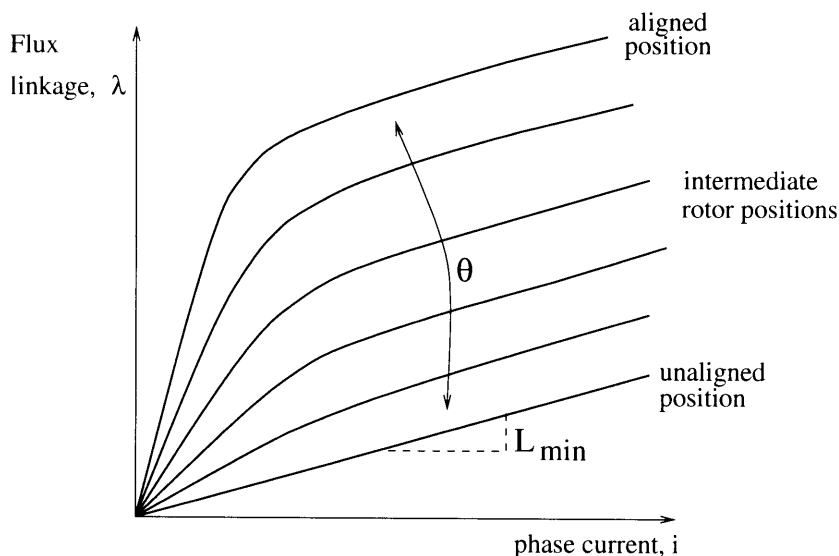


Figure 1-4: Typical magnetization curves for one phase of a VRM

The calculation of L_{min} is achieved by solution of Maxwell's equations in the motor topology at the unaligned position. A closed form expression for the magnetic field

distribution does not exist and is hard to find, due to the complicated geometry, the presence of the source and the large number of boundary conditions along the steel stator and rotor surfaces. As a result, one has to resort to numerical methods, with the finite element method being the most popular one in analyzing motor geometries. This is in contrast to the analysis of the flux linkage at alignment, which is done using simple magnetic circuit techniques.

A method that has been employed in the past in the calculation of the three-dimensional resistance, inductance and capacitance of arbitrary geometries is the dual-energy method [7]. A version of this approach, called “the method of tubes and slices”, has been successfully applied by Miller [8] to the calculation of minimum inductance of VRM geometries. The basic theory and philosophy of this method are presented in the next section in more detail.

1.3.2 Hot Spot Estimation

Accurate thermal modeling is important for the prediction of the highest temperature of the motor, allowing for an appropriate cooling scheme to be adopted, for losses in various motor parts to be accounted for and for the rating of the motor to be accurately determined. A traditional approach to such a problem is the discretization of the geometry cross-section in finite elements and the calculation of the temperature distribution, by minimization of an appropriate functional. Knowledge of the temperature distribution throughout the geometry would immediately imply knowledge of the hottest point. However, the finite element method does not provide the speed and flexibility essential for Monte-Carlo design and an alternative is necessary.

Another path is followed here that employs dual-energy analysis in the calculation of the hot spot. The motivation comes from the analogy that exists between the steady-state heat conduction equations and the electrostatic Maxwell’s equations. Following this analogy, appropriate functionals may be obtained that lead to the estimation of upper and lower bounds to the “thermal energy” of the variable reluctance machine cross-section. The dual-energy algorithm is extended to the estimation of the temperature at the hot spot of the VRM model.

1.4 The Dual-Energy Method

The VRM design problems considered in this thesis are mathematically described by a set of partial differential equations, subject to Dirichlet and Neumann boundary conditions. These problems fall under the general category of boundary value problems, which encompasses a wide range of engineering disciplines. Table 1.1 provides a chart of several such disciplines, and illustrates the similarities that exist between their describing equations. In all these cases, the boundary value problems consist

Magnetic	$\nabla \cdot \mathbf{B} = 0$	$\nabla \times \mathbf{H} = \mathbf{J}$	$\mathbf{B} = \mu \mathbf{H}$
Electrostatic	$\nabla \cdot \mathbf{D} = \rho$	$\nabla \times \mathbf{E} = \mathbf{0}$	$\mathbf{D} = \epsilon \mathbf{E}$
Conduction	$\nabla \cdot \mathbf{J} = 0$	$\nabla \times \mathbf{E} = \mathbf{0}$	$\mathbf{J} = \sigma \mathbf{E}$
Thermal	$\nabla \cdot \mathbf{q} = Q$	$\nabla \times \mathbf{M} = \mathbf{0}$	$\mathbf{M} = k \mathbf{q}$
Fluid	$\nabla \cdot \mathbf{N} = 0$	$\nabla \times \mathbf{v} = \mathbf{0}$	$\mathbf{N} = \rho \mathbf{v}$

Table 1.1: Boundary value problems in different engineering disciplines

of a curl equation, a divergence equation and a constitutive relation, that need to be solved subject to a set of boundary conditions. Although this thesis focuses on the solution of the magnetic and thermal equations, it is important to realize that the dual-energy method, the conclusions drawn and the methodology developed in the next Chapters can be applied to the solution of other engineering boundary value problems, such as those of Table 1.1.

Two points of view can be adopted in the solution of such problems. One embodies analytic methods such as conformal mapping and superposition [9], [10]. These offer the advantage of providing the exact answer to a problem, often in an attractively compact and general form. Such methods often rely on the geometrical symmetry of the structure, but may be inapplicable to problems with complicated geometries and large number of boundary conditions. With the advent of computers, numerical methods have become increasingly popular, offering accurate solutions to problems of arbitrary geometries. A large number of numerical methods is proposed and presented in the literature. The most widely applied method in the design and analysis of electric machines is the Finite Element Method (FEM) [11], [12]. FEM discretizes a problem into a large number of elements, and the field distribution is approximated

by polynomials inside each element. The approximate solution to the problem is then determined by extremizing an appropriate energy functional. The advantage of the FEM is that arbitrarily shaped problems consisting of a variety of materials can be analyzed. However, dense discretization is necessary for accurate geometry representation, and acceptable accuracy of the solution. The requirement for fine discretization has a direct impact on the computational speed and time. As a result, the finite element method becomes inappropriate for a design-optimization program where a large number of designs needs to be evaluated over a small time frame, unless very fast computer resources are available. This thesis proposes the use of the algebraic dual-energy method in the numerical solution of the VRM analysis problems.

The basic idea behind the dual-energy method involves the introduction of a convex and/or a concave energy functional. These functionals and their extrema provide upper and lower energy bounds to the true system energy, respectively. When averaged, the bounds may yield values very close to the system energy. The method originates from classical mechanics [13], [14], and has been successfully extended to electromagnetism [15], [16], [17], [18], [19], [20], [21], [22]. Penman and Fraser, and Hammond and Freeman applied the method in the 1980s to a number of simple electrostatic, magnetostatic and eddy current problems for which values of resistance, inductance and capacitance are hard to obtain analytically [23] - [36]. Their work underlines the fact that the dual-energy method approaches the problem at hand from the energy point of view and as a result, the system is treated as a whole. The goal is the energy and its derived parameters, while precise knowledge of the field distribution throughout the region of interest is not necessary; the calculated energy bounds may be far away from the actual system energy, but the averaging process of upper and lower bounds can result in significant error cancellation and yield an accurate result in very small computational times, thus avoiding computationally intensive field calculations.

The literature presents two different directions in applying the dual-energy method: the geometric approach and the algebraic approach. The geometric approach, most

widely known as the method of tubes and slices, subdivides the problem geometry into slices of equipotential surfaces and tubes of flux, resulting in lower and upper parameter bounds respectively. The effect of the tubes is the introduction of fictitious curl sources in the system, while the slices generate divergence sources. The distribution of these sources is controlled by requiring zero net fictitious sources at each individual slice or tube boundary, as well as in the system as a whole. Hammond and Qionghua [30] present some rules of thumb for subdividing the region but no formal guidelines have been formulated for a problem of arbitrary geometry. Sykulski in [37] presents a computer package (TAS) for calculating circuit parameters (R, L, C) using the method of tubes and slices. The advantages of this approach lie in the fact that the system is treated as a whole and only simple calculations are required, avoiding the time consuming matrix inversions of the FEM. However, the accuracy of the solution depends on the shape of the tubes and slices rather than on their number; the process of mesh refinement, commonly encountered in finite element analysis, is replaced here by a reshaping process. This suggests that one should examine more closely the effect of different distributions on bounds estimation, which is time consuming and problem (geometry) dependent. Special techniques are required to handle any nonlinearities present and/or different material interfaces. As a result, the application of TAS is restricted to that of a teaching aid. Miller in [8] has applied the geometric approach in VRM magnetic analysis and more specifically to the calculation of the minimum phase inductance. In his paper, the agreement between calculated and measured results is quite good; their ratio for a particular motor is 1.01. However, no results have been published on the accuracy of the method for a wide range of geometries, such as that obtained and analyzed during Monte Carlo design processes. In addition, no insight is given on the computational times and level of discretization required to achieve satisfactory accuracy levels.

The other direction that can be followed in applying the dual-energy method is the algebraic; the upper and lower bound functionals are explicitly calculated and extremized by assuming appropriate approximating polynomials for the potential and/or the field distributions throughout the problem geometry. This approach is

not as widely known or applied as the method of tubes and slices. Hammond has employed it in trivial examples with boundaries, boundary conditions and source distributions easily handled algebraically. However, the geometry of the VRM at the unaligned position, the dominating curvatures characterizing the electromagnetic field distribution, and the presence of a large number of boundary conditions arising at the steel boundaries, provides a challenging exercise in the application, behavior and effectiveness of the dual-energy method in a more realistic framework.

It is interesting to note the relation between the dual-energy method and the FEM. The finite element method on the one hand, employs only one energy functional, namely one that yields a lower energy bound. It requires fine discretization of the geometry at hand, if the system energy is to be calculated with accuracy. The dual energy-method on the other hand, extremizes two energy functionals. Its averaging process aims at canceling out the upper and lower bound deviations from the true system energy, E . As a result, a fine discretization is not necessary, as long as the two bounds are equidistant from E . The FEM is more suited for problems where the field distribution is required, whereas the dual-energy method is more appropriate for problems in which only lumped field-derived quantities, such as resistance, capacitance and inductance, are required. Cendes and Shenton in [38] couple the two methods in the solution of magnetic field problems. They employ complementary variational principles, in order to obtain error bounds and confidence limits for the finite element solution, forming criteria for interactive mesh refinement.

The algebraic dual-energy method (ADEM) is considered in more detail in this thesis. One may argue that the tubes and slices approach may look more appealing, since it requires sketching of both the flux and potential distributions, thus providing additional insight to the problem at hand. However, since the shape of both tubes and slices determines the accuracy, the method may prove hard to implement; it requires complicated computer algorithms, in order to efficiently handle arbitrary geometries and sketch flux and equipotential lines pertaining to physical intuition [1]. The algebraic dual-energy method on the other hand, may seem hard to implement since the integrals and bounds are calculated explicitly. With the continuous development

of symbolic manipulation software however, this approach may become increasingly popular. As illustrated in the next few chapters, such software can be employed in a one-time analytic calculation of the bounds of a particular geometry. Hence, expressions for the bounds can be obtained that are only a function of the problem dimensions and excitation. These can be subsequently translated into C code or any other programming language, and used repeatedly within a design-optimization program for varying geometries and excitation profiles, without a lot of computational cost.

1.5 Thesis Objectives

The objectives of this thesis and questions addressed are as follows.

- **Explore the algebraic dual-energy method.** The present literature on the algebraic dual-energy method involves simple examples with boundaries, boundary conditions and source distributions that are easily handled. However, the geometry of the variable reluctance motor at the unaligned position, the dominating curvatures characterizing its electromagnetic field distribution and the presence of a large number of boundary conditions arising at the steel boundaries, provide a challenging exercise on the feasibility of the method in a more realistic example.
- **Develop and apply an algorithm for the fast and accurate calculation of the VRM minimum phase inductance.** For a relatively small number of free coefficients, success of averaging the bounds is not guaranteed unless the equidistance of the bounds can be assured. A criterion must be developed to select the number of free coefficients required in the calculation of each bound so as to ensure equidistance from the exact solution.
- **Extend the dual-energy method application from electromagnetics to thermal analysis.** Based on the analogy that exists between the steady-state heat conduction equations and electrostatic equations, the idea of bounding the

magnetic energy of a system can be extended to the derivation and analytic calculation of upper and lower “thermal energy” bounds. This further introduces the idea of thermally analyzing and designing variable reluctance motors using the algebraic dual-energy method.

- **Find bounds to the hot spot of a VRM phase.** The last objective of this thesis is to extend the idea of bounding to the estimation of the hot spot, important in the design of VRMs. This problem addresses the issue of bounding the temperature at a point as opposed to bounding the energy of the whole system, and is analogous to finding the maximum magnetic or electric field within a geometry.

1.6 Thesis Organization

This thesis applies the algebraic dual-energy method to the efficient and accurate electromagnetic and thermal analysis of variable reluctance motors. The algebraic dual-energy method is applied to the calculation of the minimum phase inductance of VRMs, and to the estimation of their hot spot.

Chapter 2 provides the theory of the dual-energy method and the mechanics associated with its application to a series of electromagnetic problems with known, analytic solutions. Chapter 3 explores the application of the method in the calculation of the minimum phase inductance of the VRM. Error analysis for bounds control, ensuring equidistance, is provided for this problem. Chapter 4 further extends the method to thermal analysis and addresses the problem of bounding the temperature at a point in the geometry, as opposed to providing bounds for the energy of the whole system. Chapter 5 concludes the thesis with a summary of the most important results, and suggestions for further work.

Chapter 2

The Algebraic Dual-Energy Method

In this chapter the algebraic dual-energy method (ADEM) is presented in detail and illustrated by simple examples having analytic solutions. The examples may look trivial at first glance. However, the application of the ADEM to these examples provides insights into the method and illustrates its virtues and disadvantages.

2.1 Introduction

The dual-energy method yields upper and lower energy bounds to the energy of electromagnetic systems. Chapter 1 provides an introduction to the philosophy of the method, which has two formulations: geometric and algebraic. The geometric formulation involves the use of tubes and slices that define flux and potential barriers from which the energy bounds may be calculated. The algebraic formulation, which is the focus of this thesis, makes use of concave and/or convex functionals to approximate electromagnetic quantities from which the energy bounds may again be calculated.

More specifically, the algebraic dual-energy method employs two different functionals, Y and Z , that yield analytic upper and lower bounds to the true system energy, respectively. These bounds can be explicitly calculated by adopting approximations to the flux and potential distributions throughout the problem region. These

approximations are of the form

$$\alpha_0 + \sum_{i=1}^M \alpha_i N_i(x, y, z) \quad i = 1, 2, \dots, M. \quad (2.1)$$

The functions $N_i(x, y, z)$ form a set of basis functions which need not be complete. The free coefficients, α_i , are real constants which are calculated by extremizing the energy functionals Z and Y , resulting in a good “fit” for the assumed distributions. The extrema of Z and Y yield the lower and upper energy bounds E_{lower} and E_{upper} , respectively, as illustrated in the simple diagram of Figure 2-1. The average of these bounds, $E_{average}$, can provide a value close to the true system energy, E_{exact} . $E_{average}$ can be subsequently employed to develop lumped-parameter models of the system. It

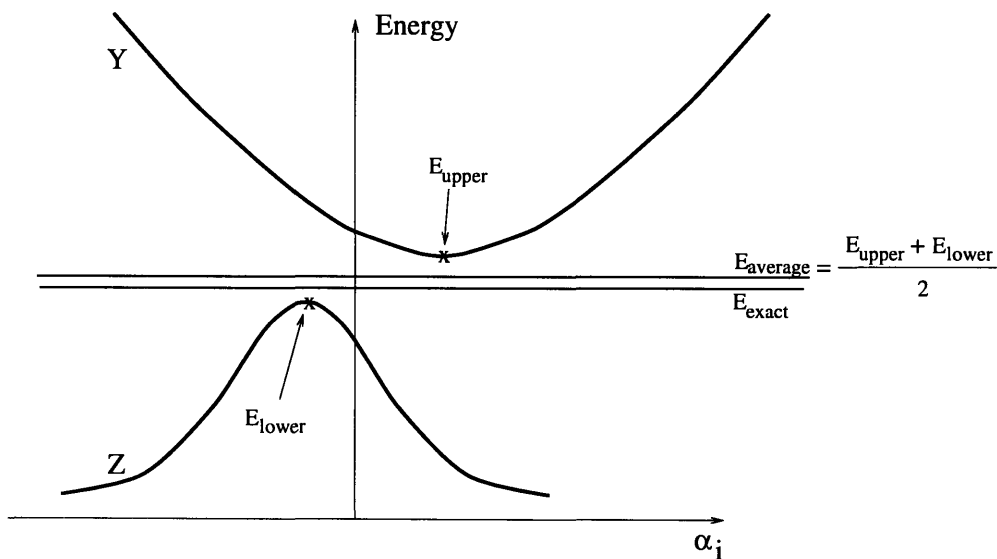


Figure 2-1: Graphical interpretation of the algebraic dual energy method

is this averaging process that permits even the crudest trial functions to yield results reasonably close to the correct answer.

2.2 Resistance Estimation Using the ADEM

In this section, the algebraic dual-energy method is employed in the calculation of static resistance as a means of illustrating the method. A proof of the existence of

upper and lower resistance bounds for arbitrarily-shaped three-dimensional linear resistors is given. An example with a known analytic solution is considered to illustrate the application of the method. The steps taken are described in detail and the issues involved in the application of the method are identified.

2.2.1 Existence of Upper and Lower Resistance Bounds

Consider the arbitrary resistor of Figure 2-2 which occupies the volume V . It is surrounded by the closed surface S , and is filled with the spatially-varying conductivity σ ; Outside S , the conductivity is zero. The surface S can be subdivided into three open surfaces S_+ , S_- and S_\perp , so that $S = S_+ \cup S_- \cup S_\perp$. The open surface S_+ defines the positive resistor terminal, a perfectly conducting surface over which the potential V_R is prescribed. Similarly, S_- defines the negative resistor terminal which is defined to be at zero potential. The remaining portion of S is S_\perp , over which the boundary condition $\mathbf{J} \cdot d\mathbf{S} = 0$ is prescribed. \mathbf{J} is the current density in the problem region. The static resistance R of the resistor is typically obtained by first solving

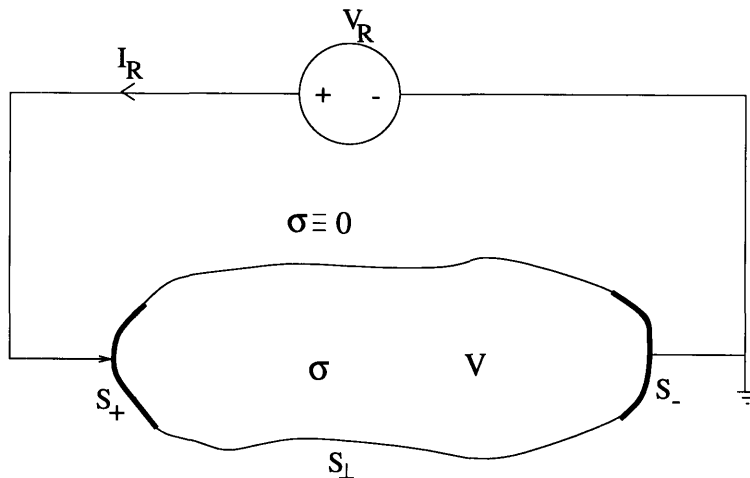


Figure 2-2: Arbitrary resistor definition

Maxwell's equations describing the system

$$\nabla \times \mathbf{E} = \mathbf{0} \Rightarrow \mathbf{E} = -\nabla\Phi \quad (2.2)$$

$$\nabla \cdot \mathbf{J} = 0 \quad (2.3)$$

$$\mathbf{J} = \sigma \mathbf{E} \quad (2.4)$$

subject to the imposed boundary conditions. Here, Φ is the electric potential and \mathbf{E} is the electric field intensity. Next, the current I_R flowing through the resistor is obtained from

$$I_R = \int_{S_+} \mathbf{J} \cdot d\mathbf{S} = - \int_{S_-} \mathbf{J} \cdot d\mathbf{S}. \quad (2.5)$$

Assuming V_R to be the known potential difference across the two resistor terminals, the resistance is given by

$$R = \frac{V_R}{I_R}. \quad (2.6)$$

Finally, the power dissipated in the resistor is given by

$$P = \int_V \mathbf{J} \cdot \mathbf{E} dV = \frac{V_R^2}{R} = R I_R^2. \quad (2.7)$$

Analytic bounds for the resistance can be found by calculating bounds to the dissipated power P . An upper bound to P , P_{lower} , that will yield a lower resistance bound, can be obtained by first choosing a function Φ_L to approximate the scalar potential, Φ , in V . Φ_L need only satisfy the Dirichlet boundary conditions on the resistor terminals, S_+ and S_- . These are $\Phi_L = V_R$ on S_+ and $\Phi_L = 0$ on S_- . The corresponding \mathbf{E}_L and \mathbf{J}_L are computed using

$$\mathbf{E}_L = -\nabla\Phi_L \quad (2.8)$$

$$\mathbf{J}_L = \sigma \mathbf{E}_L. \quad (2.9)$$

Note that \mathbf{J}_L need not satisfy its boundary condition on S_\perp , nor equation (2.3). Moreover, if substituted in (2.5), it will not yield the true resistor current, I_R . An upper bound for the dissipated power is computed using the functional

$$P_{lower} = \int_V \mathbf{E}_L \cdot \mathbf{J}_L dV. \quad (2.10)$$

Hence a lower bound for the resistance, R_{lower} , is obtained using

$$R_{lower} = \frac{V_R^2}{P_{lower}} \leq \frac{V_R^2}{P} = R. \quad (2.11)$$

$R_{lower} = R$ if and only if $\Phi_L = \Phi$. In order to prove that $P_{lower} \geq P$, define $\delta\Phi_L$ such that $\Phi_L = \Phi + \delta\Phi_L$. In a similar and consistent manner, define $\delta\mathbf{E}_L$ and $\delta\mathbf{J}_L$, such that $\mathbf{E}_L = \mathbf{E} + \delta\mathbf{E}_L$ and $\mathbf{J}_L = \mathbf{J} + \delta\mathbf{J}_L$. Then

$$\begin{aligned} P_{lower} &= \int_V \mathbf{E}_L \cdot \mathbf{J}_L \, dV \\ &= \int_V (\mathbf{E} + \delta\mathbf{E}_L) \cdot (\mathbf{J} + \delta\mathbf{J}_L) \, dV \\ &= P + 2 \int_V \mathbf{J} \cdot \delta\mathbf{E}_L \, dV + \int_V \sigma \delta\mathbf{E}_L \cdot \delta\mathbf{E}_L \, dV \\ &= P - 2 \int_V \mathbf{J} \cdot \nabla \delta\Phi_L \, dV + \int_V \sigma \delta\mathbf{E}_L \cdot \delta\mathbf{E}_L \, dV \\ &= P - 2 \int_V \nabla \cdot (\delta\Phi_L \mathbf{J}) \, dV + 2 \int_V \delta\Phi_L \nabla \cdot \mathbf{J} \, dV + \int_V \sigma \delta\mathbf{E}_L \cdot \delta\mathbf{E}_L \, dV \\ &= P - 2 \oint_S \delta\Phi_L \mathbf{J} \cdot d\mathbf{S} + 2 \int_V \delta\Phi_L \nabla \cdot \mathbf{J} \, dV + \int_V \sigma \delta\mathbf{E}_L \cdot \delta\mathbf{E}_L \, dV \\ &= P - 2 \int_{S_+} \delta\Phi_L \mathbf{J} \cdot d\mathbf{S} - 2 \int_{S_-} \delta\Phi_L \mathbf{J} \cdot d\mathbf{S} - 2 \int_{S_\perp} \delta\Phi_L \mathbf{J} \cdot d\mathbf{S} \\ &\quad + 2 \int_V \delta\Phi_L \nabla \cdot \mathbf{J} \, dV + \int_V \sigma \delta\mathbf{E}_L \cdot \delta\mathbf{E}_L \, dV \\ &= P + \int_V \sigma \delta\mathbf{E}_L \cdot \delta\mathbf{E}_L \, dV \\ &\geq P. \end{aligned} \quad (2.12)$$

The third equality holds because, by definition, $\delta\mathbf{J}_L = \sigma \delta\mathbf{E}_L$ and $\mathbf{J} = \sigma \mathbf{E}$. To obtain the fourth equality, the definition $\delta\mathbf{E}_L = -\nabla\delta\Phi_L$ is used. The fifth equality makes use of the vector identity $\nabla \cdot (\delta\Phi_L \mathbf{J}) = \delta\Phi_L \nabla \cdot \mathbf{J} + (\mathbf{J} \cdot \nabla) \delta\Phi_L$. The sixth step employs the divergence theorem. The last equality holds because $\mathbf{J} \cdot d\mathbf{S} = 0$ on S_\perp and $\delta\Phi_L = 0$ on S_+ and S_- ; also $\nabla \cdot \mathbf{J} = 0$ in the resistor volume.

An upper bound for the resistance may be obtained by choosing a function \mathbf{J}_U to approximate the current density \mathbf{J} in V . \mathbf{J}_U satisfies (2.3), as well as its boundary

condition on S_\perp . It also defines a current I_R through (2.5), such that

$$I_R = \int_{S_+} \mathbf{J}_U \cdot d\mathbf{S}. \quad (2.13)$$

The corresponding electric field is obtained from

$$\mathbf{E}_U = \frac{1}{\sigma} \mathbf{J}_U \quad (2.14)$$

and is not necessarily curl free. As a result, in the calculation of an upper bound, the Dirichlet boundary conditions are not necessarily satisfied. An upper bound for the power dissipated in the system can then be obtained using the functional

$$P_{upper} = \int_V \mathbf{J}_U \cdot \mathbf{E}_U dV. \quad (2.15)$$

Hence an upper bound for the resistance, R_{upper} , is obtained using

$$R_{upper} = \frac{P_{upper}}{I_R^2} \geq \frac{P}{I_R^2} = R. \quad (2.16)$$

Note that $R_{upper} = R$ if and only if $\mathbf{J}_U = \mathbf{J}$.

In order to prove that $P_{upper} \geq P$, define $\delta\mathbf{J}_U$ such that $\mathbf{J}_U = \mathbf{J} + \delta\mathbf{J}_U$. In a similar and consistent manner, define $\delta\mathbf{E}_U$ such that $\mathbf{E}_U = \mathbf{E} + \delta\mathbf{E}_U$. Then,

$$\begin{aligned} P_{upper} &= \int_V \mathbf{J}_U \cdot \mathbf{E}_U dV \\ &= \int_V (\mathbf{J} + \delta\mathbf{J}_U) \cdot (\mathbf{E} + \delta\mathbf{E}_U) dV \\ &= P + 2 \int_V \mathbf{E} \cdot \delta\mathbf{J}_U dV + \int_V \sigma \delta\mathbf{E}_U \cdot \delta\mathbf{E}_U dV \\ &= P - 2 \int_V (\nabla\Phi) \cdot \delta\mathbf{J}_U dV + \int_V \sigma \delta\mathbf{E}_U \cdot \delta\mathbf{E}_U dV \\ &= P - 2 \int_V \nabla \cdot (\Phi \delta\mathbf{J}_U) dV + 2 \int_V \Phi \nabla \cdot \delta\mathbf{J}_U dV + \int_V \sigma \delta\mathbf{E}_U \cdot \delta\mathbf{E}_U dV \\ &= P - 2 \oint_S \Phi \delta\mathbf{J}_U \cdot d\mathbf{S} + 2 \int_V \Phi \nabla \cdot \delta\mathbf{J}_U dV + \int_V \sigma \delta\mathbf{E}_U \cdot \delta\mathbf{E}_U dV \\ &= P - 2 \int_{S_+} \Phi \delta\mathbf{J}_U \cdot d\mathbf{S} - 2 \int_{S_-} \Phi \delta\mathbf{J}_U \cdot d\mathbf{S} - 2 \int_{S_\perp} \Phi \delta\mathbf{J}_U \cdot d\mathbf{S} \\ &\quad + 2 \int_V \Phi \nabla \cdot \delta\mathbf{J}_U dV + \int_V \sigma \delta\mathbf{E}_U \cdot \delta\mathbf{E}_U dV \end{aligned}$$

$$\begin{aligned}
&= P + \int_V \sigma \delta \mathbf{E}_U \cdot \delta \mathbf{E}_U dV \\
&\geq P.
\end{aligned} \tag{2.17}$$

The third equality holds because, by definition, $\delta \mathbf{J}_U = \sigma \delta \mathbf{E}_U$ and $\mathbf{J} = \sigma \mathbf{E}$. The fourth equality uses $\mathbf{E} = -\nabla \Phi$. The fifth equality makes use of the vector identity $\nabla \cdot (\Phi \delta \mathbf{J}_U) = \Phi \nabla \cdot \delta \mathbf{J}_U + (\delta \mathbf{J}_U \cdot \nabla) \Phi$. The sixth step employs the divergence theorem. The last equality is valid because, by construction, $\delta \mathbf{J}_U \cdot d\mathbf{S} = 0$ on S_\perp and $\nabla \cdot \delta \mathbf{J}_U = 0$ in V . Last but not least, the surface integral of $\delta \mathbf{J}_U$ vanishes over S_+ and S_- .

It is interesting to note that since \mathbf{J}_U is chosen to satisfy the zero divergence condition

$$\nabla \cdot \mathbf{J}_U = 0 \Rightarrow \mathbf{J}_U = \nabla \times \mathbf{T}_U \tag{2.18}$$

the upper bound derivation could start by adopting an electric vector potential, \mathbf{T}_U , such that $\mathbf{T}_U = \mathbf{T} + \delta \mathbf{T}_U$. Such an approach is helpful in two-dimensional resistor problems with current excitations transverse to the plane of the problem; \mathbf{T}_U will then have a single spatial component, thus simplifying the analysis.

2.2.2 Example: Right-Angled Conductor

Following the theoretical analysis of the previous section, the ADEM is applied here to a resistor problem with a known analytic solution. To obtain an upper resistance bound, the following steps are taken:

- Guess a current density distribution, \mathbf{J}_U , which satisfies the boundary condition for \mathbf{J} on S_\perp , namely

$$\mathbf{J}_U \cdot d\mathbf{S} = 0 \tag{2.19}$$

as well as the relation

$$\nabla \cdot \mathbf{J}_U = 0 \tag{2.20}$$

in the resistor volume. Each component of \mathbf{J}_U can be an approximation of the form

$$J_{U_{x,y,z}} = \sum_{i=0}^{i=K} \alpha_{i_{x,y,z}} N_{i_{x,y,z}}(x, y, z) \quad (2.21)$$

where K is the number of free coefficients, $\alpha_{i_{x,y,z}}$ are the free coefficients to be calculated, and $N_{i_{x,y,z}}$ are the trial functions in x , y and z . Imposing (2.19) and (2.20) will constrain some (or all) of the free coefficients $\alpha_{i_{x,y,z}}$.

- Set

$$I_R = \int_{S_+} \mathbf{J}_U \cdot d\mathbf{S} \quad (2.22)$$

where I_R is the total current through the resistor terminals.

- Obtain the corresponding electric field distribution, \mathbf{E}_U , from

$$\mathbf{E}_U = \frac{1}{\sigma} \mathbf{J}_U. \quad (2.23)$$

- Calculate the power dissipated in the resistor, P_{upper} , from

$$P_{upper} = \int_V \mathbf{J}_U \cdot \mathbf{E}_U dV. \quad (2.24)$$

- Calculate any remaining free coefficients, $\alpha_{i_{x,y,z}}$, by extremizing P_{upper} by solving the algebraic set of equations

$$\frac{\partial P_{upper}}{\partial \alpha_{i_{x,y,z}}} = 0. \quad (2.25)$$

- Obtain an upper bound for the resistance from

$$R_{upper} = \frac{P_{upper}}{I_R^2}. \quad (2.26)$$

Similarly, the steps taken to obtain a lower resistance bound are as follows.

- Guess a potential distribution, Φ_L , satisfying the boundary conditions for Φ on S_+ and S_- . Φ_L can be an approximation of the form

$$\Phi_L = \sum_{i=0}^{i=K} \beta_{i_{x,y,z}} N_{i_{x,y,z}}(x, y, z) \quad (2.27)$$

where K is the number of free coefficients, $\beta_{i_{x,y,z}}$ are the free coefficients to be calculated, and $N_{i_{x,y,z}}$ are trial functions in x , y and z . Imposing the boundary conditions for Φ_L will constrain some (or all) of the free coefficients $\beta_{i_{x,y,z}}$.

- Obtain the corresponding electric field distribution, \mathbf{E}_L , from

$$\mathbf{E}_L = -\nabla\Phi_L. \quad (2.28)$$

- Calculate the power dissipated in the resistor, P_{lower} , from

$$P_{lower} = \int_V \sigma \mathbf{E}_L \cdot \mathbf{E}_L dV. \quad (2.29)$$

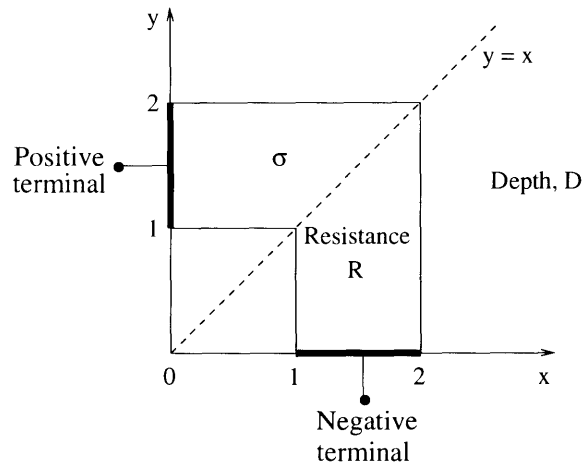
- Calculate any remaining free coefficients, $\beta_{i_{x,y,z}}$, by extremizing P_{lower} by solving the algebraic set of equations

$$\frac{\partial P_{lower}}{\partial \beta_{i_{x,y,z}}} = 0. \quad (2.30)$$

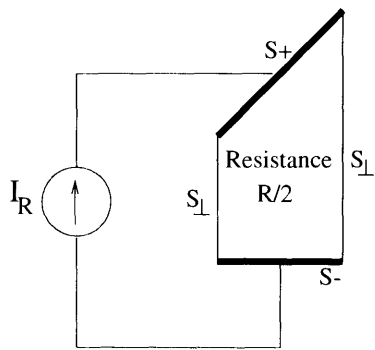
- Obtain the lower bound for the resistance from

$$R_{lower} = \frac{V_R^2}{P_{lower}}. \quad (2.31)$$

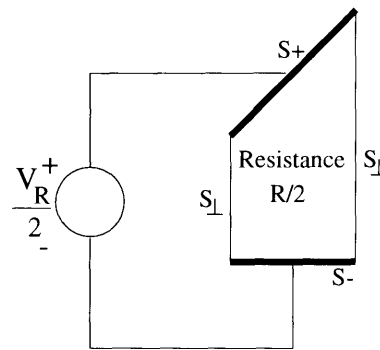
This algorithm is now illustrated by considering the right-angled conductor of Figure 2-3(a). It is assumed to have depth D into the paper and a uniform conductivity σ throughout its volume. The end electrodes are perfectly conducting and the potential difference between the two terminals is V_R , and the total current through the terminals is I_R . The uniformity of the cross-section in the z -direction simplifies



(a)



(b)



(c)

Figure 2-3: Right-angled resistor problem

the resistance calculation to that of a two-dimensional problem. Furthermore, the symmetry that exists about the $x = y$ line permits analysis of half of the problem geometry, as shown in Figures 2-3(b) and 2-3(c). The task of determining an exact value for the resistance R is hindered by the polygonal shape of the structure. However, the method of conformal mapping [9], [10] can be employed to obtain an analytic solution. Using the Schwarz-Christoffel transformation, R is found to be [39]

$$R = \frac{2.558523142}{\sigma D} \quad (\Omega) \quad (2.32)$$

The algebraic dual-energy method is applied below to obtain analytic upper and lower resistance bounds.

Resistance Upper Bound: R_{upper}

As shown in Figure 2-3(b), the bounding surface of the resistor is broken up into three open surfaces, S_+ , S_- , S_\perp , the positive and negative terminals and the remaining bounding surface, respectively. Next, \mathbf{J}_U is chosen within the resistor subject to (2.19) and (2.20). Condition (2.20) can be enforced by setting

$$\mathbf{J}_U = \nabla \times \mathbf{T}_U. \quad (2.33)$$

For the two-dimensional problem at hand, \mathbf{T}_U has only one component in the z -direction, namely T_U . Considering only half of the problem due to symmetry, T_U should satisfy the following boundary conditions on S_\perp :

- $\frac{\partial T_U}{\partial y} = 0$ at $x = 1$
- $\frac{\partial T_U}{\partial y} = 0$ at $x = 2$

so that (2.19) is satisfied. A second order polynomial in x and y is employed for T_U such that

$$T_U = a_1 + a_2x + a_3y + a_4xy + a_5x^2 + a_6y^2. \quad (2.34)$$

The first boundary condition on T_U requires that $a_6 = 0$, and $a_3 = -a_4$. The second boundary condition imposes $a_4 = 0$, and hence $a_3 = 0$. Then,

$$T_U = a_1 + a_2 x + a_5 x^2. \quad (2.35)$$

The corresponding current density is then

$$\mathbf{J}_U = \frac{\partial T_U}{\partial y} \hat{\mathbf{x}} - \frac{\partial T_U}{\partial x} \hat{\mathbf{y}} = (-a_2 - 2a_5 x) \hat{\mathbf{y}}. \quad (2.36)$$

Setting

$$I_R = - \int_{S_-} \mathbf{J}_U \cdot d\mathbf{S} = -D \int_1^2 (a_2 + 2 a_5 x) dx \quad (2.37)$$

gives an extra constraint on the coefficients, namely

$$a_2 = -\left(\frac{I_R}{D} + 3 a_5\right). \quad (2.38)$$

Substituting (2.38) into (2.36), the electric field distribution is obtained as

$$\mathbf{E}_U = \frac{1}{\sigma} \mathbf{J}_U = \frac{1}{\sigma} \left[\frac{I_R}{D} + a_5(3 - 2x)\right] \hat{\mathbf{y}}. \quad (2.39)$$

Next, the power dissipated in the whole resistor volume, P_{upper} , is given by

$$\begin{aligned} P_{upper} &= 2 \int_{V/2} \mathbf{J}_U \cdot \mathbf{E}_U dV \\ &= 2 D \frac{1}{\sigma} \int_{S/2} \left[\frac{I_R}{D} + a_5(3 - 2x)\right] \hat{\mathbf{y}} \cdot \left[\frac{I_R}{D} + a_5(3 - 2x)\right] \hat{\mathbf{y}} dy dx \\ &= 2 D \frac{1}{\sigma} \int_{x=1}^2 \int_{y=0}^x \left[\frac{I_R}{D} + a_5(3 - 2x)\right]^2 dy dx \\ &= 2 \frac{1}{\sigma} D \left(\frac{a_5^2}{2} - \frac{a_5 I_R}{3 D} + \frac{3 I_R^2}{2 D^2}\right) \end{aligned} \quad (2.40)$$

and a_5 is determined by extremizing P_{upper} according to

$$\frac{\partial P_{upper}}{\partial a_5} = 0 \Rightarrow a_5 = \frac{I_R}{3 D}. \quad (2.41)$$

Substituting back into (2.40), yields

$$P_{upper} = \frac{26}{9} \frac{1}{\sigma} \frac{I_R^2}{D}. \quad (2.42)$$

The upper resistance bound is given by

$$R_{upper} = \frac{P_{upper}}{I_R^2} = \frac{26}{9 \sigma D} = \frac{2.888888889}{\sigma D} \quad (\Omega) \quad (2.43)$$

which is within 13% of the exact answer. Maple V [40], a symbolic manipulation software package, can be used to generate the above equations. A script file that performs the above operations and yield an upper resistance bound is included in Appendix A at the end of this chapter. Unity D and σ are assumed for simplicity.

The same process can be repeated to generate better upper bounds by increasing the order of the polynomial approximation for T_U . Table 2.1 summarizes the upper resistance bounds obtained using different orders of approximation for the guessed T_U . For example, the first order polynomial approximation for T_U is given by

$$T_U = a_1 + a_2x + a_3y \quad (2.44)$$

and results in $R_{upper} = 3.0 \quad (\Omega)$. The third order polynomial approximation is

$$T_U = a_1 + a_2x + a_3y + a_4xy + a_5x^2 + a_6y^2 + a_7x^2y + a_8xy^2 + a_9x^3 + a_{10}y^3 \quad (2.45)$$

and yields $R_{upper} = 2.7179204 \quad (\Omega)$. Notice that a zeroth-order approximation in x and y is constant, and so does not provide enough free coefficients to satisfy the boundary conditions for T_U .

Resistance Lower Bound: R_{lower}

To obtain a lower bound for the resistance of the geometry of Figure 2-3, half of the resistor problem is considered again as shown in Figure 2-3(c). A potential distribution

$R_{exact} = 2.5585231 \text{ } (\Omega)$				
Order of approximation	Lower bound (Ω)	Upper bound (Ω)	$R_{average}$ (Ω)	Difference $ R_{average} - R_{exact} $
0	-	-	-	-
1	2.1640426	3.0	2.5820213	0.0234981
2	2.4266065	2.8888889	2.6577477	0.0992246
3	2.4506032	2.7179204	2.5842618	0.0257387

Table 2.1: Resistance bounds for the right-angled conductor problem

is adopted according to

$$\Phi_L = \frac{V_s y}{2 x} \quad (2.46)$$

for example, which satisfies the boundary conditions for Φ , namely $\Phi_L = 0$ at $y = 0$, and $\Phi_L = \frac{V_s}{2}$ at $y = x$. The corresponding electric field distribution is

$$\mathbf{E}_L = -\nabla\Phi_L = \frac{V_s}{2} \left[\frac{y}{x^2} \hat{\mathbf{x}} - \frac{1}{x} \hat{\mathbf{y}} \right]. \quad (2.47)$$

Finally, the power dissipated in the resistor volume is

$$\begin{aligned} P_{lower} &= \int_V \sigma \mathbf{E}_L \cdot \mathbf{E}_L dV \\ &= 2 \sigma D \int_{S/2} \frac{V_s^2}{4 x^4} (y^2 + x^2) dx dy \\ &= 2 \sigma D \int_{x=1}^2 \int_{y=0}^x \frac{V_s^2}{4 x^4} (y^2 + x^2) dy dx \\ &= \frac{2 \sigma D V_s^2 \ln(2)}{3}. \end{aligned} \quad (2.48)$$

Hence,

$$R_{lower} = \frac{V_s^2}{P_{lower}} = \frac{2.1640426}{\sigma D} \Omega \quad (2.49)$$

which is approximately 15.5% below the exact solution. Maple V can be used again to generate the above equations. A script file that performs the above operations and yields the lower resistance bound of (2.49) is included in Appendix A at the end of the chapter. Again unity σ and D are assumed for simplicity.

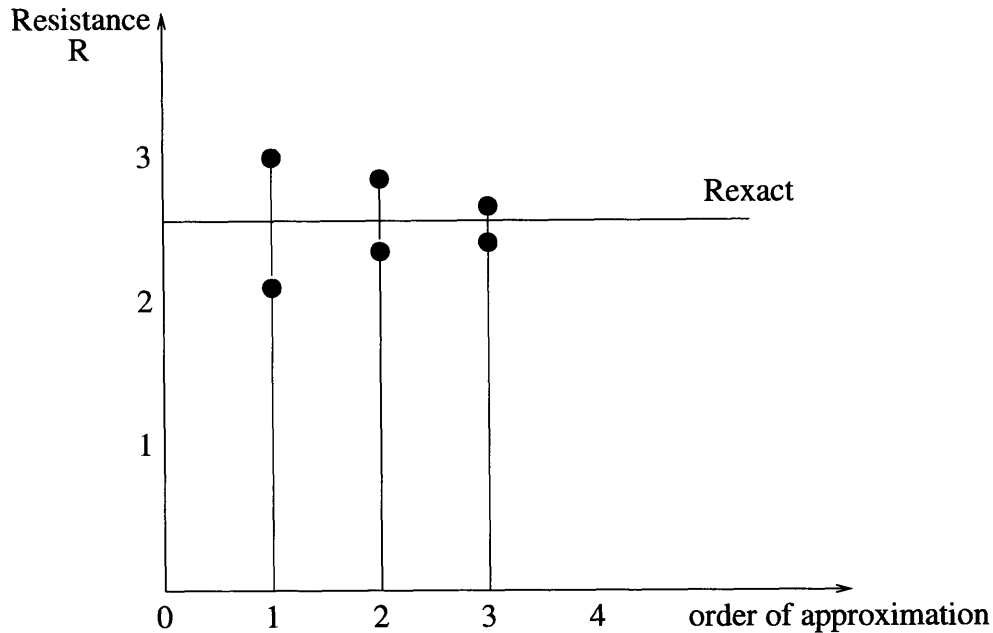


Figure 2-4: Resistance bounds vs. order of approximation

Increasing the order of approximation for Φ_L , results in improved lower resistance bounds. Table 2.1 summarizes the results obtained using different orders of approximation for the guessed Φ_L . The same table also includes the corresponding averages of the lower and upper bounds, which are within 10% of the exact value of $R = 2.558523142 \ \Omega$.

Observations on the Resistor Problem

Figure 2-4 displays the calculated bounds against the order of approximation for the resistor problem. As the order of approximation increases, the individual resistance bounds move closer to the exact value but their average does not necessarily improve. This suggests that, for an increase in the order of approximation and number of free coefficients, averaging of the bounds does not guarantee a better result. It is hence immediately clear that equidistance of bounds is a critical and important factor in guaranteeing success of the method; the order of field approximation is not as critical in averaging unless very high orders are considered.

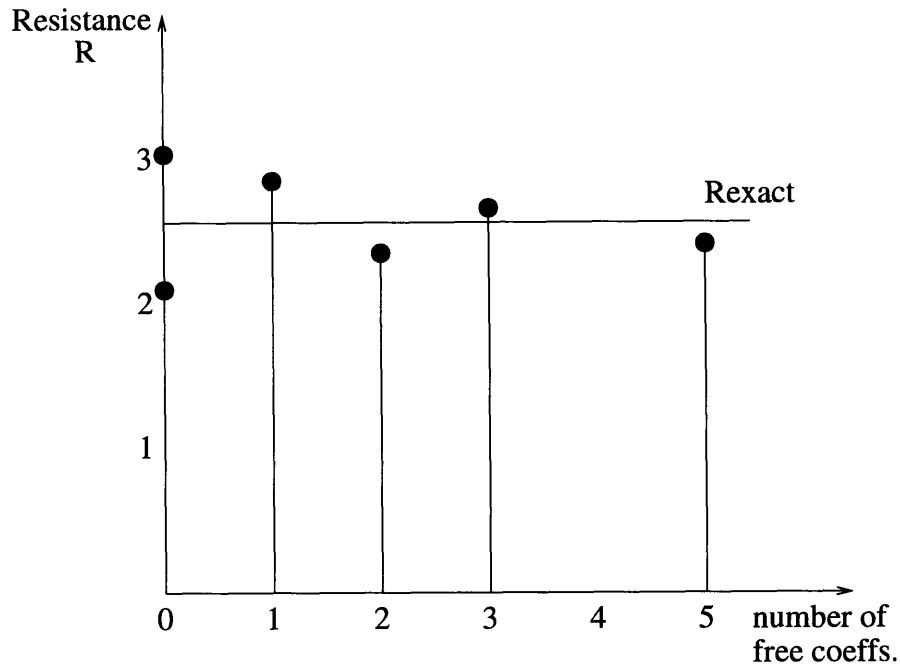


Figure 2-5: Resistance bounds vs. number of free coefficients

Another interesting point lies in the calculation of the lower bound. The approximation used for the scalar potential

$$\Phi_L = \frac{V_s y}{2x} \quad (2.50)$$

is not a polynomial in both x and y . Due to the resistor shape, the boundary conditions for Φ would be impossible to match simultaneously, unless the $\frac{1}{x}$ dependence is employed; this guess is not a polynomial guess for Φ_L . The application of (2.50) has two implications: on the one hand, care should be taken with divisions; if a point with abscissa $x = 0$ exists in the problem domain, division by x is an invalid operation. Moreover, the original notion of an “order of approximation” is less clear; this is due to the presence of negative powers of x in (2.50) that is essential in matching the boundary conditions. It is therefore more meaningful to plot the calculated bounds versus the number of free coefficients, as shown in Figure 2-5.

From the above discussion, several rules of thumb for implementing the ADEM can be deduced.

- The type of approximation employed for the guessed field distributions is critical. It must have an x - y dependence and/or enough free coefficients, to allow all pertinent boundary conditions and Maxwell's equations to be met. It must also be easy to integrate, requiring minimal numerical computation.
- The calculation of the upper bounds may require different approximating functions than the calculation of the lower bounds. This is strongly dependent on the problem geometry and boundary conditions.

2.3 Capacitance Estimation Using the Algebraic Dual-Energy Method

In this section, the calculation of static capacitance using the algebraic dual-energy method is presented. A proof on the existence of upper and lower capacitance bounds is given. Since the static capacitance problem is similar to that of the static resistance problem, an example is provided in Appendix B at the end of the chapter.

2.3.1 Existence of Upper and Lower Capacitance Bounds

The proof in this section closely follows that presented above for resistance bounds. Consider the arbitrary capacitor of Figure 2-6. S_+ and S_- are the positive and negative capacitor terminals respectively, with prescribed potential values. The body of the capacitor is the infinite volume V of spatially-varying permittivity, ϵ , bounded by the closed surface S_\perp at infinity. The electric potential Φ is assumed constant at V_C on S_+ , and $\Phi = 0$ on S_- . Moreover, \mathbf{E} and \mathbf{D} , the electric field intensity and the displacement flux density respectively, vanish on S_\perp .

The static capacitance C of the capacitor is obtained by first solving Maxwell's

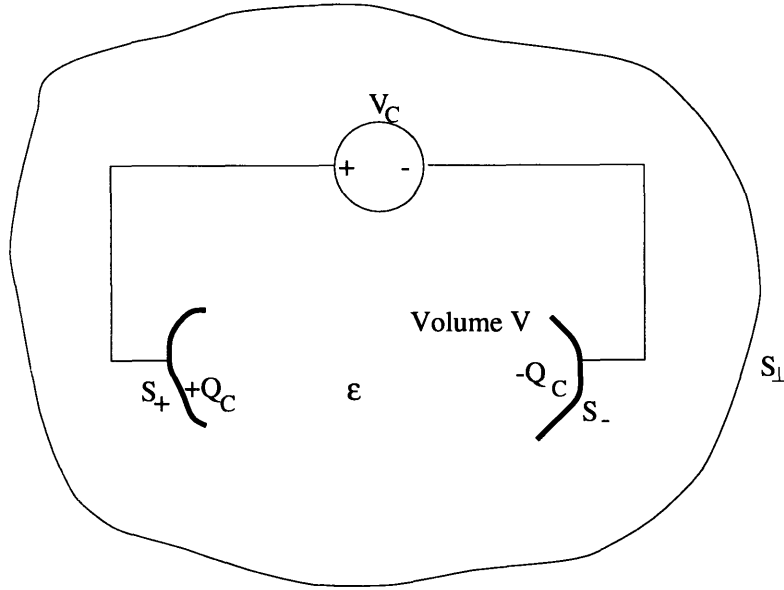


Figure 2-6: Arbitrary capacitor definition

equations describing the system

$$\nabla \times \mathbf{E} = \mathbf{0} \Rightarrow \mathbf{E} = -\nabla\Phi \quad (2.51)$$

$$\nabla \cdot \mathbf{D} = 0 \quad (2.52)$$

$$\mathbf{D} = \epsilon \mathbf{E} \quad (2.53)$$

subject to the imposed boundary conditions. The total charge on the positive terminal is next obtained from

$$Q_C = \oint_{S_+} \mathbf{D} \cdot d\mathbf{S} = -\oint_{S_-} \mathbf{D} \cdot d\mathbf{S}. \quad (2.54)$$

The capacitance is then given by

$$C = \frac{Q_C}{V_C} \quad (2.55)$$

where V_C is the potential difference between the two capacitor terminals. The electric energy stored in the capacitor is

$$W_e = \frac{1}{2} \int_V \mathbf{D} \cdot \mathbf{E} \, dV = \frac{C V_C^2}{2} = \frac{Q_C^2}{2C}. \quad (2.56)$$

Analytic bounds for the capacitance can be obtained by calculating bounds for the stored energy. An upper energy bound, W_{lower} , that will yield a lower capacitance bound, can be calculated by first choosing a function \mathbf{D}_L to approximate \mathbf{D} in V . \mathbf{D}_L need only satisfy the boundary condition on S_\perp , as well as the zero divergence condition, $\nabla \cdot \mathbf{D}_L = 0$. The corresponding \mathbf{E}_L is computed from

$$\mathbf{E}_L = \frac{1}{\epsilon} \mathbf{D}_L. \quad (2.57)$$

Note that \mathbf{E}_L need not be curl free and its line integral need not satisfy the boundary conditions for Φ on S_+ and S_- . The charge on the positive terminal, Q_C , can be obtained from

$$Q_C = \oint_{S_+} \mathbf{D}_L \cdot d\mathbf{S}. \quad (2.58)$$

An upper bound for the stored energy is computed using the functional

$$W_{lower} = \frac{1}{2} \int_V \mathbf{E}_L \cdot \mathbf{D}_L dV. \quad (2.59)$$

and hence, a lower bound for the capacitance, C_{lower} , can be calculated from

$$C_{lower} = \frac{Q_C^2}{2 W_{lower}} \leq \frac{Q_C^2}{W_e} = C. \quad (2.60)$$

Note that $C_{lower} = C$ if and only if $\mathbf{D}_L = \mathbf{D}$.

In order to prove that $W_{lower} \geq W_e$, define $\delta\mathbf{D}_L$ such that $\mathbf{D}_L = \mathbf{D} + \delta\mathbf{D}_L$. In a similar and consistent manner, define $\delta\mathbf{E}_L$ such that $\mathbf{E}_L = \mathbf{E} + \delta\mathbf{E}_L$. Then

$$\begin{aligned} W_{lower} &= \frac{1}{2} \int_V \mathbf{E}_L \cdot \mathbf{D}_L dV \\ &= \frac{1}{2} \int_V (\mathbf{E} + \delta\mathbf{E}_L) \cdot (\mathbf{D} + \delta\mathbf{D}_L) dV \\ &= W_e + \int_V \mathbf{E} \cdot \delta\mathbf{D}_L dV + \frac{1}{2} \int_V \epsilon \delta\mathbf{E}_L \cdot \delta\mathbf{E}_L dV \\ &= W_e - \int_V \nabla\Phi \cdot \delta\mathbf{D}_L dV + \frac{1}{2} \int_V \epsilon \delta\mathbf{E}_L \cdot \delta\mathbf{E}_L dV \\ &= W_e - \int_V \nabla \cdot (\Phi \delta\mathbf{D}_L) dV + \int_V \Phi \nabla \cdot \delta\mathbf{D}_L dV + \frac{1}{2} \int_V \epsilon \delta\mathbf{E}_L \cdot \delta\mathbf{E}_L dV \end{aligned}$$

$$\begin{aligned}
&= W_e - \oint_S \Phi \delta \mathbf{D}_L \cdot d\mathbf{S} + \int_V \Phi \nabla \cdot \delta \mathbf{D}_L dV + \frac{1}{2} \int_V \epsilon \delta \mathbf{E}_L \cdot \delta \mathbf{E}_L dV \\
&= W_e - \int_{S_+} \Phi \delta \mathbf{D}_L \cdot d\mathbf{S} - \int_{S_-} \Phi \delta \mathbf{D}_L \cdot d\mathbf{S} - \int_{S_\perp} \Phi \delta \mathbf{D}_L \cdot d\mathbf{S} \\
&\quad + \int_V \Phi \nabla \cdot \delta \mathbf{D}_L dV + \frac{1}{2} \int_V \epsilon \delta \mathbf{E}_L \cdot \delta \mathbf{E}_L dV \\
&= W_e + \frac{1}{2} \int_V \epsilon \delta \mathbf{E}_L \cdot \delta \mathbf{E}_L dV \\
&\geq W_e
\end{aligned} \tag{2.61}$$

The third equality holds because, by definition, $\delta \mathbf{D}_L = \epsilon \delta \mathbf{E}_L$ and $\mathbf{D} = \epsilon \mathbf{E}$. To obtain the fourth equality, the definition $\mathbf{E} = -\nabla \Phi$ is used. The fifth equality makes use of the vector identity $\nabla \cdot (\Phi \delta \mathbf{D}_L) = \Phi \nabla \cdot \delta \mathbf{D}_L + (\delta \mathbf{D}_L \cdot \nabla) \Phi$. The sixth equality employs the divergence theorem. The last equality holds because, by construction, $\delta \mathbf{D}_L = 0$ on S_\perp and the surface integral of $\delta \mathbf{D}_L$ vanishes over the terminals S_+ and S_- ; moreover, by construction, $\nabla \cdot \delta \mathbf{D}_L = 0$ in the capacitor volume.

Similarly, an upper bound for the capacitance may be calculated by choosing a vector \mathbf{E}_U to approximate \mathbf{E} in V . \mathbf{E}_U should satisfy the zero-curl condition

$$\nabla \times \mathbf{E}_U = \mathbf{0}. \tag{2.62}$$

This can be automatically satisfied by adopting a function Φ_U to approximate Φ in V . Φ_U satisfies the Dirichlet boundary conditions on S_+ and S_- . Then,

$$\mathbf{E}_U = -\nabla \Phi_U \tag{2.63}$$

$$\mathbf{D}_U = \epsilon \mathbf{E}_U. \tag{2.64}$$

Note that \mathbf{D}_U will not necessarily be solenoidal, nor satisfy the boundary conditions on S_\perp . An upper bound for the stored system energy is obtained using the functional

$$W_{upper} = \frac{1}{2} \int_V \mathbf{D}_U \cdot \mathbf{E}_U dV \tag{2.65}$$

and an upper bound for the capacitance, C_{upper} , can be calculated from

$$C_{upper} = \frac{2 W_{upper}}{V_C^2} \geq \frac{2 W_e}{V_C^2} = C. \quad (2.66)$$

Note that $C_{upper} = C$ if and only if $\Phi_U = \Phi$.

In order to prove that $W_{upper} \geq W_e$, define $\delta\Phi_U$ such that $\Phi_U = \Phi + \delta\Phi_U$. In a similar and consistent manner, define $\delta\mathbf{E}_U$ and $\delta\mathbf{D}_U$ such that $\mathbf{E}_U = \mathbf{E} + \delta\mathbf{E}_U$ and $\mathbf{D}_U = \mathbf{D} + \delta\mathbf{D}_U$. Then,

$$\begin{aligned} W_{upper} &= \frac{1}{2} \int_V \mathbf{D}_U \cdot \mathbf{E}_U \, dV \\ &= \frac{1}{2} \int_V (\mathbf{D} + \delta\mathbf{D}_U) \cdot (\mathbf{E} + \delta\mathbf{E}_U) \, dV \\ &= W_e + \int_V \mathbf{D} \cdot \delta\mathbf{E}_U \, dV + \frac{1}{2} \int_V \epsilon \delta\mathbf{E}_U \cdot \delta\mathbf{E}_U \, dV \\ &= W_e - \int_V \mathbf{D} \cdot \nabla \delta\Phi_U \, dV + \frac{1}{2} \int_V \epsilon \delta\mathbf{E}_U \cdot \delta\mathbf{E}_U \, dV \\ &= W_e - \int_V \nabla \cdot (\delta\Phi_U \mathbf{D}) \, dV + \int_V \delta\Phi_U \nabla \cdot \mathbf{D} \, dV + \frac{1}{2} \int_V \epsilon \delta\mathbf{E}_U \cdot \delta\mathbf{E}_U \, dV \\ &= W_e - \oint_S \delta\Phi_U \mathbf{D} \cdot d\mathbf{S} + \int_V \delta\Phi_U \nabla \cdot \mathbf{D} \, dV + \frac{1}{2} \int_V \epsilon \delta\mathbf{E}_U \cdot \delta\mathbf{E}_U \, dV \\ &= W_e - \int_{S_+} \delta\Phi_U \mathbf{D} \cdot d\mathbf{S} - \int_{S_-} \delta\Phi_U \mathbf{D} \cdot d\mathbf{S} - \int_{S_\perp} \delta\Phi_U \mathbf{D} \cdot d\mathbf{S} \\ &\quad + \int_V \delta\Phi_U \nabla \cdot \mathbf{D} \, dV + \frac{1}{2} \int_V \epsilon \delta\mathbf{E}_U \cdot \delta\mathbf{E}_U \, dV \\ &= W_e + \frac{1}{2} \int_V \epsilon \delta\mathbf{E}_U \cdot \delta\mathbf{E}_U \, dV \\ &\geq W_e. \end{aligned} \quad (2.67)$$

The third equality holds because, by definition, $\delta\mathbf{D}_U = \epsilon \delta\mathbf{E}_U$ and $\mathbf{D} = \epsilon \mathbf{E}$. The fourth equality uses $\delta\mathbf{E}_U = -\nabla\delta\Phi_U$. The fifth equality makes use of the vector identity $\nabla \cdot (\delta\Phi_U \mathbf{D}) = \delta\Phi_U \nabla \cdot \mathbf{D} + (\mathbf{D} \cdot \nabla) \delta\Phi_U$. The sixth equality employs the divergence theorem. The last equality is valid because, by definition, $\mathbf{D} = \mathbf{0}$ on S_\perp and $\nabla \cdot \mathbf{D} = 0$ in V ; moreover $\delta\Phi_U = 0$ on S_+ and S_- .

An example on the application of the ADEM to a closed capacitor problem is given in Appendix B of this chapter. That problem forms a subset of the more general open capacitor problem analyzed here.

2.4 Inductance Estimation Using the Algebraic Dual-Energy Method

Dual-Energy Method

In this section, the algebraic dual-energy method is employed in the calculation of static inductance. A proof on the existence of upper and lower inductance bounds for arbitrarily-shaped, three-dimensional linear inductors is given. Two examples with known analytic solutions are considered to illustrate the application of the method. The steps taken are described in detail and the issues involved in the application of the method are identified.

2.4.1 Existence of Upper and Lower Inductance Bounds

Consider the arbitrary inductor of Figure 2-7. It is surrounded by a closed surface S , enclosing a volume V of spatially-varying permeability, μ . The surface S can be subdivided into two open surfaces S_{\parallel} and S_{\perp} , so that $S = S_{\perp} \cup S_{\parallel}$. S_{\parallel} is the portion of S over which the value of the magnetic vector potential is prescribed and S_{\perp} is the portion over which the normal derivative of the potential is given. These correspond to Dirichlet and Neumann boundary conditions, respectively.

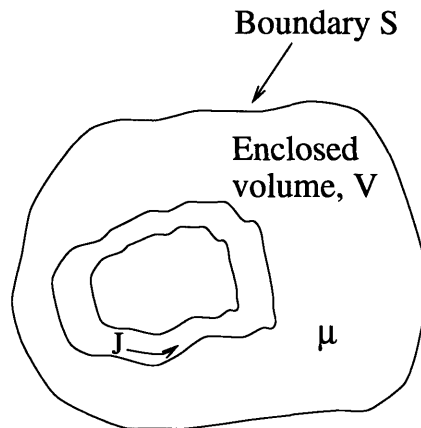


Figure 2-7: General inductor definition

The static inductance, L , of the inductor is obtained by first solving Maxwell's

equations describing the system

$$\nabla \cdot \mathbf{B} = 0 \Rightarrow \mathbf{B} = \nabla \times \mathbf{A} \quad (2.68)$$

$$\nabla \times \mathbf{H} = \mathbf{J} \quad (2.69)$$

$$\mathbf{B} = \mu \mathbf{H} \quad (2.70)$$

subject to the boundary conditions imposed. \mathbf{A} is the magnetic vector potential, \mathbf{J} is the current density, \mathbf{B} is the magnetic flux density and \mathbf{H} is the magnetic field intensity. The inductance can be subsequently calculated using either of two ways. On the one hand, $L = \frac{\lambda}{i}$, where λ is the total magnetic flux linked by the winding, carrying a current i . On the other hand, $L = \frac{2W_m}{i^2}$, where W_m is the stored magnetic energy of the system, given by

$$W_m = \frac{1}{2} \int_V \mathbf{B} \cdot \mathbf{H} dV = \frac{1}{2} \int_V \mathbf{A} \cdot \mathbf{J} dV. \quad (2.71)$$

It is important to note that the second equality in (2.71) holds under the condition that

$$\oint_S (\mathbf{A} \times \mathbf{H}) \cdot d\mathbf{S} = 0. \quad (2.72)$$

Equation (2.71) is usually presented in the literature for problems where the surface $S \rightarrow \infty$ [42]; then the magnetic vector potential decreases as $\frac{1}{r}$, the magnetic field decreases as $\frac{1}{r^2}$, and although the surface S increases as r^2 , the product $(\mathbf{A} \times \mathbf{H}) \cdot d\mathbf{S}$ decreases as $\frac{1}{r}$. Hence, in the limit as $r \rightarrow \infty$, the integral of (2.72) vanishes. But for the problems considered here, S has finite dimensions and the enclosed fields will not necessarily decrease to zero with increasing r . However, condition (2.72) will still hold in this case, since

$$\oint_S (\mathbf{A} \times \mathbf{H}) \cdot d\mathbf{S} = \oint_S \mathbf{A} \cdot (\mathbf{H} \times d\mathbf{S}) = \int_{S_\perp} \mathbf{A} \cdot (\mathbf{H} \times d\mathbf{S}) + \int_{S_\parallel} \mathbf{A} \cdot (\mathbf{H} \times d\mathbf{S}) = 0 \quad (2.73)$$

This is because, by definition, $\mathbf{H} \times d\mathbf{S} = \mathbf{0}$ on S_\perp and $\mathbf{A} = \mathbf{0}$ on S_\parallel . As a result, (2.71) is still valid for the problem and boundary conditions under consideration in

this section.

Analytic bounds for the inductance can be found by calculating lower and upper bounds to the stored system energy. A lower energy bound, W_{lower} , can be obtained by first adopting a function \mathbf{A}_L to approximate the magnetic vector potential, \mathbf{A} , in V . \mathbf{A}_L need only satisfy the Dirichlet boundary conditions on $S_{||}$; it is otherwise unconstrained. The corresponding \mathbf{B}_L and \mathbf{H}_L are computed using Maxwell's equations

$$\mathbf{B}_L = \nabla \times \mathbf{A}_L \quad (2.74)$$

$$\mathbf{H}_L = \frac{1}{\mu} \mathbf{B}_L. \quad (2.75)$$

They need not satisfy their boundary conditions on S_{\perp} , nor Ampere's law. A lower energy bound is computed using the functional

$$W_{lower} = \int_V \mathbf{A}_L \cdot \mathbf{J} \, dV - \frac{1}{2} \int_V \mathbf{B}_L \cdot \mathbf{H}_L \, dV \quad (2.76)$$

and a lower bound for the inductance, L_{lower} , is found using

$$L_{lower} = \frac{2 W_{lower}}{i^2} \leq \frac{2 W_m}{i^2} = L. \quad (2.77)$$

Note that $L_{lower} = L$ if and only if $\mathbf{A}_L = \mathbf{A}$.

In order to prove that $W_{lower} \leq W_m$, define $\delta\mathbf{A}_L$ such that $\mathbf{A}_L = \mathbf{A} + \delta\mathbf{A}_L$. In a similar and consistent manner, define $\delta\mathbf{B}_L$ and $\delta\mathbf{H}_L$, such that $\mathbf{B}_L = \mathbf{B} + \delta\mathbf{B}_L$ and $\mathbf{H}_L = \mathbf{H} + \delta\mathbf{H}_L$. Then

$$\begin{aligned} W_{lower} &= \int_V \mathbf{A}_L \cdot \mathbf{J} \, dV - \frac{1}{2} \int_V \mathbf{B}_L \cdot \mathbf{H}_L \, dV \\ &= \int_V (\mathbf{A} + \delta\mathbf{A}_L) \cdot \mathbf{J} \, dV - \frac{1}{2} \int_V (\mathbf{B} + \delta\mathbf{B}_L) \cdot (\mathbf{H} + \delta\mathbf{H}_L) \, dV \\ &= W_m + \int_V \delta\mathbf{A}_L \cdot \mathbf{J} \, dV - \int_V \mathbf{H} \cdot \delta\mathbf{B}_L \, dV - \frac{1}{2} \int_V \mu \delta\mathbf{H}_L \cdot \delta\mathbf{H}_L \, dV \\ &= W_m + \int_V \delta\mathbf{A}_L \cdot (\nabla \times \mathbf{H}) \, dV - \int_V \mathbf{H} \cdot \delta\mathbf{B}_L \, dV - \frac{1}{2} \int_V \mu \delta\mathbf{H}_L \cdot \delta\mathbf{H}_L \, dV \\ &= W_m - \int_V \nabla \cdot (\delta\mathbf{A}_L \times \mathbf{H}) \, dV + \int_V \mathbf{H} \cdot (\nabla \times \delta\mathbf{A}_L) \, dV \end{aligned}$$

$$\begin{aligned}
& - \int_V \mathbf{H} \cdot \delta \mathbf{B}_L dV - \frac{1}{2} \int_V \mu \delta \mathbf{H}_L \cdot \delta \mathbf{H}_L dV \\
= & W_m - \oint_S (\delta \mathbf{A}_L \times \mathbf{H}) \cdot d\mathbf{S} - \frac{1}{2} \int_V \mu \delta \mathbf{H}_L \cdot \delta \mathbf{H}_L dV \\
= & W_m - \int_{S_\perp} (\delta \mathbf{A}_L \times \mathbf{H}) \cdot d\mathbf{S}_\perp - \int_{S_\parallel} (\delta \mathbf{A}_L \times \mathbf{H}) \cdot d\mathbf{S}_\parallel - \frac{1}{2} \int_V \mu \delta \mathbf{H}_L \cdot \delta \mathbf{H}_L dV \\
= & W_m - \int_{S_\parallel} (\delta \mathbf{A}_L \times \mathbf{H}) \cdot d\mathbf{S}_\parallel - \int_{S_\perp} \delta \mathbf{A}_L \cdot (\mathbf{H} \times d\mathbf{S}_\perp) - \frac{1}{2} \int_V \mu \delta \mathbf{H}_L \cdot \delta \mathbf{H}_L dV \\
= & W_m - \frac{1}{2} \int_V \mu \delta \mathbf{H}_L \cdot \delta \mathbf{H}_L dV \\
\leq & W_m. \tag{2.78}
\end{aligned}$$

The third equality holds because, by definition, $\delta \mathbf{B}_L = \mu \delta \mathbf{H}_L$. The sixth equality holds because, by definition, $\delta \mathbf{B}_L = \nabla \times \delta \mathbf{A}_L$. The last equality holds because, by construction, $\delta \mathbf{A}_L = \mathbf{0}$ on S_\parallel and $\mathbf{H} \times d\mathbf{S} = \mathbf{0}$ on S_\perp .

Similarly, an upper bound for L may be obtained by adopting a function \mathbf{H}_U to approximate \mathbf{H} in V . \mathbf{H}_U is forced to satisfy Ampere's law (2.69) and the Neumann boundary conditions on S_\perp , but it need not satisfy any boundary conditions on S_\parallel , nor Gauss' law (2.68). Using

$$\mathbf{B}_U = \mu \mathbf{H}_U \tag{2.79}$$

an upper bound for the stored system energy can be obtained using the functional

$$W_{upper} = \frac{1}{2} \int_V \mathbf{B}_U \cdot \mathbf{H}_U dV \tag{2.80}$$

and an upper bound for the inductance, L_{upper} , can be calculated using

$$L_{upper} = \frac{2 W_{upper}}{i^2} \geq \frac{2 W_m}{i^2} = L. \tag{2.81}$$

Note that $L_{upper} = L$ if and only if $\mathbf{H}_U = \mathbf{H}$.

In order to prove that $W_{upper} \geq W_m$, define $\delta \mathbf{H}_U$ such that $\mathbf{H}_U = \mathbf{H} + \delta \mathbf{H}_U$. In a similar and consistent manner, define $\delta \mathbf{B}_U$ such that $\mathbf{B}_U = \mathbf{B} + \delta \mathbf{B}_U$. Since \mathbf{H}_U is chosen to satisfy the curl condition,

$$\nabla \times \mathbf{H}_U = \mathbf{J} \Rightarrow \nabla \times (\mathbf{H} + \delta \mathbf{H}_U) = \mathbf{J} \Rightarrow \nabla \times \delta \mathbf{H}_U = \mathbf{0}. \tag{2.82}$$

Thus, $\delta\mathbf{H}_U$ is curl free. Therefore, there exists a magnetic scalar potential $\delta\Psi_U$, such that $\delta\mathbf{H}_U = -\nabla\delta\Psi_U$. Then,

$$\begin{aligned}
W_{upper} &= \frac{1}{2} \int_V \mathbf{B}_U \cdot \mathbf{H}_U \, dV \\
&= \frac{1}{2} \int_V (\mathbf{B} + \delta\mathbf{B}_U) \cdot (\mathbf{H} + \delta\mathbf{H}_U) \, dV \\
&= W_m + \int_V \mathbf{B} \cdot \delta\mathbf{H}_U \, dV + \frac{1}{2} \int_V \mu \delta\mathbf{H}_U \cdot \delta\mathbf{H}_U \, dV \\
&= W_m - \int_V \mathbf{B} \cdot \nabla\delta\Psi_U \, dV + \frac{1}{2} \int_V \mu \delta\mathbf{H}_U \cdot \delta\mathbf{H}_U \, dV \\
&= W_m - \int_V \nabla \cdot (\delta\Psi_U \mathbf{B}) \, dV + \int_V \delta\Psi_U \nabla \cdot \mathbf{B} \, dV \\
&\quad + \frac{1}{2} \int_V \mu \delta\mathbf{H}_U \cdot \delta\mathbf{H}_U \, dV \\
&= W_m - \oint_S \delta\Psi_U \mathbf{B} \cdot d\mathbf{S} + \frac{1}{2} \int_V \mu \delta\mathbf{H}_U \cdot \delta\mathbf{H}_U \, dV \\
&= W_m - \int_{S_\perp} \delta\Psi_U \mathbf{B} \cdot d\mathbf{S}_\perp - \int_{S_\parallel} \delta\Psi_U \mathbf{B} \cdot d\mathbf{S}_\parallel + \frac{1}{2} \int_V \mu \delta\mathbf{H}_U \cdot \delta\mathbf{H}_U \, dV \\
&= W_m + \frac{1}{2} \int_V \mu \delta\mathbf{H}_U \cdot \delta\mathbf{H}_U \, dV \\
&\geq W_m.
\end{aligned} \tag{2.83}$$

The third equality holds because, by definition, $\delta\mathbf{B}_U = \mu \delta\mathbf{H}_U$. The fourth equality holds because, by definition, $\delta\mathbf{H}_U = -\nabla \delta\Psi_U$. The sixth equality holds because $\nabla \cdot \mathbf{B} = 0$ in the inductor volume. Finally, the last equality is obtained since $\delta\Psi_U = 0$ on S_\parallel and $\mathbf{B} \cdot d\mathbf{S} = 0$ on S_\perp .

2.4.2 Application of the ADEM to Inductance Computation

Applying the algebraic dual-energy method, a lower bound for the static inductance can be obtained as follows.

- Guess a spatial distribution for the magnetic vector potential, \mathbf{A}_L , which satisfies the boundary conditions for \mathbf{A} . Each component of \mathbf{A}_L can be an approxi-

mation of the form

$$A_{L_{x,y,z}} = \sum_{i=0}^{i=K} \gamma_{i_{x,y,z}} N_{i_{x,y,z}}(x, y, z) \quad (2.84)$$

where K is the number of free coefficients, $\gamma_{i_{x,y,z}}$ are the free coefficients to be calculated, and $N_{i_{x,y,z}}$ are the trial functions in x , y and z . Imposing the boundary conditions for \mathbf{A} will constrain some (or all) of the free coefficients $\gamma_{i_{x,y,z}}$.

- Obtain the corresponding magnetic flux density distribution, \mathbf{B}_L , from

$$\mathbf{B}_L = \nabla \times \mathbf{A}_L. \quad (2.85)$$

- Calculate the corresponding magnetic field intensity from

$$\mathbf{H}_L = \frac{\mathbf{B}_L}{\mu}. \quad (2.86)$$

- Obtain the lower energy bound, W_{lower} , from

$$W_{lower} = \int_V \mathbf{A}_L \cdot \mathbf{J} dV - \frac{1}{2} \int_V \mathbf{B}_L \cdot \mathbf{H}_L dV \quad (2.87)$$

where V is the volume of the geometry at hand.

- Calculate any remaining free coefficients, $\gamma_{i_{x,y,z}}$, by extremizing W_{lower} by solving the algebraic set of equations

$$\frac{\partial W_{lower}}{\partial \gamma_{i_{x,y,z}}} = 0. \quad (2.88)$$

- Obtain the lower bound for the inductance from

$$L_{lower} = \frac{2 W_{lower}}{i^2} \leq \frac{2 W_m}{i^2} = L \quad (2.89)$$

where i is the current flowing through the winding.

Similarly an inductance upper bound is obtained as follows.

- Guess a spatial distribution for the magnetic field intensity, \mathbf{H}_U , which satisfies the boundary conditions for \mathbf{H} and the curl condition

$$\nabla \times \mathbf{H}_U = \mathbf{J}. \quad (2.90)$$

Again, each component of \mathbf{H}_U can be an approximation of the form

$$H_{U_{x,y,z}} = \sum_{i=0}^{i=K} \delta_{i_{x,y,z}} N_{i_{x,y,z}}(x, y, z) \quad (2.91)$$

where K is the number of free coefficients, $\delta_{i_{x,y,z}}$ are the free coefficients to be calculated, and $N_{i_{x,y,z}}$ are the trial functions in x , y , and z . Imposing the boundary conditions for \mathbf{H} and Ampere's law will constrain some, or all, of the free coefficients $\delta_{i_{x,y,z}}$.

- Calculate the corresponding magnetic flux density from

$$\mathbf{B}_U = \mu \mathbf{H}_U. \quad (2.92)$$

- Calculate the upper energy bound, W_{upper} , from

$$W_{upper} = \frac{1}{2} \int_V \mathbf{B}_U \cdot \mathbf{H}_U dV \quad (2.93)$$

where V is the volume of the geometry at hand.

- Calculate any remaining free coefficients, $\delta_{i_{x,y,z}}$, by extremizing W_{upper} , by solving the algebraic set of equations

$$\frac{\partial W_{upper}}{\partial \delta_{i_{x,y,z}}} = 0. \quad (2.94)$$

- Obtain the upper bound for the inductance from

$$L_{upper} = \frac{2 W_{upper}}{i^2} \geq \frac{2 W_m}{i^2} = L. \quad (2.95)$$

2.4.3 Example: T-inductor

This section illustrates the application of the ADEM to the computation of inductance. The T-inductor provides the basis for this example. Figure 2-8 provides a definition of the geometry for the T-inductor. The problem can be found in [7], [25] and consists of a conductor carrying a uniform current density $J = 1 \text{ A/m}^2$. The

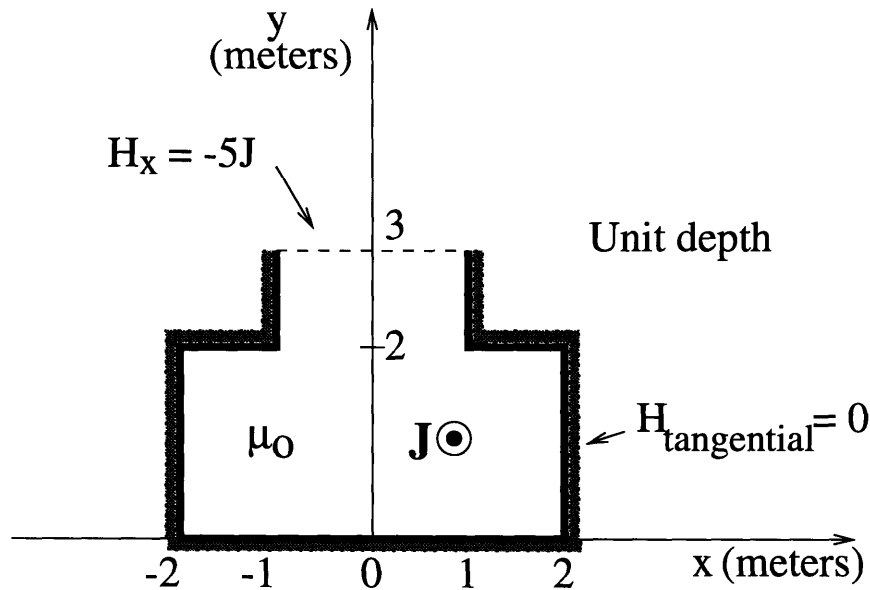


Figure 2-8: Geometry of the T-inductor problem

presence of highly permeable iron on the bottom and sides, and the imposition of $H_x = -5J$ at the top, define the boundary conditions for this problem. The exact value of the problem inductance is

$$L = 0.57 \mu_0. \quad (2.96)$$

Hammond [7] obtains the lower inductance bound by adopting a trial function $A_L = b y$. Hence $B_x = b$ and $B_y = 0$. Substitution into his lower bound functional

yields

$$W_{lower} = -\frac{5 b^2}{\mu_o} + 13 b J - 30 b J. \quad (2.97)$$

This functional is maximized at

$$\frac{\partial W_{lower}}{\partial b} = 0 \Rightarrow b = -1.7 \mu_o J. \quad (2.98)$$

Substitution back into equation (2.97) gives

$$W_{lower} = 14.45 \mu_o J^2 \quad (2.99)$$

and hence

$$L_{lower} = \frac{2 W_{lower}}{i^2} = 0.289 \mu_o. \quad (2.100)$$

Hammond's calculation of the upper inductance bound begins by adopting a linear approximation for the field

$$\mathbf{H}_U = -\frac{5}{3} y J \hat{\mathbf{x}}. \quad (2.101)$$

Substitution into the upper bound energy functional, yields

$$W_{upper} = 32.41 \mu_o J^2 \quad (2.102)$$

which implies a

$$L_{upper} = \frac{2 W_{upper}}{i^2} = 0.648 \mu_o. \quad (2.103)$$

It is interesting to note that Hammond's guess of magnetic field intensity does not satisfy Ampere's law, nor all the boundary conditions for \mathbf{H} . As a result, his guess does not guarantee an upper energy bound and is not theoretically justified. A possible reason for the success of his guess is the definition of the symmetry boundary condition on the top of the slot as $H_x = -5 J$, instead of as $A = 0$. This has the advantage of introducing J , the current density and problem energy source, into the guessed solution. As a result, the guessed distribution is "anchored" about J without the need to satisfy the $\nabla \times \mathbf{H} = \mathbf{J}$ condition; the chances of obtaining an upper bound

are significantly increased.

The derivations and implementation steps outlined in the previous section are employed next to obtain the desired bounds. The method is not essentially different from Hammond's but use is made of a more structured methodology. The lower inductance bound can be obtained by assuming a first order polynomial approximation in x and y for \mathbf{A}_L throughout the slot geometry. Thus,

$$\mathbf{A}_L = A_z \hat{\mathbf{z}} = (\alpha_1 + \alpha_2 x + \alpha_3 y) \hat{\mathbf{z}}. \quad (2.104)$$

\mathbf{A}_L must satisfy the Dirichlet boundary conditions, namely $A_z = 0$ at $y = 3$. This implies

$$\alpha_1 + \alpha_2 x + 3 \alpha_3 = 0 \Rightarrow \alpha_2 = 0, \alpha_1 = -3 \alpha_3. \quad (2.105)$$

Hence

$$A_z = \alpha_3 (y - 3) \quad (2.106)$$

and

$$\mathbf{B}_L = \frac{\partial A_z}{\partial y} \hat{\mathbf{x}} - \frac{\partial A_z}{\partial x} \hat{\mathbf{y}} = \alpha_3 \hat{\mathbf{x}} \quad (2.107)$$

so that

$$\mathbf{H}_L = \frac{\alpha_3}{\mu} \hat{\mathbf{x}}. \quad (2.108)$$

Calculation of the lower energy functional per unit depth then gives

$$\begin{aligned} W_{lower} &= \int_V \mathbf{A}_L \cdot \mathbf{J} dV - \frac{1}{2} \int_V \mathbf{B}_L \cdot \mathbf{H}_L dV \\ &= J \int_{y=0}^2 \int_{x=-2}^2 \alpha_3 (y - 3) dx dy + J \int_{y=2}^3 \int_{x=-1}^1 \alpha_3 (y - 3) dx dy \\ &\quad - \frac{1}{2\mu} \int_{y=0}^2 \int_{x=-2}^2 \alpha_3^2 dx dy - \frac{1}{2\mu} \int_{y=2}^3 \int_{x=-1}^1 \alpha_3^2 dx dy \\ &= -17 \alpha_3 J - \frac{5\alpha_3^2}{\mu_o}. \end{aligned} \quad (2.109)$$

Finally,

$$\frac{\partial W_{lower}}{\partial \alpha_3} = 0 \Rightarrow \alpha_3 = -1.7 \mu_o J. \quad (2.110)$$

Substituting back into (2.109) yields

$$W_{lower} = 14.45 \mu_o J^2 \quad (2.111)$$

and

$$L_{lower} = 0.289 \mu_o. \quad (2.112)$$

This result is the same as Hammond's but has been reached using the $A = 0$ symmetry boundary condition at the top and a more structured methodology.

In order to calculate an upper bound, a field approximation must be adopted that satisfies (2.90), as well as the boundary conditions at all iron surfaces, namely $H_x = 0$ at $y = 0$ and $y = 2$, $H_y = 0$ at $x = \pm 2$ for $0 \leq y \leq 2$, and $H_y = 0$ at $x = \pm 1$ for $2 \leq y \leq 3$. It is unnecessarily difficult to match these boundary conditions using a finite set of polynomial approximations for \mathbf{H} . A way to simplify this task is to break the geometry into six elements and then proceed to find the upper bound. The element discretization is given in Figure 2-9. Discretization imposes the further

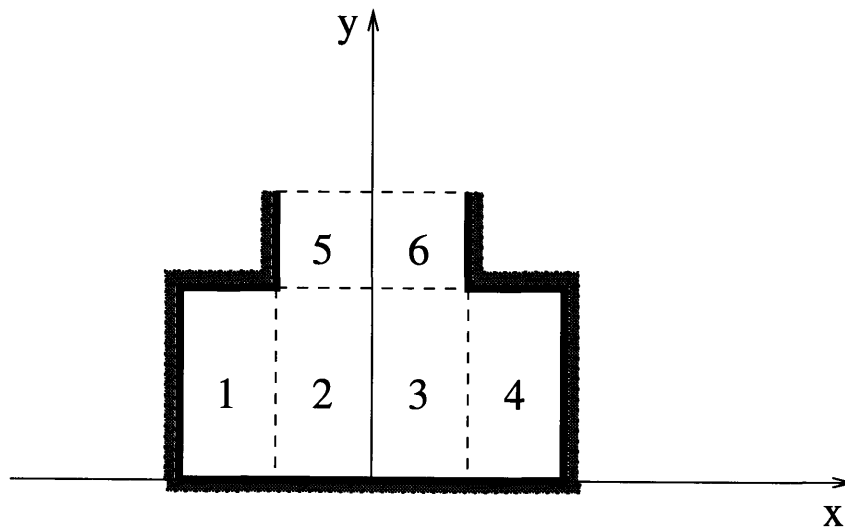


Figure 2-9: Six-element discretization for the T-slot problem

requirement that the tangential component of \mathbf{H}_U should be continuous at all element interfaces. This will further constrain some of the free coefficients. Appendix C at the end of this chapter includes the Maple V code that will generate an upper bound

for this problem using second order polynomial approximations. The code yields

$$W_{upper} = 30.4968725 \mu_o J^2 \quad (2.113)$$

which implies an upper inductance bound of

$$L_{upper} = 0.6099374 \mu_o. \quad (2.114)$$

The average of the two inductance bounds is

$$L_{average} = \frac{L_{upper} + L_{lower}}{2} = 0.4494687 \mu_o \quad (2.115)$$

which is close to the exact value of $0.57 \mu_o$. Increasing the order of approximation for the field distributions improves the energy bounds. While the accuracy of each energy functional improves with the order of approximation, the average of the upper and lower bounds does not necessarily improve.

2.4.4 Example: Slot with Perfectly Conducting Walls

Figure 2-10 provides the definition of the geometry considered here. The problem can be found in [41] and consists of a rectangular winding slot surrounded by perfectly conducting walls. The wires comprising the winding carry a current in the $-z$ direction over the range $0 < x < a$ and are uniformly distributed in the slot. The return current path is defined over the range $-a < x < 0$. Hence, the current density in the $\pm z$ -direction depends on the number of turns N and the current magnitude flowing through the winding. For simplicity, the geometry is assumed uniform with a depth D in the z -direction, so that a two-dimensional analysis can be employed. The problem is also symmetric about the y -axis, so that only half the geometry need be considered. The goal is the calculation of the inductance and the stored magnetic energy of the structure.

The describing equation is Poisson's equation for the magnetic vector potential so

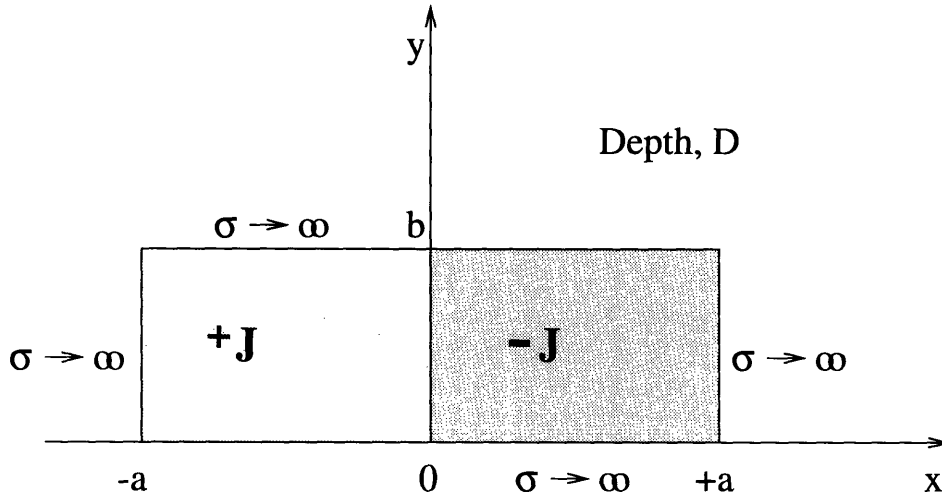


Figure 2-10: Rectangular slot with perfectly conducting walls

that

$$\nabla^2 A_z = \mu_0 J \quad (2.116)$$

in the volume. The perfectly conducting walls require that the normal flux density, and hence A_z , is zero along the inductor boundaries. An analytic expression for A_z can be obtained through the addition of a homogeneous and a particular solution. Hence an analytic expression for the total flux linked by the winding is obtained by integrating over the inductor area. An analytic expression for the inductance of the system is found to be

$$L = 2 \mu_0 \left(\frac{N}{A}\right)^2 D \sum_{n=\text{odd}}^{\infty} \frac{16}{n\pi} \left(\frac{a}{n\pi}\right)^4 \left[\frac{n\pi b}{2a} - \tanh\left(\frac{n\pi b}{2a}\right) \right] \quad (2.117)$$

where $A = a b$ is the winding area. Finally, the stored magnetic energy can be obtained from

$$W_m = \frac{1}{2} L i^2 = \mu_0 \left(\frac{N i}{A}\right)^2 D \sum_{n=\text{odd}}^{\infty} \frac{16}{n\pi} \left(\frac{a}{n\pi}\right)^4 \left[\frac{n\pi b}{2a} - \tanh\left(\frac{n\pi b}{2a}\right) \right]. \quad (2.118)$$

Assuming values for the different parameters, this equation can be easily programmed in C code and the sum to a large number of terms can be determined. For simplicity, unit length in the z -direction is assumed and $a = b = 0.05m$. The

excitation consists of a winding of $N = 100$ turns, with a current of $i = 25A$ flowing through each turn. This gives rise to a current density of $10^6 A/m^2$. Using 20,000 terms in (2.118), the value of stored magnetic energy is found to be

$$W_m = 0.2760223234 J \tag{2.119}$$

exact to 10 decimal places. As an extra check on this value, an approximate value for W_m can be obtained using the finite element method. Quickfield [63] yields a value of 0.27594 J with 57,200 nodes, which accurately compares with the exact value in (2.119). Figure 2-11 provides the magnetic field profile obtained from this finite element analysis.

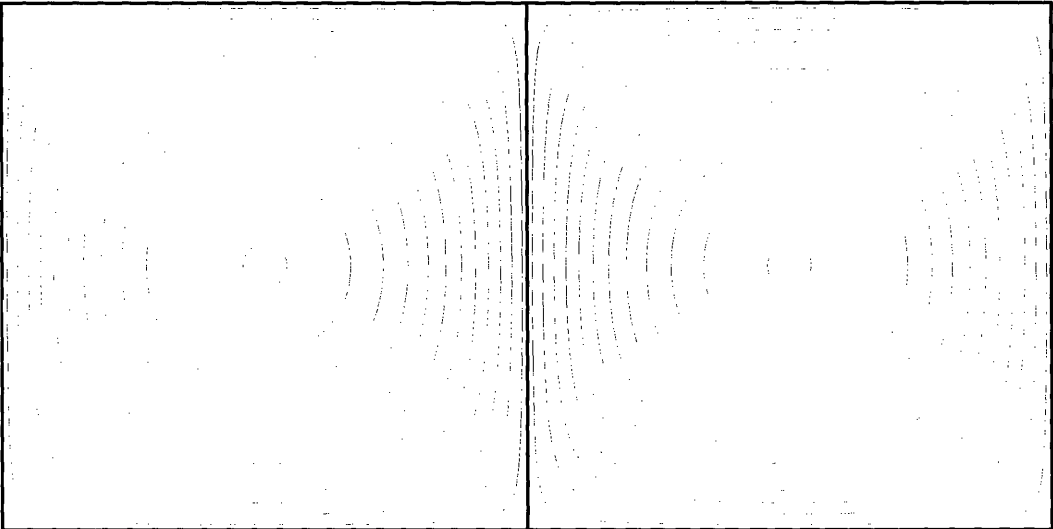


Figure 2-11: Field plot for rectangular slot with perfectly conducting walls

One can now proceed to calculate analytic upper and lower bounds for the energy of this problem, using the algebraic dual-energy method.

Lower Energy Bound

Using the symmetry of the problem about the y -axis, the boundary conditions for the assumed A_L are $A_z = 0$ at $x = 0, x = a, y = 0, y = b$. A polynomial approximation in x and y is assumed for A_z , such that the boundary conditions on A_z are satisfied.

Lower bound for $\sigma \rightarrow \infty$		
Order of approximation	Stored energy (J)	Error (J)
1st	-	-
2nd	-	-
3rd	-	-
4th	0.2727076956	3.31462e-3
5th	0.2727076956	3.31462e-3
6th	0.2756612085	3.61115e-4

Table 2.2: Lower energy bounds for rectangular slot problem

First, second and third order polynomial approximations do not provide enough free coefficients to satisfy all boundary conditions. Fourth, fifth and sixth order approximations, however, give the results of Table 2.2, obtained using Maple V [40]. The error in the calculated stored energy is very small.

Upper Energy Bound

For the particular problem, no boundary conditions on \mathbf{H} are present. As a result, a first order approximation that satisfies the condition

$$\nabla \times \mathbf{H} = \mathbf{J} \quad (2.120)$$

is

$$H_x = \alpha_1 + \alpha_2 x + \alpha_3 y \quad (2.121)$$

$$H_y = \alpha_4 + (\alpha_3 + J) x + \alpha_5 y. \quad (2.122)$$

Using Maple V again, this yields an energy value of 0.3272492347 J . Increasing the order of approximation yields a very accurate energy value, as shown in Table 2.3.

Upper bound for $\sigma \rightarrow \infty$		
Order of approximation	Stored energy (J)	Error (J)
1st	0.32724923474	0.0512269
2nd	0.32724923474	0.0512269
3rd	0.27634379823	0.0003214

Table 2.3: Upper energy bounds for rectangular slot problem

2.5 Further Thoughts on the Application of the Algebraic Dual-Energy Method

From the examples presented above, a number of conclusions can be drawn on the algebraic dual-energy method and its application. First, it is interesting to note that there are two types of sources involved in these problems, namely curl and divergence sources. In the calculation of the lower bound, the divergence condition is automatically satisfied, but Ampere's law is not. This physically implies the introduction of an additional current density within the volume of the problem. The calculation of the upper bound however, ensures that the curl condition is satisfied. Gauss' law is not necessarily satisfied in this case, and this can be physically interpreted as the introduction of divergence sources, or magnetic charge, into the system volume.

The problems considered in this chapter have two common characteristics. They are all two-dimensional and, for simplicity, they all consist of a single material with uniform electric or magnetic properties; the resistor and capacitor geometries consist of materials of constant σ and ϵ , respectively, while the inductor problems consist of current densities and permeabilities, uniformly distributed throughout their volumes. In the following chapter, the variable reluctance motor geometry is considered; it consists of regions with different electrical and magnetic properties. In such cases, the geometry to be analyzed should be subdivided into regions, or elements, of different properties, as suggested in [25]. The total system energy, both upper and lower bounds, can be subsequently calculated by summing the contributions from the elemental functionals. The advantage of such an approach is that the system is broken up into a set of subsystems; an algorithm could be adopted to assign different weight on the various contributions from elemental energies, thus reducing computational time and cost. Moreover, the increased number of elements improves the accuracy of the solution by providing an increase in the number of degrees of freedom. The disadvantages, however, involve those encountered in the usual finite-element methods. When the domain of the problem is to be discretized, one has to ensure continuity of the fields along element interfaces. Moreover, in a finite-element implementation, a

compromise must be reached between the mesh density and the required accuracy of solution. In reaching this compromise, one has to factor in issues such as the shape of the elements and the order of polynomial approximations employed.

The key advantage of the algebraic dual-energy method is that, while it requires many degrees of freedom to calculate a reasonably accurate value of energy using a conventional “single-sided” finite element method, equally accurate results can be computed simply by averaging the two less accurate bounds found using a small number of degrees of freedom. However, upper and lower bounds are not necessarily symmetric about the exact value. As a result, equidistance of the bounds from the true solution is not guaranteed and the average of the two bounds may be an estimate worse than one of the bounds. Chapter 3 provides an error analysis of the algebraic dual-energy method which forms the basis for an algorithm guaranteeing the equidistance of the bounds.

The examples of this chapter demonstrate that the bounds obtained can only be as good as the set of trial functions adopted. In theory, an infinite number of basis functions would yield the exact solution. In reality however, one cannot employ an infinite number of basis functions. Some consideration is appropriate as to the choice of basis functions, since some families of basis functions may be more successful in reducing the error.

Last but not least, the task of obtaining appropriate energy functionals is not trivial. The present literature addresses only a restricted range of problems so that the energy functionals proposed in this chapter can be used. However, one should bear in mind that these functionals are not universally applicable. This is because they are partially dependent on the boundary conditions, which can be specified in an unlimited number of ways. Consider for example, the case of a conductor of arbitrary shape between two electrodes. If the electrodes are each set to a known constant potential, then the ADEM will provide both bounds to the resistance of the problem. If however, a spatially-varying potential distribution was to be assumed along the surface of one or both electrodes, the method would not work in the upper bound case. This is because a current distribution cannot be defined a priori in this case to

match the real current distribution at the electrode. An upper bound to the resistance would be therefore impossible to derive.

2.6 Appendix A: Maple Code for Resistance Bounds Calculation

This Appendix provides the Maple V code employed to generate upper and lower resistance bounds to the right-angled conductor of Section 2.2.2.

```
# UPPER BOUND RESISTANCE CALCULATION
# SIGMA AND D ASSUMED UNITY
a2 := -(Is + 3*a5);
# APPROXIMATION FOR Tu
Tu := a1 + a2*x + a5*x*x;
Tu := simplify(Tu);
# CORRESPONDING J-FIELD COMPONENTS
Jx := diff(Tu,y);
Jy := -diff(Tu,x);
# OBTAIN THE SQUARE OF THE MAGNITUDE OF THE J-FIELD
Jsq := simplify(Jx*Jx+Jy*Jy);
# INTEGRATE J^2 OVER 1/2 OF THE PROBLEM REGION
int1 := int(Jsq, y=0..x);
Pu := int(int1, x=1..2);
# SIMPLIFY THE POWER EXPRESSION
Pu := simplify(Pu);
# EXPRESSION FOR TOTAL RESISTANCE (UPPER BOUND)
Ru := (2*Pu)/I^2;
# GET VALUES OF FREE PARAMETER, a5, THAT EXTREMIZES THE POWER EXPRESSION
da5 := simplify(diff(Pu,a5));
solutionset := solve({da5},{a5});
```

```

# SUBSTITUTE VALUE OF a5 IN EXPRESSION FOR Ru
Ru := subs(solutionset,Ru);

# LOWER BOUND RESISTANCE CALCULATION
# SIGMA AND D ASSUMED UNITY
# APPROXIMATION FOR PHI
Phi := V*y/(2*x);
# CORRESPONDING E-FIELD COMPONENTS
Ex := -diff(Phi,x);
Ey := -diff(Phi,y);
# OBTAIN THE SQUARE OF THE MAGNITUDE OF THE E-FIELD
Esq := simplify(Ex*Ex+Ey*Ey);
# INTEGRATE E^2 OVER 1/2 OF THE PROBLEM REGION
int1 := int(Esq,y=0..x);
P1 := int(int1, x=1..2);
# SIMPLIFY THE POWER EXPRESSION
P1 := simplify(P1);
# EXPRESSION FOR TOTAL RESISTANCE
R1 := V*V/(2*P1);

```

2.7 Appendix B: Capacitance Bounds for Tubular Capacitor

In this Appendix, the algebraic dual-energy method is applied to a closed capacitance problem with a known analytic solution, following the analysis of Section 2.3. To obtain a C_{lower} , the following steps are taken.

- Guess a displacement flux density distribution, \mathbf{D}_L , which satisfies the boundary condition for \mathbf{D} on S_\perp

$$\mathbf{D}_L \cdot d\mathbf{S} = 0 \quad (2.123)$$

as well as the relation

$$\nabla \cdot \mathbf{D}_L = 0 \quad (2.124)$$

in the capacitor volume. Each component of \mathbf{D}_L can be an approximation of the form

$$D_{i_x, y, z} = \sum_{i=0}^{i=K} k_{i_x, y, z} N_{i_x, y, z}(x, y, z) \quad (2.125)$$

where K is the number of free coefficients, $k_{i_x, y, z}$ are the free coefficients to be calculated, and $N_{i_x, y, z}$ are the trial functions in x , y and z . Imposing the boundary conditions for \mathbf{D} will constrain some, or all, of the free coefficients $k_{i_x, y, z}$.

- Set

$$Q_C = \oint_{S_+} \mathbf{D}_L \cdot d\mathbf{S} \quad (2.126)$$

where Q_C is the total charge on the positive terminal of the capacitor.

- Obtain the corresponding electric field distribution, \mathbf{E}_L , from

$$\mathbf{E}_L = \frac{1}{\epsilon} \mathbf{D}_L. \quad (2.127)$$

- Calculate the electric energy stored in the capacitor, W_{lower} , from

$$W_{lower} = \frac{1}{2} \int_V \mathbf{D}_L \cdot \mathbf{E}_L dV. \quad (2.128)$$

- Calculate any remaining free coefficients, $k_{i_x, y, z}$, by extremizing W_{lower} , by solving the algebraic set of equations

$$\frac{\partial W_{lower}}{\partial k_{i_x, y, z}} = 0. \quad (2.129)$$

- Obtain a lower bound for the capacitance from

$$C_{lower} = \frac{Q_C^2}{2 W_{lower}}. \quad (2.130)$$

To obtain an upper capacitance bound, C_{upper} , the following steps are taken.

- Guess a potential distribution, Φ_U , satisfying the boundary conditions for Φ . Φ_U can be an approximation of the form

$$\Phi_U = \sum_{i=0}^{i=K} \lambda_{i_{x,y,z}} N_{i_{x,y,z}}(x, y, z) \quad (2.131)$$

where K is the number of free coefficients, $\lambda_{i_{x,y,z}}$ are the free coefficients to be calculated, and $N_{i_{x,y,z}}$ are the trial functions in x , y and z . Imposing the boundary conditions for Φ will constrain some, or all, of the free coefficients $\lambda_{i_{x,y,z}}$.

- Obtain the corresponding electric field distribution, \mathbf{E}_U , from

$$\mathbf{E}_U = -\nabla\Phi_U. \quad (2.132)$$

- Calculate the electric energy stored in the capacitor, W_{upper} , from

$$W_{upper} = \frac{1}{2} \int_V \epsilon \mathbf{E}_U \cdot \mathbf{E}_U dV. \quad (2.133)$$

- Calculate any remaining free coefficients, $\lambda_{i_{x,y,z}}$, by extremizing W_{upper} , i.e. by solving the algebraic set of equations

$$\frac{\partial W_{upper}}{\partial \lambda_{i_{x,y,z}}} = 0. \quad (2.134)$$

- Obtain the upper bound for the capacitance from

$$C_{upper} = \frac{2 W_{upper}}{V_C^2}. \quad (2.135)$$

Consider the closed tubular capacitor of Figure 2-12(a). It is assumed to have depth D into the paper and a uniform permittivity, ϵ , throughout its volume. The potential difference between its perfectly conducting terminals is V_C . The total charge

Q_C on the positive terminal is constant, yet unknown. The uniformity of the cross-section in the z -direction allows for two-dimensional analysis to be employed. Furthermore, the symmetry that exists about $y = x$, $x = 0$ and $y = 0$ permits analysis of one-eighth of the problem geometry, as shown in Figure 2-3(b). An exact value of the capacitance C is given in [7] as

$$C = 10.25 \epsilon D. \quad (2.136)$$

The algebraic dual-energy method is applied below to obtain analytic upper and

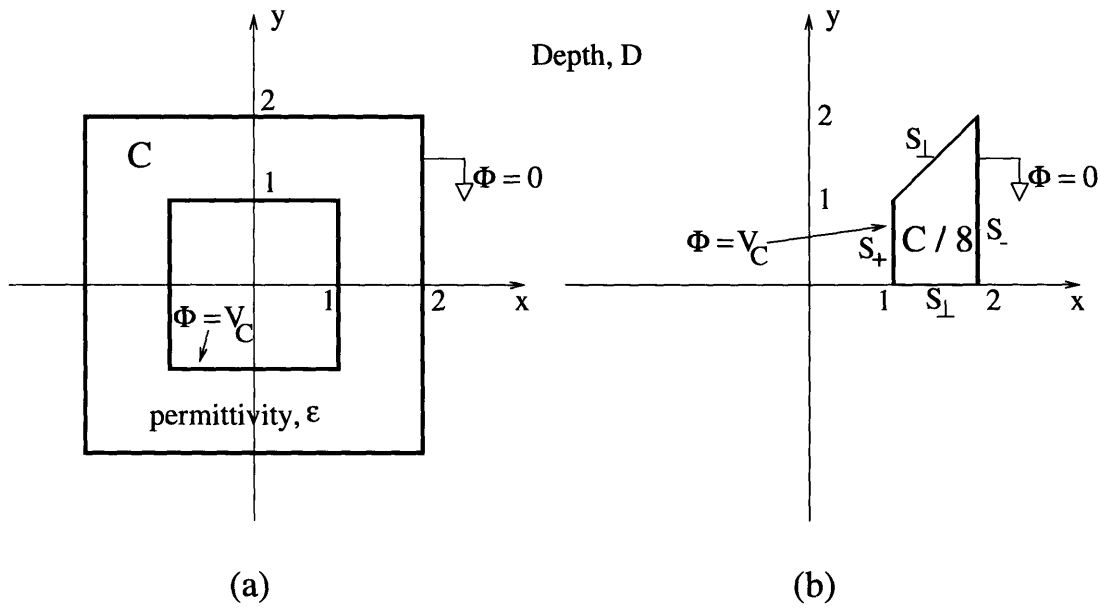


Figure 2-12: Tubular capacitor problem

lower capacitance bounds.

Capacitance Lower Bound: C_{lower}

For convenience, the bounding surface of the capacitor is broken up into three open surfaces, S_+ , S_- , S_\perp , the positive and negative terminals and the remaining bounding surface, respectively. Condition (2.124) can be reinforced by setting

$$\mathbf{D}_L = \nabla \times \mathbf{T}_L. \quad (2.137)$$

For the problem at hand, \mathbf{T}_L has only one component in the z -direction, namely T_L . Considering only one-eighth of the problem due to symmetry, T_L should be forced to satisfy the boundary conditions

- $T_L = 0$ at $y = 0$
- $T_L = 1$ at $y = x$

on S_\perp . An approximation that satisfies these boundary conditions is

$$T_L = \left(\frac{1}{x} - a_6 x\right) y + a_6 y^2. \quad (2.138)$$

The corresponding displacement flux density is

$$\mathbf{D}_L = \frac{\partial T_L}{\partial y} \hat{\mathbf{x}} - \frac{\partial T_L}{\partial x} \hat{\mathbf{y}} = \left(\frac{1}{x} - a_6 x + 2a_6 y\right) \hat{\mathbf{x}} + \left(a_6 y + \frac{y}{x^2}\right) \hat{\mathbf{y}}. \quad (2.139)$$

Set

$$Q_C = \oint_{S_+} \mathbf{D}_L \cdot d\mathbf{S} = - \int_0^1 D_x \text{ at } x=1 \, dy = - \int_0^1 (1 - a_6 + 2 a_6 y) \, dy = -1. \quad (2.140)$$

Then

$$\mathbf{E}_L = \frac{1}{\epsilon} \mathbf{D}_L = \frac{1}{\epsilon} \left[\left(\frac{1}{x} - a_6 x + 2a_6 y\right) \hat{\mathbf{x}} + \left(a_6 y + \frac{y}{x^2}\right) \hat{\mathbf{y}} \right]. \quad (2.141)$$

Assuming unity ϵ and D for simplicity, the electric stored energy in the whole structure is given by

$$\begin{aligned} W_{lower} &= 8 \frac{\epsilon}{2} \int_{V/8} \mathbf{E}_L \cdot \mathbf{E}_L \, dV \\ &= 4 \frac{1}{\epsilon} D \int_{y=0}^x \int_{x=1}^2 \left[\frac{1}{x} - a_6 x + 2a_6 y, a_6 y + \frac{y}{x^2} \right]^2 + \left[a_6 y + \frac{y}{x^2} \right]^2 \, dx \, dy \\ &= 10 a_6^2 + 4 a_6 + 3.696785. \end{aligned} \quad (2.142)$$

Extremizing W_{lower} yields

$$\frac{\partial W_{lower}}{\partial a_6} = 0 \Rightarrow a_6 = -0.2. \quad (2.143)$$

Hence, the lower capacitance bound is found to be

$$C_{lower} = 9.706426216 (F) \quad (2.144)$$

Maple V [40] can be used to generate the above equations. A sample script file is included here and can form the basis for generating better bounds, by increasing the order of approximation and the number of free coefficients.

```
#LOWER BOUND FOR TUBULAR CAPACITOR
#ANALYSIS NORMALIZED TO EPSILON AND DEPTH
# APPROXIMATION FOR D-FIELD COMPONENTS
Dx := (1/x)-a6*x+2*a6*y;
Dy := a6*y+(y/x^2);
# OBTAIN THE SQUARE OF THE MAGNITUDE OF THE D-FIELD
Dsqr := simplify(Dx*Dx+Dy*Dy);
# INTEGRATE D^2 OVER 1/8 OF THE PROBLEM REGION
int1 := 0.5*int(Dsqr,y=0..x);
w1 := int(int1, x=1..2);
# CALCULATE CHARGE Q ON POSITIVE TERMINAL
Dxat1 := subs(x=1,Dx);
Q := int(Dxat1,y=0..1);
# GET TOTAL ENERGY AND SIMPLIFY ITS EXPRESSION
w := simplify(w1);
# EXPRESSION FOR 1/8 OF CAPACITANCE
C := (Q)^2/(2*w);
# GET VALUES OF FREE PARAMETER, a6, THAT EXTREMIZES THE
# ENERGY EXPRESSION
da6 := simplify(diff(w,a6));
solutionset := solve({da6},{a6});
# SUBSTITUTE VALUE OF a6 IN EXPRESSION FOR CAPACITANCE
C := subs(solutionset,C);
```

OBTAIN CAPACITANCE FOR THE WHOLE PROBLEM REGION

Ctotal := 8*C;

Capacitance Upper Bound: C_{upper}

An upper bound for the capacitance can be obtained by adopting a second-order polynomial approximation for Φ throughout the capacitor volume. Thus,

$$\Phi_U = a_1 + a_2x + a_3y + a_4xy + a_5x^2 + a_6y^2. \quad (2.145)$$

The boundary conditions for Φ_U are $\Phi_U = 0$ at $x = 2$, and $\Phi_U = V_C$ at $x = 1$. The first boundary condition demands that $a_6 = 0$, $a_3 = -2 a_4$, and $a_1 = -2 a_2 - 4 a_5$. The second boundary condition further demands that $a_4 = 0$, and $a_2 = -V_C - 3 a_5$. Hence,

$$\Phi_U = 2V_C + 2a_5 - (V_C + 3a_5) x + a_5 x^2. \quad (2.146)$$

Then

$$\mathbf{E}_U = -\nabla\Phi_U = (V_C + 3a_5 - 2a_5x) \hat{\mathbf{x}}. \quad (2.147)$$

Hence

$$\begin{aligned} W_{upper} &= 8 \frac{\epsilon}{2} \int_{V/8} \mathbf{E}_U \cdot \mathbf{E}_U dV \\ &= 4 \epsilon D \int_{x=1}^2 \int_{y=0}^x (V_C + 3 a_5 - 2 a_5 x)^2 dx dy \\ &= 2 a_5^2 - 1.3333333 a_5 V_C + 6 V_C^2. \end{aligned} \quad (2.148)$$

The extremum of W_{upper} occurs when

$$\frac{\partial W_{upper}}{\partial a_5} = 0 \Rightarrow a_5 = 0.333333333 V_C \quad (2.149)$$

and is given by

$$W_{upper} = 5.777777778 \quad (2.150)$$

by assuming unity ϵ and D . Hence the upper capacitance bound is given by

$$C_{upper} = 11.55555556 F. \quad (2.151)$$

The following is a sample Maple V script file that will generate the steps given above.

```
#UPPER BOUND FOR TUBULAR CAPACITOR
#ANALYSIS NORMALIZED TO EPSILON AND DEPTH
#GUESS PHI DISTRIBUTION
phi := a1+a2*x+a3*y+a4*x*y+a5*x*x+a6*y*y;
#IMPOSE DIRICHLET CONDITIONS FOR PHI
a6 := 0;
a3 := -2*a4;
a1 := -2*a2-4*a5;
a4 := 0;
a2 := -3*a5-Vs;
#CALCULATE THE CORRESPONDING ELECTRIC FIELD
Ex := -diff(phi,x);
Ey := -diff(phi,y);
#CALCULATE THE SQUARE OF THE ELECTRIC FIELD
Esq := simplify(Ex*Ex+Ey*Ey);
#CALCULATE THE STORED SYSTEM ENERGY IN THE WHOLE GEOMETRY
int1 := 8*0.5*int(Esq,y=0..x);
energy := int(int1, x=1..2);
#MAXIMIZE THE ENERGY FUNCTIONAL, SOLVING FOR FREE COEFF.
da5 := simplify(diff(energy,a5));
solutionset := solve({da5},{a5});
#GET UPPER BOUND FOR CAPACITANCE
C := (2*energy)/Vs^2;
C := subs(solutionset,C);
```

Once again, the upper bounds can be improved by increasing the order of approximation. The conclusions drawn are similar to those drawn for the resistor problem.

2.8 Appendix C: Maple Code for T-slot Inductance Upper Bound Calculation

This Appendix provides the Maple V code employed to generate an upper inductance bound for the T-inductor of Section 2.4.3.

```
#UPPER BOUND FOR T-SLOT PROBLEM

#INITIAL GUESSES FOR H-FIELDS IN ALL ELEMENTS
#SATISFY THE CURL CONDITION
Hx1 := a11+a12*x+a13*y+2*a14*x*y+a15*x*x+a16*y*y;
Hy1 := a17+(a13+J)*x+a19*y+2*a16*x*y+a14*x*x+a18*y*y;
Hx2 := a21+a22*x+a23*y+2*a24*x*y+a25*x*x+a26*y*y;
Hy2 := a27+(a23+J)*x+a29*y+2*a26*x*y+a24*x*x+a28*y*y;
Hx3 := a31+a32*x+a33*y+2*a34*x*y+a35*x*x+a36*y*y;
Hy3 := a37+(a33+J)*x+a39*y+2*a36*x*y+a34*x*x+a38*y*y;
Hx4 := a41+a42*x+a43*y+2*a44*x*y+a45*x*x+a46*y*y;
Hy4 := a47+(a43+J)*x+a49*y+2*a46*x*y+a44*x*x+a48*y*y;
Hx5 := a51+a52*x+a53*y+2*a54*x*y+a55*x*x+a56*y*y;
Hy5 := a57+(a53+J)*x+a59*y+2*a56*x*y+a54*x*x+a58*y*y;
Hx6 := a61+a62*x+a63*y+2*a64*x*y+a65*x*x+a66*y*y;
Hy6 := a67+(a63+J)*x+a69*y+2*a66*x*y+a64*x*x+a68*y*y;

#IMPOSE BOUNDARY CONDITIONS FOR ALL ELEMENTS
a11 := 0;
a12 := 0;
a15 := 0;
```

```
a51 := 0;
a52 := 0;
a55 := 0;
a61 := 0;
a62 := 0;
a65 := 0;
a41 := 0;
a42 := 0;
a45 := 0;
a13 := -2*a16;
a14 := 0;
a44 := 0;
a43 := -2*a46;
a18 := 0;
a19 := 4*a16;
a17 := 2*J-4*a16;
a48 := 0;
a49 := -4*a46;
a47 := -2*J+4*a46;
a28 := 0;
a29 := 2*a26;
a27 := a23+J-a24;
a38 := 0;
a39 := -2*a36;
a37 := -a33-J-a34;
```

```
#IMPOSE INTERELEMENT CONTINUITY
```

```
a58 := 0;
a59 := 2*a16+2*a56;
a57 := 2*J-2*a16+a53-a54;
```

```

a68 := 0;
a69 := -2*a46-2*a66;
a67 := -2*J+2*a46-a63-a64;
a66 := -a16-a56-a46;
a64 := -4*J+2*a16-a53+a54+2*a46-a63;
a25 := 0;
a22 := 4*a54-4*a24;
a53 := -2*a56+(1/2)*a21+a23+2*a26;
a35 := 0;
a32 := -4*a34-16*J+8*a16+8*a56-2*a21-4*a23-8*a26+4*a54+8*a46-4*a63;
a31 := -4*a16-2*a33-4*a36-4*a46-4*a56+2*a63;
a36 := -a26;
a34 := -a23-2*J+a24-a33;

```

```

# SIMPLIFY EXPRESSIONS FOR H-FIELDS

```

```

Hx1 := simplify(Hx1);
Hy1 := simplify(Hy1);
Hx2 := simplify(Hx2);
Hy2 := simplify(Hy2);
Hx3 := simplify(Hx3);
Hy3 := simplify(Hy3);
Hx4 := simplify(Hx4);
Hy4 := simplify(Hy4);
Hx5 := simplify(Hx5);
Hy5 := simplify(Hy5);
Hx6 := simplify(Hx6);
Hy6 := simplify(Hy6);

```

```

#GET SQUARE OF FIELDS AND ENERGY IN EACH ELEMENT

```

```

H1s := simplify(Hx1*Hx1+Hy1*Hy1);

```



```

EE1 := int(H1s,x=-2..-1);
E1 := int(EE1,y=0..2);

H2s := simplify(Hx2*Hx2+Hy2*Hy2);
EE2 := int(H2s,x=-1..0);
E2 := int(EE2,y=2..3);

H3s := simplify(Hx3*Hx3+Hy3*Hy3);
EE3 := int(H3s,x=0..1);
E3 := int(EE3,y=2..3);

H4s := simplify(Hx4*Hx4+Hy4*Hy4);
EE4 := int(H4s,x=1..2);
E4 := int(EE4,y=0..2);

H5s := simplify(Hx5*Hx5+Hy5*Hy5);
EE5 := int(H5s,x=-1..0);
E5 := int(EE5,y=0..2);

H6s := simplify(Hx6*Hx6+Hy6*Hy6);
EE6 := int(H6s,x=0..1);
E6 := int(EE6,y=0..2);

#GET TOTAL ENERGY IN THE SYSTEM
Etotal := 0.5*mu*simplify(E1+E2+E3+E4+E5+E6);

#EXTREMIZE THE ENERGY FUNCTIONAL OVER THE FREE COEFFS.
da1 := diff(Etotal,a56);
da2 := diff(Etotal,a21);
da3 := diff(Etotal,a23);

```

```
da4 := diff(Etotal,a26);
da5 := diff(Etotal,a54);
da6 := diff(Etotal,a16);
da7 := diff(Etotal,a24);
da8 := diff(Etotal,a46);
da9 := diff(Etotal,a63);
da10 := diff(Etotal,a33);
sol := solve({da1,da2,da3,da4,da5,da6,da7,da8,da9,
da10},{a56,a21,a23,a26,a54,a16,a24,a46,a63,a33});

#GET UPPER BOUND FOR ENERGY
Etotal := subs(sol,Etotal);
```

Chapter 3

Minimum Inductance of the VRM

In this chapter, the algebraic dual-energy method (ADEM) is applied in the calculation of the minimum inductance of a variable-reluctance motor (VRM). Existing literature involves simple examples with boundaries, boundary conditions and source distributions that are easily handled by the ADEM. However, the geometry of the VRM at the unaligned position, the dominating curvatures characterizing the electromagnetic field distribution and the presence of a large number of boundary conditions arising at the steel boundaries, provide a challenging exercise in the application, behavior and effectiveness of the dual-energy method in a more realistic example than studied so far.

3.1 The Minimum Inductance Problem

One of the most important challenges in the design of a variable reluctance motor is the calculation of its minimum inductance, L_{min} . The value of L_{min} is critical for two reasons. First, it affects the estimation of the peak currents present in the motor windings and hence the size and cost of the inverter switches. Second, it affects the area of the energy conversion loop in the ψ - i plane and hence the prediction of the average torque that the motor can produce. Accurate calculation of L_{min} is therefore essential in reliable VRM drive design.

The problem topology is given in Figure 3-1. Phase A is on, and its respective

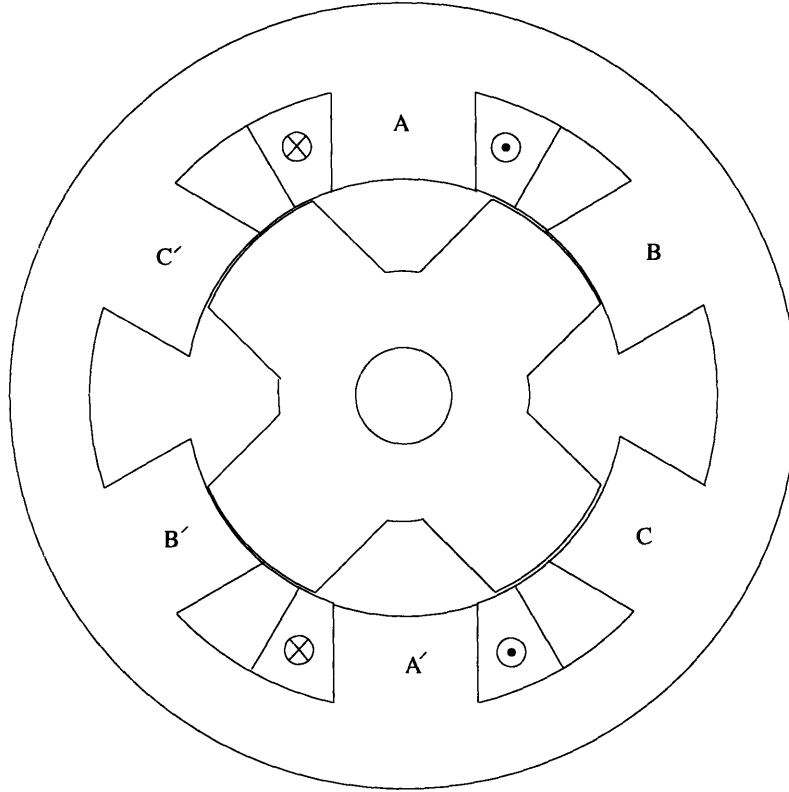


Figure 3-1: Minimum inductance topology for phase A

stator poles are symmetrically misaligned with respect to the rotor poles. At this rotor position, the air gap dominates and the calculation of the VRM minimum inductance is a linear problem. The calculation of L_{min} is achieved by solving for the magnetic field throughout the motor cross-section and hence calculating the stored magnetic energy of the system, W_m . The minimum inductance value is then obtained from the relationship

$$W_m = \frac{1}{2} L_{min} i^2. \quad (3.1)$$

Under the assumption of infinite permeability for the stator and rotor steel, one way of estimating L_{min} is to calculate the permeances of the flux paths through the air. This involves breaking the air region into probable flux paths which are of simple shape. The only rule of thumb that can be used as a guide in this discretization is that the permeance of the air path should be a maximum, i.e. for a given magnetomotive force, the flux paths should be arranged in a way that results in maximum possible flux. This method is hard to implement and may be inaccurate, since the flux does

not confine itself to any particular path that can be expressed with a simple, analytic equation.

Alternatively, numerical analysis of the electromagnetic field is often employed. The finite element method is the most widely used approach, but it involves fine discretization of the problem geometry, before a satisfactory accuracy of solution can be achieved. As was stressed in chapter 1, such an approach is not desirable in design-optimization programs, since it will slow down considerably the analysis of every candidate design considered. However, the dual-energy method can combine computational accuracy with speed. In [8], Miller has successfully applied the method of tubes and slices in the context of VRM geometries for the calculation of the minimum inductance. In this chapter, L_{min} is extracted using the algebraic-dual energy method (ADEM).

3.2 The Minimum Inductance Model

In this section the algebraic dual-energy method is applied to the VRM minimum inductance problem. This is achieved in two stages. First, the VRM geometry at the unaligned position is cast in Cartesian coordinates. This allows the application of the ADEM to be most easily illustrated. Second, the problem is properly cast to include curvature.

3.2.1 The VRM Model in x - y Coordinates

Figure 3-2 casts the VRM geometry at the unaligned position in Cartesian coordinates. The winding end turns are ignored, and two-dimensional analysis is employed. The stator and rotor steel are assumed to be infinitely permeable. Again for simplicity, the airgap is omitted, an assumption which is justified since, in a well-designed VRM, the radial airgap length is small compared to the distance l . The boundary conditions are Dirichlet at $x = 0$ and Neumann at all steel boundaries. Given a constant current density, J , through the winding, the goal here is to calculate the magnetic energy stored in the above configuration. L_{min} is then directly obtained

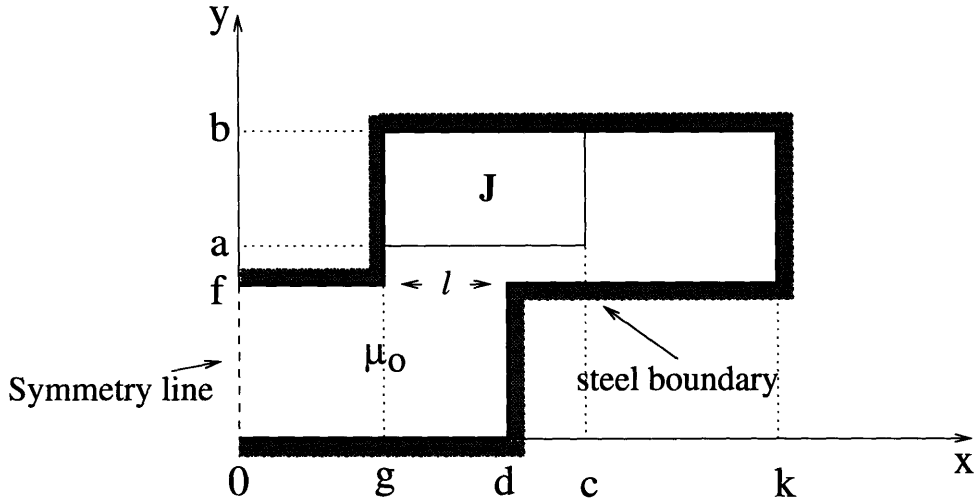


Figure 3-2: Simplified VRM model in x-y coordinates

through its linear dependence on the system energy.

Lower Energy Bound

A lower energy bound is computed using the functional

$$W_L = \int_V \mathbf{A}_L \cdot \mathbf{J} dV - \frac{1}{2} \int_V \mathbf{B}_L \cdot \mathbf{H}_L dV. \quad (3.2)$$

For the two-dimensional problem considered, the magnetic vector potential has only one component in the z direction and is approximated throughout the geometry by a polynomial in x and y . One simple approximation is

$$\mathbf{A}_L = A_z \hat{\mathbf{z}} = (a_1 + a_2 x + a_3 y) \hat{\mathbf{z}} \quad (3.3)$$

Only one region covering the inductor is sufficient for the lower bound calculation, as shown in Figure 3-3. Using (3.3), the Dirichlet condition at $x = 0$ is imposed such that

$$a_1 = a_3 = 0 \Rightarrow A_z = a_2 x \quad (3.4)$$

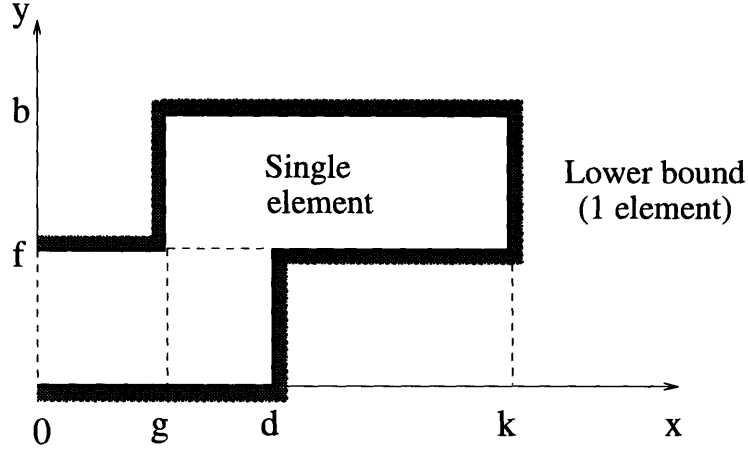


Figure 3-3: Single region representation for lower bound calculation

Then

$$\mathbf{B}_L = \frac{\partial A_z}{\partial y} \hat{x} - \frac{\partial A_z}{\partial x} \hat{y} = -a_2 \hat{y} \quad (3.5)$$

$$\mathbf{H}_L = \frac{1}{\mu} \mathbf{B}_L = -\frac{a_2}{\mu} \hat{y}. \quad (3.6)$$

Finally, substitution of (3.5) and (3.6) into (3.2) yields

$$\begin{aligned} W_L &= \int_V \mathbf{A}_L \cdot \mathbf{J} dV - \frac{1}{2} \int_V \mathbf{B}_L \cdot \mathbf{H}_L dV \\ &= -\frac{a_2^2}{2\mu} [(g-k)(f-b) + df] - \frac{1}{2} J a_2 (g^2 - c^2)(a-b). \end{aligned} \quad (3.7)$$

The free coefficient, a_2 , is determined by maximizing W_L . Thus,

$$\frac{\partial W_L}{\partial a_2} = 0 \Rightarrow a_2 = \frac{\mu J}{2} \frac{(b-a)(c^2 - g^2)}{(b-f)(k-g) + df}. \quad (3.8)$$

Substituting (3.8) into (3.7) yields

$$W_L = \frac{\mu J^2}{8} \frac{(b-a)^2 (c^2 - g^2)^2}{(b-f)(k-g) + df}. \quad (3.9)$$

Upper Energy Bound

An upper bound for the stored system energy can be obtained using the functional

$$W_U = \frac{1}{2} \int_V \mathbf{B}_U \cdot \mathbf{H}_U dV. \quad (3.10)$$

The magnetic field intensity is approximated by

$$\mathbf{H}_U = (a_1 + a_2 x + a_3 y) \hat{\mathbf{x}} + (a_4 + a_5 x + a_6 y) \hat{\mathbf{y}}. \quad (3.11)$$

It is clear that at least two elements must be employed in the calculation, since in the winding region,

$$\nabla \times \mathbf{H}_U = \mathbf{J} \quad (3.12)$$

should be imposed, while in the remaining region

$$\nabla \times \mathbf{H}_U = \mathbf{0}. \quad (3.13)$$

Thus, the two solutions

$$\mathbf{H}_U^A = (a_1 + a_2 x + a_3 y) \hat{\mathbf{x}} + (a_4 + a_3 x + a_6 y) \hat{\mathbf{y}} \quad (3.14)$$

and

$$\mathbf{H}_U^J = (a_{11} + a_{12} x + a_{13} y) \hat{\mathbf{x}} + [a_{14} + (a_{13} + J) x + a_{16} y] \hat{\mathbf{y}} \quad (3.15)$$

are employed. Next the Neumann boundary conditions should be imposed at all steel surfaces. Due to the large number of boundary conditions present, (3.14) and (3.15) do not provide enough free coefficients to match the boundary conditions. A very large order of approximation for \mathbf{H}_U could perhaps alleviate this problem, but this avenue is not pursued further. Instead, the problem is subdivided into six rectangular elements, as shown in Figure 3-4. Separate polynomial approximations in x and y

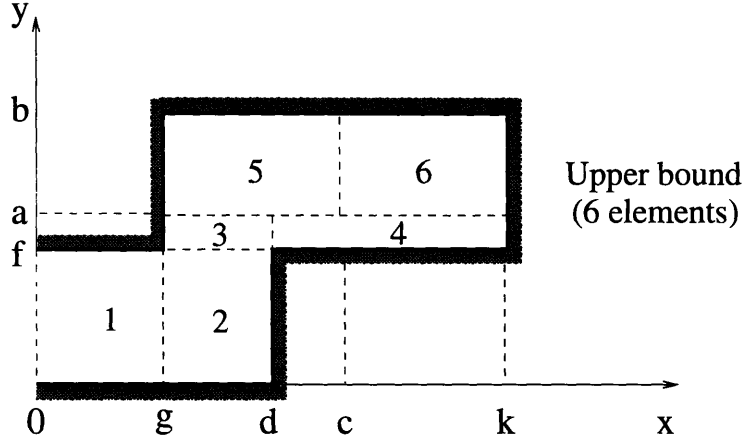


Figure 3-4: Subdivision for upper bound calculation

of the form given in (3.14) and (3.15) are considered for H_U in each element. After satisfying (3.12) or (3.13), these approximations take the form

$$\begin{aligned}
H_U^1 &= (a_1 + a_2 x + a_3 y) \hat{x} + (a_4 + a_3 x + a_5 y) \hat{y} \\
H_U^2 &= (a_6 + a_7 x + a_8 y) \hat{x} + (a_9 + a_8 x + a_{10} y) \hat{y} \\
H_U^3 &= (a_{11} + a_{12} x + a_{13} y) \hat{x} + (a_{14} + a_{13} x + a_{15} y) \hat{y} \\
H_U^4 &= (a_{16} + a_{17} x + a_{18} y) \hat{x} + (a_{19} + a_{18} x + a_{20} y) \hat{y} \\
H_U^5 &= (a_{21} + a_{22} x + a_{23} y) \hat{x} + [a_{24} + (a_{23} + J) x + a_{25} y] \hat{y} \\
H_U^6 &= (a_{26} + a_{27} x + a_{28} y) \hat{x} + (a_{29} + a_{28} x + a_{30} y) \hat{y}. \tag{3.16}
\end{aligned}$$

Imposing all Neumann boundary conditions on (3.16), and ensuring continuity of tangential H_U along element interfaces results in

$$\begin{aligned}
H_U^1 &= a_8 (g - d) \hat{y} \\
H_U^2 &= a_8 y \hat{x} + a_8 (x - d) \hat{y} \\
H_U^3 &= [a_8 f + a_{13} (y - f)] \hat{x} + [a_{13} (x - g)] \hat{y} \\
H_U^4 &= a_{13} (y - f) \frac{d - g}{d - k} \hat{x} + a_{13} (x - k) \frac{d - g}{d - k} \hat{y} \\
H_U^5 &= [a_{23} (y - b)] \hat{x} + (a_{23} + J) (x - g) \hat{y}
\end{aligned}$$

$$\mathbf{H}_U^6 = a_{13} (y - b) \frac{(a - f)(d - g)}{(a - b)(d - k)} \hat{\mathbf{x}} + a_{13} (x - k) \frac{(a - f)(d - g)}{(a - b)(d - k)} \hat{\mathbf{y}} \quad (3.17)$$

where

$$\begin{aligned} a_8 &= \frac{J(c - g)(a - b)}{(g - d)f} \\ a_{13} &= \frac{J(a - b)(d - k)(c - g)}{(a - f)(d - g)(g - k)} \\ a_{23} &= -\frac{J(c - g)}{k - g}. \end{aligned}$$

Note that no free coefficients are left after all conditions have been satisfied. Finally,

$$\begin{aligned} W_U &= \frac{1}{2} \int_V \mathbf{B}_U \cdot \mathbf{H}_U dV \\ &= \sum_{j=1}^6 \frac{\mu}{2} \int_V \mathbf{H}_U^j \cdot \mathbf{H}_U^j dV \\ &= \frac{J^2 \mu (c - g)^2 (b - a)}{3(a - f)(g - k)f(d - g)} \cdot [a^3 df + a^3 fk - 2a^3 fg - a^2 bfk + a^2 bfg \\ &\quad + a^2 d^2 k - a^2 d^2 g - 3a^2 df^2 + a^2 dkg - a^2 dg^2 - a^2 f^2 k + 4a^2 f^2 g - 2a^2 kg^2 \\ &\quad + 2a^2 g^3 - ab^2 df + ab^2 fg - abd^2 k + abd^2 g + 2abdf^2 - abdkg + abdg^2 \\ &\quad + abf^2 k - 3abf^2 g + 2abkg^2 - 2abg^3 + ad^3 f - 3ad^2 fk \\ &\quad + 2adf^3 + adfkg + 2adfk c + adfg^2 - adfc^2 \\ &\quad - 2af^3 g + 2afkg^2 - 2afkgc - 2afg^3 + afgc^2 + b^2 df^2 - b^2 f^2 g \\ &\quad - bd^3 f + 3bd^2 fk - 2bdf^3 - bdfk^2 - bdfkg - bdfg^2 + 2bf^3 g + bfk^2 g \\ &\quad - 2bfkg^2 + 2bf g^3 + df^2 k^2 - 2df^2 kc \\ &\quad + df^2 c^2 - f^2 k^2 g + 2f^2 kgc - f^2 gc^2]. \end{aligned} \quad (3.18)$$

It is interesting to note that symbolic manipulation (Maple V) was employed in the computations above, as well as in the derivation of the final analytic expressions for the bounds.

Energy Bound Average and Numerical Example

Table 3.1 provides the dimensions used for a numerical example. Substituting these

a	3.4 cm
b	6.0 cm
c	3.0 cm
d	2.4 cm
f	3.0 cm
g	1.5 cm
k	4.5 cm
J	1e6 A/m ²
μ	μ_o

Table 3.1: Geometric and excitation values for inductance problem

values into (3.9) and (3.18), yields

$$W_L = 0.029864 \text{ J/m.} \quad (3.19)$$

$$W_U = 0.340046 \text{ J/m.} \quad (3.20)$$

The average of the two energy bounds is

$$W_{avg} = \frac{W_L + W_U}{2} = 0.184955 \text{ J/m.} \quad (3.21)$$

This compares favorably with a finite element solution, obtained using QuickField [63] and 54,000 nodes. The energy computed from that analysis is

$$W_{FEA} = 0.21082 \text{ J/m.} \quad (3.22)$$

Although the individual energy bounds are not accurate, their average is within 12% of the FEA solution.

The equations for the two bounds, (3.9) and (3.18), are simple and compact. As a result, they can be easily translated into C code and incorporated in a design-optimization program. In fact, this translation can be done automatically by Maple V. An estimate of L_{min} can therefore be obtained within fractions of a second, for every design to be evaluated. The above bounds although fairly close, may still not be sufficiently accurate for motor design. The accuracy can be immediately improved

by increasing the order of polynomial approximation within the elements. Accuracy estimates and criteria for equidistance of bounds are critical issues, further explored in the next section. Moreover, the curvature present in the motor geometry has to be included and this issue is further addressed in Section 3.2.3.

3.2.2 Error Analysis

Before proceeding with the analysis of the error involved in the application of the algebraic dual-energy method, it is instructive to introduce the basic ideas and definitions typically employed in such an analysis. The following definitions have been widely applied in deriving accuracy estimates for finite-element computations [49], [50], [51] and are briefly presented here.

The discretization of a problem is defined by the shape and number of elements employed in the problem region and the degree of polynomial approximation used within the elements. Suppose the exact magnetic field distribution in the two-dimensional minimum inductance problem is $\mathbf{H}(x, y)$ and it is approximated in the upper bound calculation by $\mathbf{H}_U(x, y)$.

Then, the error \mathbf{e} is defined as

$$\mathbf{e}(x, y) = \mathbf{H}(x, y) - \mathbf{H}_U(x, y) \quad (3.23)$$

and is dependent on the exact solution $\mathbf{H}(x, y)$ and the approximation adopted. A measure of the error in energy form is given by

$$\|\mathbf{e}\|^2 = \frac{1}{2} \int_V \mathbf{e} \cdot \mathbf{e} \, dV \quad (3.24)$$

where $\|\mathbf{e}\|$ is the energy norm of \mathbf{e} .

Error estimation and control is traditionally based on extensions, that is, on consecutive changes of discretization that successively increase the number of degrees of freedom. In considering the error involved in the dual-energy method, three extensions are available: an extension based on mesh refinement only (h-extension), which

involves an increase in the number of elements; an extension based on increasing the polynomial degree of a given set of elements (p-extension); and a combination of the two (hp-extension). The h- and hp-extensions are not considered further in this thesis. The only mesh refinement that will be considered here is the one which will be sufficient to satisfy the boundary conditions for either bound. As a result, programming can be made particularly simple. Moreover, as shown later, several singularities are present in the geometry under consideration. In the presence of such singularities, the rate of convergence of the p-extension has been shown to be exactly twice the rate of convergence of the h-extension [49].

By employing the p-extension to the dual-energy method, the goal is to derive an algorithm that will provide equidistant bounds, and will allow conclusions to be drawn on the overall quality of the method. These conclusions will depend on the criteria one chooses in assessing the performance of the p-extension. One way to assess this performance is to consider the relationship between the error in energy and the number of degrees of freedom, or free coefficients, N . This is the most logical measure to use since it looks at the system as a whole by providing information on the overall quality of the approximation. This is in agreement with the dual-energy method philosophy which extremizes the total stored magnetic energy of the system. Moreover, the error in the energy norm is the best understood and most widely used measure of performance in the literature on finite-element analysis. However, it should be understood that a small error-in-the-energy norm does not guarantee a small error in any other quantity of interest, for example, in the field distribution at a special point in the geometry.

p-Convergence of the Dual-Energy Method

The energy bounds of the previous section can be improved by increasing the order of the polynomial approximations for \mathbf{A}_L and \mathbf{H}_U , and hence the number of free coefficients. The analytic calculation of (3.2) and (3.10), although still possible by hand, becomes a difficult task that is prone to error. Maple V [40], a symbolic manip-

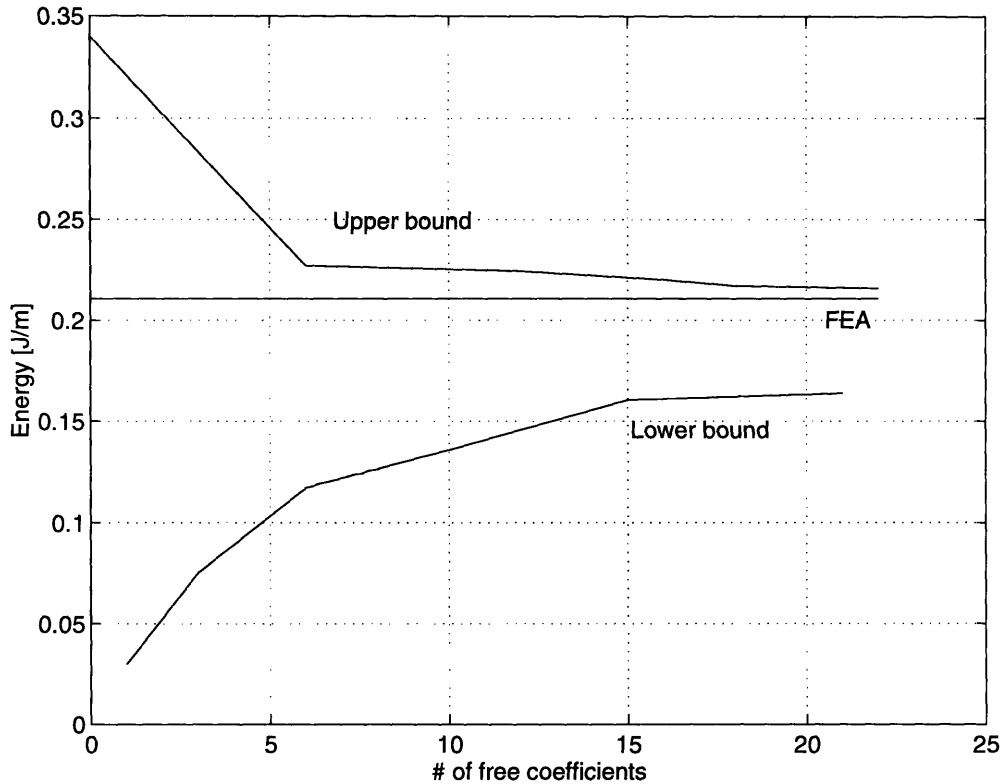


Figure 3-5: Energy bounds convergence to FEA solution

ulation package, is employed to alleviate this problem and obtain analytic bounds for increasing numbers of coefficients. Figure 3-5 illustrates the behavior of the bounds as the order of approximation increases. Here, at each step, the order is increased by including all terms of the form $x^n y^m$, where $(n + m)$ is the next integer in the progression (p-extension). Two conclusions can be drawn. First, the upper bound converges much faster than the lower bound. Second, each bound converges faster for small numbers of free coefficients. Moreover, the rates of convergence are such that, for a number of free coefficients greater than two or three, the average of the bounds will not provide a better value than the upper bound itself. Hence it is clear that, for a relatively small number of free coefficients, the success of averaging is not guaranteed unless bounds equidistance can be assured. A criterion must be developed to select the number of free coefficients required in the calculation of each bound so as to ensure equidistance from the exact solution.

In order to study equidistance, the FEA solution of (3.22) is adopted as the

exact stored energy. Plots of the log error-in-energy versus the log number-of-free-coefficients yield the characteristics of Figures 3-6 and 3-7. For large number of free coefficients N , linear characteristics are obtained with slope $-K_2$. The absolute value of K_2 defines the asymptotic rate of convergence, which, for a linear characteristic, is referred to as algebraic.

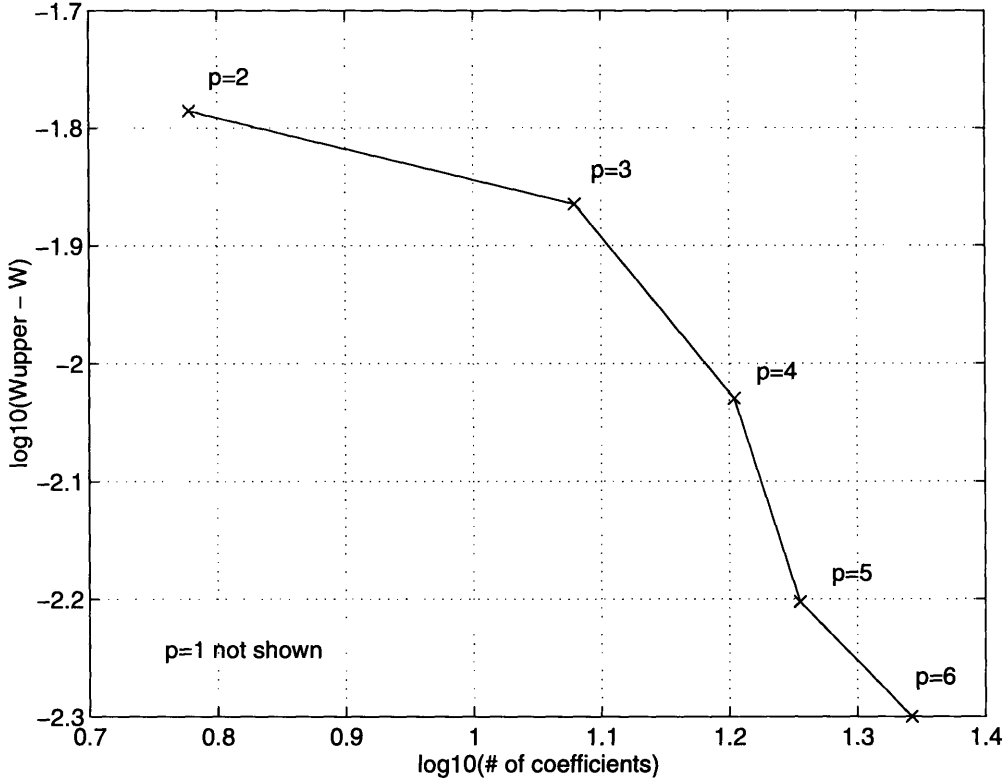


Figure 3-6: Error variation with increasing number of coefficients for upper bound. The parameter p defines the order of polynomial approximation.

The rates of convergence present in the curves of Figures 3-6 and 3-7 depend upon the smoothness of the exact solution. The exact solution can be considered as the sum of a smooth function and a series of functions of the form

$$F_i = \sum_{i=1}^m A_i r^{\lambda_i} \psi_i(\theta). \quad (3.25)$$

The F_i describe the exact solution in the neighborhood of m singular points with polar coordinates (r, θ) . The $\psi_i(\theta)$ are smooth functions and the $\lambda_i \in (\frac{1}{2}, 2)$ characterize the

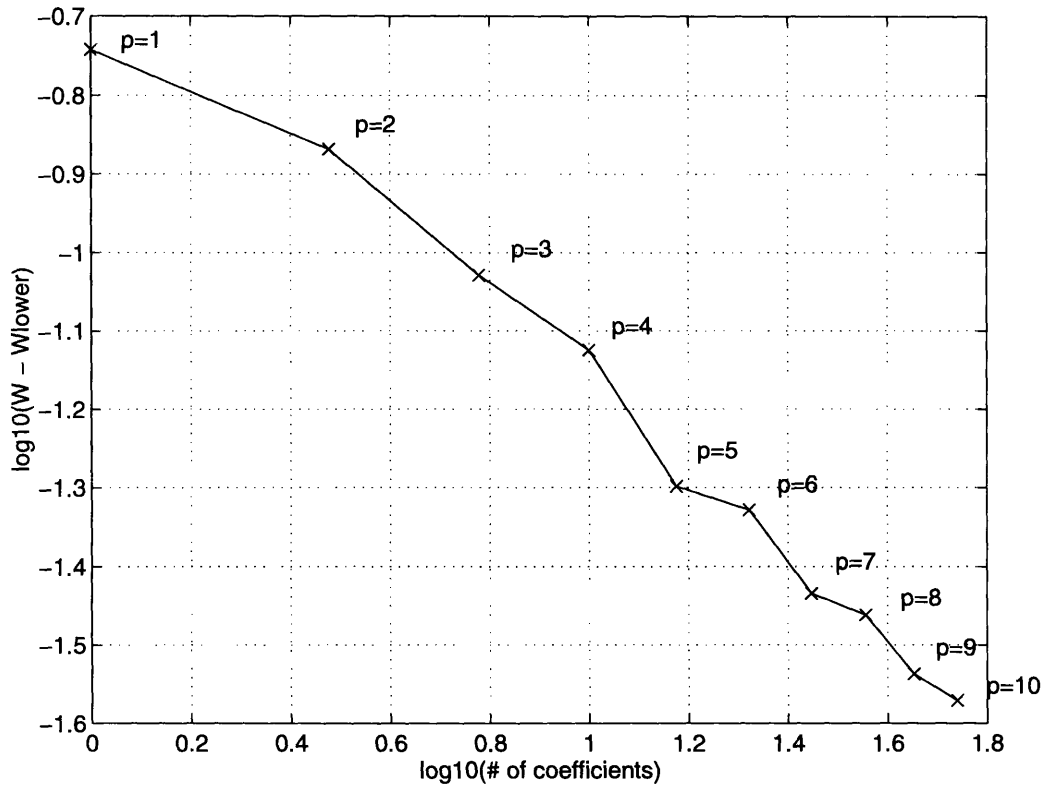


Figure 3-7: Error variation with increasing number of coefficients for lower bound. The parameter p defines the order of polynomial approximation.

singularity in the solution and hence, its smoothness. Singular points can lie in the problem region and/or its boundary and occur frequently in problems with reentrant corners, abrupt changes in material properties along boundaries, or abrupt changes in boundary conditions.

For p -extensions, if a solution is smooth, then the expected rate of convergence is faster than algebraic, resulting in a downward curving line in the $\log(\|e\|^2)$ vs. $\log(N)$ graph. If on the other hand, singularities are present, the expected rate of convergence is algebraic of the form

$$\|e\|^2 \approx K_1 \cdot N^{K_2}. \quad (3.26)$$

Here, K_2 depends on the order of polynomial approximation, p , and the point of singularity.

With the above in mind, the characteristics of Figures 3-6 and 3-7 can be further

analyzed and understood. For a fixed mesh and a uniform increase in the order of approximation, the rate of convergence (K_2) is very fast at first. This is because the error is coming from that part of the problem region where the solution is smooth. As p is increased, the singularity (or singularities) present in the solution begin to dominate the error behavior, and the convergence rate becomes that of (3.26). This linear behavior is evident in Figures 3-6 and 3-7 and is due to the two reentrant corners ($\geq 180^\circ$) present in the VRM geometry, and more specifically at the stator and rotor pole tips.

In order to determine the rate of convergence involved in each of the bounds, one can start with

$$\|e\|^2 = K_1 \cdot N^{K_2} \quad (3.27)$$

where K_1 and K_2 are constants to be determined. Equation (3.27) can be written as

$$|W - W_{bound}| = K_1 \cdot N^{K_2}. \quad (3.28)$$

Equation (3.28) contains three unknowns, namely the constants K_1 and K_2 and the unknown stored energy W . Three different sets of (W_{bound}, N) obtained using three different values of p , can be substituted into this equation, yielding three equations in the three unknowns

$$|W - W_{bound,i}| = K_1 \cdot N_i^{K_2}, \quad i = 1..3 \quad (3.29)$$

or

$$\begin{aligned} |W - W_1| &= K_1 \cdot N_1^{K_2} \\ |W - W_2| &= K_1 \cdot N_2^{K_2} \\ |W - W_3| &= K_1 \cdot N_3^{K_2}. \end{aligned} \quad (3.30)$$

This set of equations takes the form

$$\frac{\log \frac{|W-W_1|}{|W-W_2|}}{\log \frac{|W-W_2|}{|W-W_3|}} = \frac{\log \frac{N_2}{N_1}}{\log \frac{N_3}{N_2}}. \quad (3.31)$$

Hence, the exact value of the stored energy, W , can be estimated. It is important to note that (3.31) is nonlinear in W . The Newton-Raphson method can be employed for its solution but this immediately raises two issues. The first is the choice of an appropriate initial guess that will guarantee convergence to the required solution. A starting point too far away from the actual solution may result in no convergence. This is not, however, a critical problem in the ADEM case, since W_{bound} will always provide a guess very close to the actual W . The second is the singularity in the Jacobian that may lead to numerical instabilities yielding erroneous results.

The above equation was solved in Matlab using its built-in Newton-Raphson function. Estimates of W were obtained using three values of W_i from the lower bound calculations and three from the upper bound calculations. These estimates were $0.2 J/m$ and $0.2202 J/m$ and they are 5% and 4.5% below and above the finite-element value of $0.21082 J/m$, respectively.

Equation (3.27) can also be employed to estimate the number of coefficients required in the lower bound calculation to match a given error in the upper bound or vice versa. Linear regression is employed to find the best line-fit for the data points. K_1 and K_2 are hence found to be

$$(K_1, K_2) = (0.2568, -0.5683) \quad (3.32)$$

for the lower bound, and

$$(K_1, K_2) = (0.9874, -1.7159) \quad (3.33)$$

for the upper bound.

For example, an upper bound error of $E = 0.026 J/m$, corresponds to approximately 55 free coefficients in the lower bound calculation. To verify this, Maple V

can be employed to calculate a lower bound with 55 free coefficients, yielding

$$W_L = 0.18395 \text{ J/m}. \quad (3.34)$$

This implies an error

$$E = W_{FEA} - W_L = 0.02687 \text{ J/m} \quad (3.35)$$

which is almost equal to the upper bound error. A number of geometries of varying dimensions and excitations have been analyzed and the linear behavior of Figures 3-6 and 3-7 has been found to hold after a few N .

Another interesting point can be made when the number of elements in the mesh increases. This has the effect of extending the nonlinear regime of the convergence path into larger N as illustrated in Figure 3-8. In conventional finite element analyses,

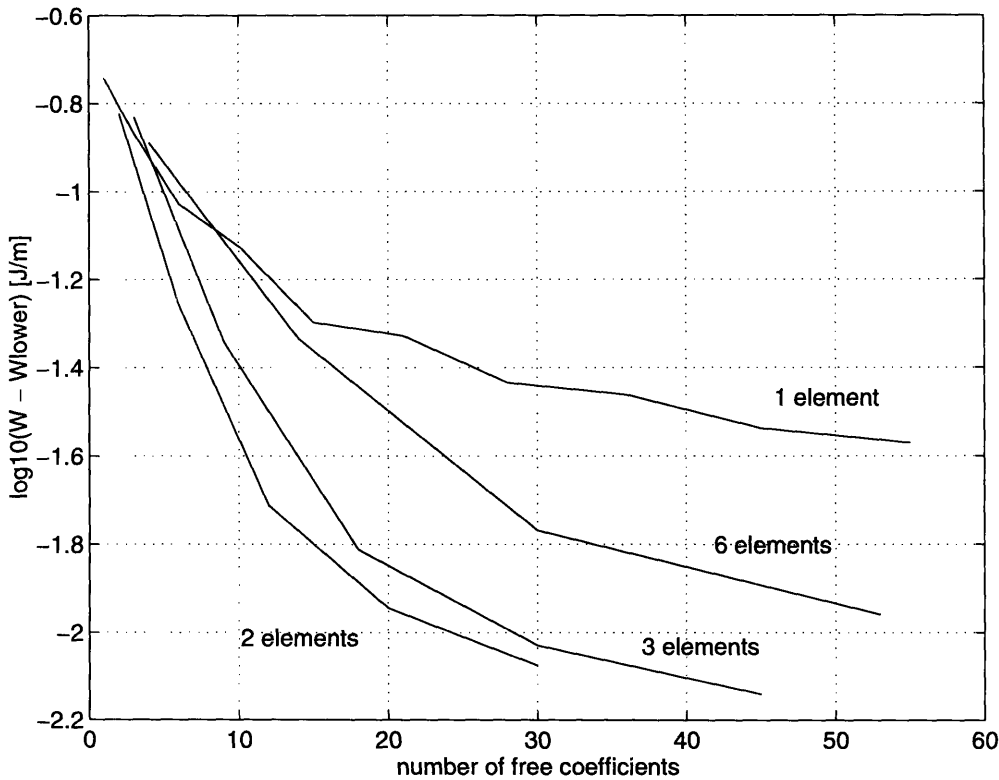


Figure 3-8: Error variation for varying number of elements in the p-extension

it is desirable to select the mesh so that the desired level of precision is reached before the rate of convergence gets into the linear regime, resulting in faster convergence.

This is, however, not desirable with the algebraic dual-energy method. It is the linear regime that allows control of the error and estimates of the number of free coefficients required to ensure equidistance for each bound. Hence it is desirable to reach that regime as fast as possible. This has the additional advantage of keeping the number of elements in the mesh low, resulting in faster and easier analytic computations within Maple. However, the compromise that must be reached in this case is that the number of elements should be high enough in order to satisfy the appropriate boundary conditions for each bound.

Finally, it should be noted that as the order of polynomial approximations increases, two issues arise. First, the computational effort involved in Maple V increases considerably. This is not a critical disadvantage since the symbolic derivation of analytic bounds at each step need only be performed once. Then the bounds expressions, which are only a function of geometry and excitation, need to be translated only once into C code for inclusion in the design-optimization program. Second, for higher orders of approximation, one may consider employing orthogonal polynomials for each bound derivation. This is because orthogonal polynomials provide improved numerical properties, that results in considerable reduction of the round-off error accumulation in numerical computations. By employing symbolic manipulation, however, the issue of round-off errors does not arise until the geometric and excitation parameters are substituted in the final expression for the bound. Within Maple V, the round-off errors can be minimized by increasing the number of decimal digits for all numerical computations.

3.2.3 The VRM Model in $r - \theta$ Coordinates

For a VRM model cast in polar coordinates, such as that of Figure 3-9, the ADEM procedure involves two complications. First, the equations of the stator and rotor pole sides cannot easily be cast in $r - \theta$ coordinates. This complicates the analytic integration over elements 2, 3, 4, 5 and 6. Second, in polar coordinates, integration is of the form $\int \dots r dr d\theta$. Multiplication by the extra r will increase the order of the integrand by one, and result in more computationally intensive integration procedures

within Maple V.

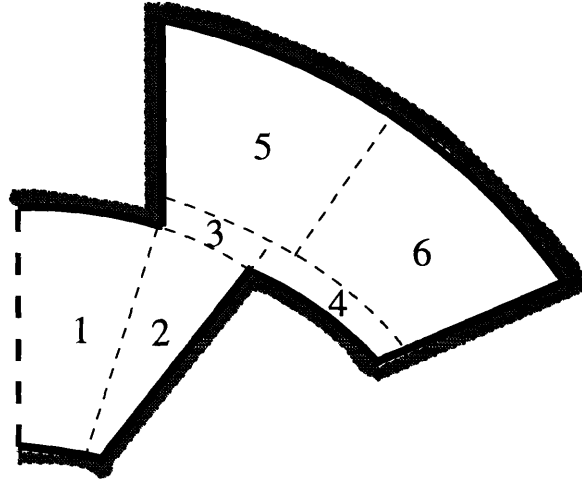


Figure 3-9: The VRM geometry in polar coordinates

A simpler yet effective way of approaching the configuration of Figure 3-9, is to perform all analysis in Cartesian coordinates by considering straight boundaries, instead of curved boundaries. The error introduced by this simplification is small, as shown below.

The VRM geometry of Figure 3-9 is defined by ten basic points, as shown in Figure 3-10. The $r - \theta$ and $x - y$ coordinates of these points are given in Table 3.2 for any motor radii and pole arc angles. In the table, θ_s and θ_r are the stator and rotor

POINT	r	θ	x	y
A	r_2	$\frac{\pi}{2}$	0	r_2
B	r'	$\frac{\pi}{2}$	0	r'
C	r'	$\frac{\pi - \theta_s}{2}$	$r' \cos(\frac{\pi - \theta_s}{2})$	$r' \sin(\frac{\pi - \theta_s}{2})$
D	r_5	$\cos^{-1}(\frac{r'}{r_5} \cos(\frac{\pi - \theta_s}{2}))$	$r' \cos(\frac{\pi - \theta_s}{2})$	$r_5 \sin(\cos^{-1}(\frac{r'}{r_5} \cos(\frac{\pi - \theta_s}{2})))$
F	r_5	$2\theta_D - \frac{\pi}{n_s}$	$r_5 \cos(\frac{\pi}{2} - \frac{\pi}{n_s})$	$r_5 \sin(\frac{\pi}{2} - \frac{\pi}{n_s})$
G	r_5	$3\theta_D - \frac{2\pi}{n_s}$	$r_5 \cos(\pi - \theta_D - \frac{2\pi}{n_s})$	$r_5 \sin(\pi - \theta_D - \frac{2\pi}{n_s})$
H	r'	$\frac{\pi + \theta_s}{2} - \frac{2\pi}{n_s}$	$r' \cos(\frac{\pi + \theta_s}{2} - \frac{2\pi}{n_s})$	$r' \sin(\frac{\pi + \theta_s}{2} - \frac{2\pi}{n_s})$
Q	r'	$\frac{\pi}{2} - \frac{\pi}{n_s}$	$r' \cos(\frac{\pi}{2} - \frac{\pi}{n_s})$	$r' \sin(\frac{\pi}{2} - \frac{\pi}{n_s})$
P	r'	$\frac{n_r \theta_r - \pi}{2}$	$r' \cos(\theta_P)$	$r' \sin(\theta_P)$
S	r_2	$\frac{\pi}{2} - \frac{\pi}{n_r} + \frac{\theta_M}{2}$	$r_2 \cos(\theta_M)$	$r_2 \sin(\theta_M)$

Table 3.2: Coordinates of the basic VRM geometry points

pole angles [rad], respectively. n_s and n_r are the number of stator and rotor poles,

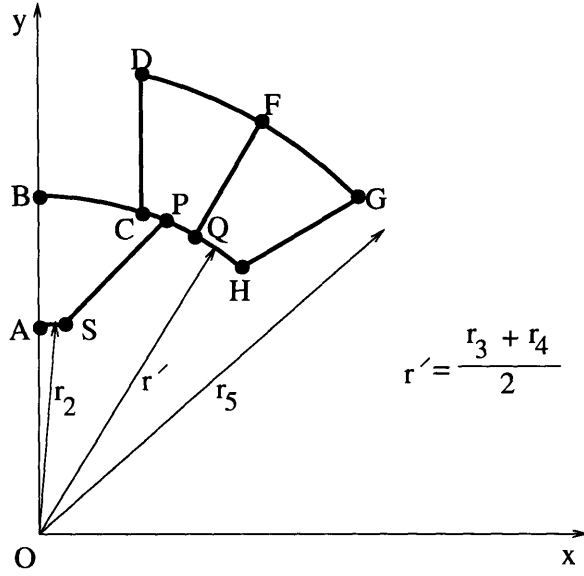


Figure 3-10: Minimum inductance model definition

respectively. r_2 is the outer rotor backiron radius, r_3 is the rotor pole radius, r_4 is the stator pole radius, r_5 is the inner stator backiron radius. The remaining parameters are defined as: $r' = \frac{r_3+r_4}{2}$, $\theta_D = \frac{\pi}{2} - \sin^{-1}\left(\frac{r'}{r_5} \cdot \sin\left(\frac{\theta_s}{2}\right)\right)$, $\theta_M = \frac{\pi}{2} - \frac{\pi}{n_r} + \sin^{-1}\left(\frac{r'}{r_2} \sin\left(\frac{\theta_r}{2}\right)\right)$, and $\theta_P = \frac{\pi}{2} - \frac{\pi}{n_r} + \frac{\theta_r}{2}$.

Analytic integration along the stator and rotor pole sides is very hard. For simplicity the rotor and stator curvatures are ignored and the basic points defining the geometry are assumed to be joined by straight lines, as illustrated in Figure 3-11. Using the values of Table 3.3, Quickfield was employed to obtain finite element solutions for a characteristic geometry. The finite-element program was run for a model with curved boundaries and a model with straight boundaries. Figures 3-12 and 3-13 provide the field profiles for each case, respectively. Although the profiles look the same, the respective stored magnetic energies are

$$W_{FEA, \text{ curved boundary}} = 0.5033 \text{ J/m} \quad (3.36)$$

$$W_{FEA, \text{ linear boundary}} = 0.4684 \text{ J/m} \quad (3.37)$$

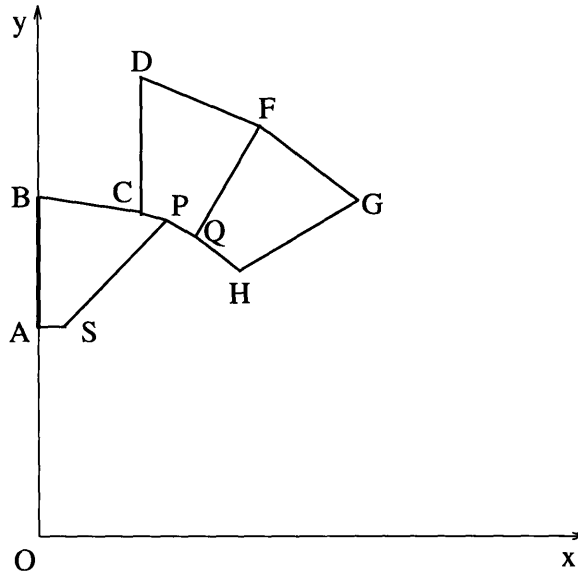


Figure 3-11: Minimum inductance model definition

r_1	15.00mm
r_2	35.00mm
r_3	55.00mm
r_4	55.52mm
r_5	85.00mm
r_6	102.00mm
n_r	4
n_s	6
θ_r	35°
θ_s	30°
J	$1e6 A/m^2$
μ	μ_0

Table 3.3: Geometric and excitation values for VRM geometry

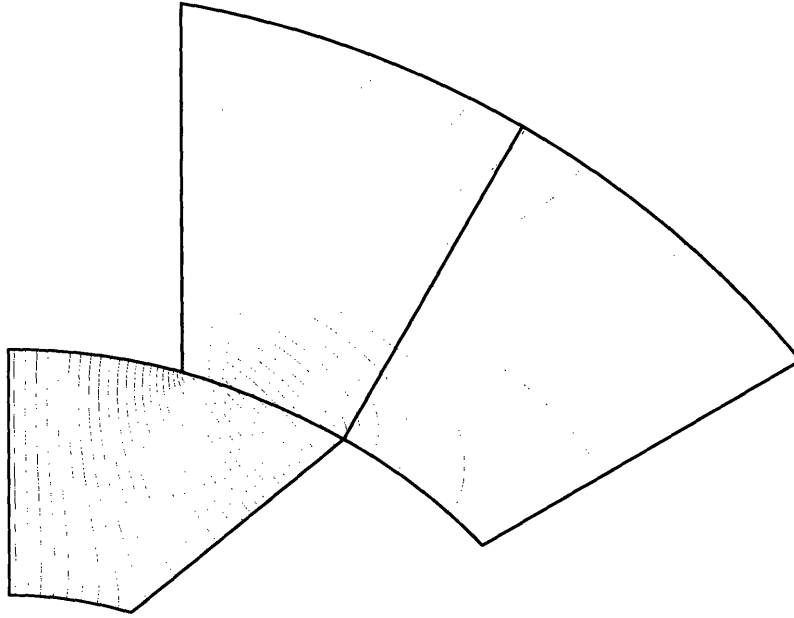


Figure 3-12: Field distribution for VRM model with curved boundaries

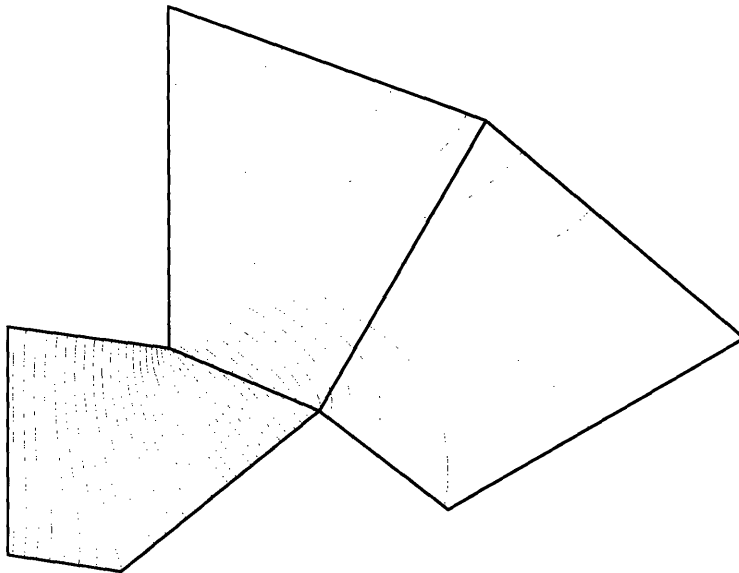


Figure 3-13: Field distribution for VRM model with straight boundaries

with approximately 42,000 nodes used in both solutions. Hence, the simplification from curved to straight boundaries results in a value which is approximately 7% less than the solution with curved boundaries. Consequently, each L_{min} estimate obtained with the model of Figure 3-11 should be adjusted by approximately 7% to account for this discrepancy.

Lower Bound Calculation for L_{min}

A first order magnetic vector potential guess, \mathbf{A}_L , is adopted. Only one region covering the inductor is sufficient for the lower bound calculation. This means that throughout the geometry considered

$$\mathbf{A}_L = A_z \hat{\mathbf{z}} = (a_1 + a_2 x + a_3 y) \hat{\mathbf{z}}. \quad (3.38)$$

The Dirichlet boundary condition at $x = 0$ is enforced so that $a_1 = a_3 = 0$. Thus,

$$A_z = a_2 x. \quad (3.39)$$

The corresponding magnetic field density is given by

$$\mathbf{B}_L = \nabla \times \mathbf{A}_L = \left(\frac{\partial A_z}{\partial y}, -\frac{\partial A_z}{\partial x} \right) = (0, -a_2) \quad (3.40)$$

and

$$\mathbf{H}_L = \frac{1}{\mu} \mathbf{B}_L = \left(0, -\frac{a_2}{\mu_0} \right). \quad (3.41)$$

Hence a lower bound for the magnetic stored energy can be calculated, using

$$W_{lower} = \int_V \mathbf{A}_L \cdot \mathbf{J} dV - \frac{1}{2} \int_V \mathbf{B}_L \cdot \mathbf{H}_L dV. \quad (3.42)$$

Assuming unit length into the paper, this becomes

$$W_{lower} = \int_{x,y} a_2 x \cdot J dx dy - \frac{1}{2\mu_0} \int_{x,y} a_2^2 \cdot dx dy. \quad (3.43)$$

This functional involves analytic integration over quadrilateral elements. This integration is not straightforward but is still feasible within Maple V; the general approach and Maple algorithm are given in Appendix A at the end of this chapter.

Upper Bound Calculation for L_{min}

The magnetic field intensity is approximated by

$$\mathbf{H}_U^A = (a_1 + a_2 x + a_3 y) \hat{\mathbf{x}} + (a_4 + a_5 x + a_6 y) \hat{\mathbf{y}} \quad (3.44)$$

in the air region and

$$\mathbf{H}_U^J = (a_{11} + a_{12} x + a_{13} y) \hat{\mathbf{x}} + [a_{14} + (a_{13} + J) x + a_{16} y] \hat{\mathbf{y}} \quad (3.45)$$

in the winding region. Due to the large number of boundary conditions present, the approximating \mathbf{H}_U do not provide enough free coefficients. The problem region is subdivided into five four-sided elements, as shown in Figure 3-14. . First-order

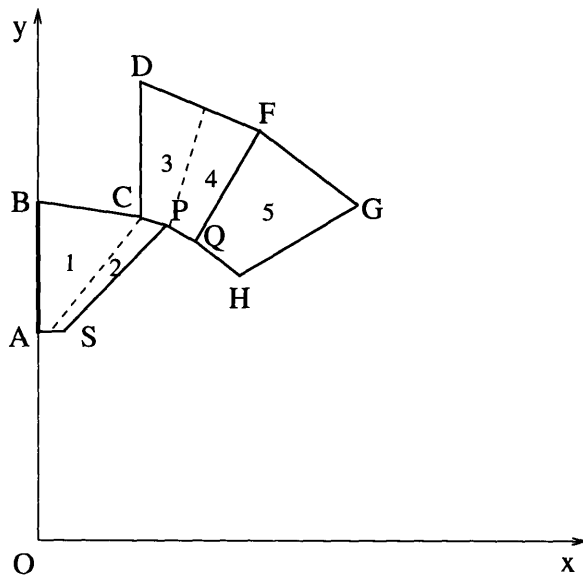


Figure 3-14: Element subdivision of the VRM model

approximations are considered for all \mathbf{H}_U 's in the elements. After satisfying the curl

condition, these take the form

$$\begin{aligned}
\mathbf{H}_U^1 &= (a_1 + a_2 x + a_3 y) \hat{\mathbf{x}} + (a_4 + a_3 x + a_5 y) \hat{\mathbf{y}} \\
\mathbf{H}_U^2 &= (a_6 + a_7 x + a_8 y) \hat{\mathbf{x}} + (a_9 + a_8 x + a_{10} y) \hat{\mathbf{y}} \\
\mathbf{H}_U^3 &= (a_{11} + a_{12} x + a_{13} y) \hat{\mathbf{x}} + (a_{14} + a_{13} x + a_{15} y) \hat{\mathbf{y}} \\
\mathbf{H}_U^4 &= (a_{16} + a_{17} x + a_{18} y) \hat{\mathbf{x}} + (a_{19} + a_{18} x + a_{20} y) \hat{\mathbf{y}} \\
\mathbf{H}_U^5 &= (a_{21} + a_{22} x + a_{23} y) \hat{\mathbf{x}} + [a_{24} + (a_{23} + J) x + a_{25} y] \hat{\mathbf{y}}. \quad (3.46)
\end{aligned}$$

For the calculation of the upper bound, the tangential components of \mathbf{H}_U must be continuous on the element interfaces. Consider the interface between elements i and j in Figure 3-15, and let the equation of the interface be $y = \lambda_1 x + \lambda_2$. Suppose the

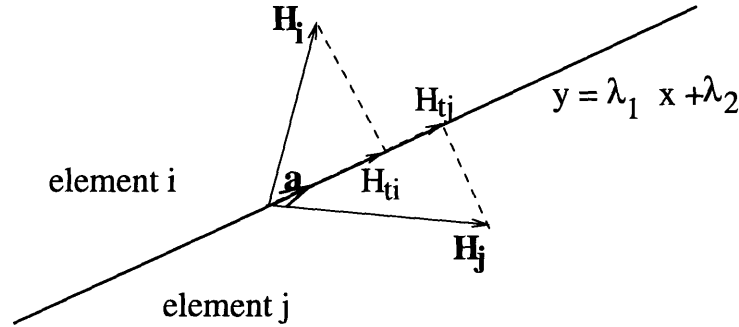


Figure 3-15: Field continuity along element interface

vector \mathbf{a} spans the interface line, then the projection of the magnetic vector \mathbf{H}_i onto the interface is given by

$$\mathbf{H}_{ti} = \frac{\mathbf{a}^T \mathbf{H}_i}{\mathbf{a}^T \mathbf{a}} \mathbf{a}. \quad (3.47)$$

With $\mathbf{a} = x \hat{\mathbf{x}} + (\lambda_1 x + \lambda_2) \hat{\mathbf{y}}$ and $\mathbf{H}_i = H_{ix} \hat{\mathbf{x}} + H_{iy} \hat{\mathbf{y}}$, equation (3.47) becomes

$$\mathbf{H}_{ti} = \frac{x H_{ix} + (\lambda_1 x + \lambda_2) H_{iy}}{x^2 + (\lambda_1 x + \lambda_2)^2} [x \hat{\mathbf{x}} + (\lambda_1 x + \lambda_2) \hat{\mathbf{y}}]. \quad (3.48)$$

Similarly, for \mathbf{H}_j ,

$$\mathbf{H}_{tj} = \frac{x H_{jx} + (\lambda_1 x + \lambda_2) H_{jy}}{x^2 + (\lambda_1 x + \lambda_2)^2} [x \hat{\mathbf{x}} + (\lambda_1 x + \lambda_2) \hat{\mathbf{y}}]. \quad (3.49)$$

Setting $\mathbf{H}_{ti} = \mathbf{H}_{tj}$ for continuity results in

$$x H_{ix} + (\lambda_1 x + \lambda_2) H_{iy} = x H_{jx} + (\lambda_1 x + \lambda_2) H_{jy}. \quad (3.50)$$

For example, suppose

$$H_{ix} = a_{i1} + a_{i2} x + a_{i3} y \quad (3.51)$$

$$H_{iy} = a_{i4} + (J + a_{i3}) x + a_{i5} y \quad (3.52)$$

$$H_{jx} = a_{j1} + a_{j2} x + a_{j3} y \quad (3.53)$$

$$H_{jy} = a_{j4} + (J + a_{j3}) x + a_{j5} y. \quad (3.54)$$

At the interface, $y = \lambda_1 x + \lambda_2$ so that

$$H_{ix} = a_{i1} + a_{i2} x + a_{i3} (\lambda_1 x + \lambda_2) \quad (3.55)$$

$$H_{iy} = a_{i4} + (J + a_{i3}) x + a_{i5} (\lambda_1 x + \lambda_2) \quad (3.56)$$

$$H_{jx} = a_{j1} + a_{j2} x + a_{j3} (\lambda_1 x + \lambda_2) \quad (3.57)$$

$$H_{jy} = a_{j4} + (J + a_{j3}) x + a_{j5} (\lambda_1 x + \lambda_2). \quad (3.58)$$

Substituting in (3.50), and equating powers of x , one obtains

$$a_{j2} = a_{i2} + 2 (J + a_{i3}) \lambda_1 + (a_{j5} + a_{i5}) \lambda_1^2 \quad (3.59)$$

$$a_{j1} = a_{i1} + 2 (J + a_{i3}) \lambda_2 + (a_{j4} + a_{i4}) \lambda_1 + 2 \lambda_1 \lambda_2 (a_{j5} + a_{i5}) \quad (3.60)$$

and

$$(a_{j4} + a_{i4}) + \lambda_2 (a_{j5} + a_{i5}) = 0 \quad (3.61)$$

as constraints on the free coefficients. This is assuming that a current density J is present in both elements i and j . If a current density is present only in element j , the above constraints change to

$$a_{j2} = a_{i2} + (J + 2 a_{i3}) \lambda_1 + (a_{j5} + a_{i5}) \lambda_1^2 \quad (3.62)$$

$$a_{j1} = a_{i1} + (J + 2 a_{i3}) \lambda_2 + (a_{j4} + a_{i4}) \lambda_1 + 2 \lambda_1 \lambda_2 (a_{j5} + a_{i5}) \quad (3.63)$$

and

$$(a_{j4} + a_{i4}) + \lambda_2 (a_{j5} + a_{i5}) = 0. \quad (3.64)$$

It is obvious that as the order of approximation for \mathbf{H}_U increases within each element, the complexity of generating the above constraints increases. A small script file that will generate the continuity condition within Maple V is included in Appendix B at the end of this chapter.

3.3 Conclusions

In this chapter, the algebraic dual-energy method was applied to calculate the stored magnetic energy of a simplified variable reluctance motor at the unaligned position. By simply averaging upper and lower energy bounds, accurate energy and inductance values can be computed using a small number of degrees of freedom. Analytic expressions for the bounds are easily obtained using a symbolic manipulation package, such as Maple V. These expressions, dependent only upon the dimensions of the problem and the current excitation, can be subsequently incorporated within a design-optimization program for fast inductance extraction. Equidistance of bounds is critical in the success of the method. For the simplified variable reluctance motor geometry considered, the linear relationship between the logarithms of the error and number of free coefficients can provide a criterion for bounds equidistance. Last but not least, although the upper bound converges faster to the exact solution, its calculation is hindered by the larger number of boundary conditions that must be sat-

ified. The lower bound on the other hand can be obtained with a trivial, one-element approximation to the magnetic vector potential.

3.4 Appendix A: Integration Over a Quadrilateral Element

This Appendix describes the algorithm employed in Maple V to perform the analytic integration of a function over a quadrilateral. This algorithm is required in the application of the ADEM method to the VRM geometry of Section 3.2.3.

3.4.1 The Algorithm

Consider a function $f(x, y)$ to be integrated over the quadrilateral element ABCD of Figure 3-16. The required integral is given by

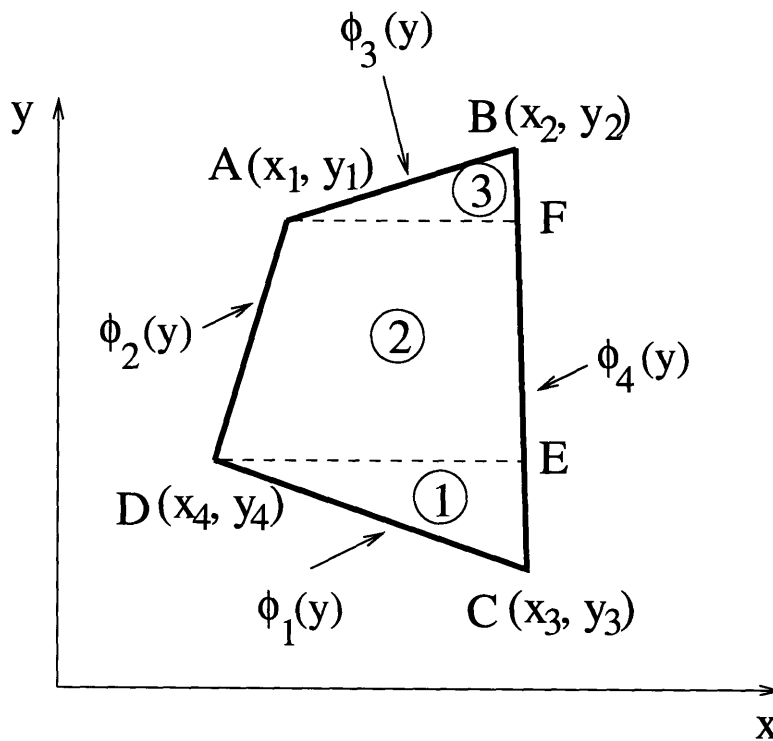


Figure 3-16: Quadrilateral element in the $x - y$ coordinate system

$$I = \int_{ABCD} f(x, y) dx dy. \quad (3.65)$$

Integration over the element is accomplished by breaking the quadrilateral into three smaller elements. Then

$$I = \int_{E1} f(x, y) dx dy + \int_{E2} f(x, y) dx dy + \int_{E3} f(x, y) dx dy. \quad (3.66)$$

This becomes

$$I = \int_{y_3}^{y_4} \int_{\phi_1(y)}^{\phi_4(y)} f(x, y) dx dy + \int_{y_4}^{y_1} \int_{\phi_2(y)}^{\phi_4(y)} f(x, y) dx dy + \int_{y_1}^{y_2} \int_{\phi_3(y)}^{\phi_4(y)} f(x, y) dx dy. \quad (3.67)$$

Notice that the lower limit of the inner integrals is the curve on which a line cutting across a triangle and moving in the positive x-direction enters the region, while the upper limit is given by the curve on which such a line leaves the region. The above integration can be carried out symbolically in Maple. The associated script file is provided and explained in the next section.

3.4.2 Maple V Algorithm

The Maple procedure *intelem* that performs symbolic integration of a function over a quadrilateral element is given below. Its inputs are the four points defining the four-sided element, as well as the function $f(x, y)$ that is to be integrated. Its output is the desired value of the integral. The steps taken within the procedure are the following.

- Given the four corner points in a random sequence, sort them with an order of increasing y-coordinate.
- Generate the equations of the edges bounding the quadrilateral, by calculating their slopes.
- Generate the additional points E and F (Figure 3-16).
- Integrate the function $f(x, y)$ over the three subelements.

- Add integration results from the three subelements to get the final value of the integral.

Procedure *intelelem*

```
with(geometry):
# Procedure int_elem. Calculates integral of a function over a four-sided
# element.
# Inputs:  pointin1...pointin4 = points defining the 4-sided element
#          finput              = function to be integrated
# Outputs: solution           = value of integral

intelelem := proc(pointin1,pointin2,pointin3,pointin4,finput)

    local point1, point2, point3, point4, point5,
          point6, S1, S2, S3, m1,m2,m3,m4, int1, int2,
          solution1, solution2, solution3, temp, yy1,
          yy2, yy3, yy4, yy5, yy6, solution, int3;

# First sort out the points so that they start from the one
# with min. y-coordinate and finish with the one with max.
# y-coordinate.

    temp := sort([pointin1[y], pointin2[y], pointin3[y], pointin4[y]]);

    if temp[1] = pointin1[y] then point1 := pointin1
      elif temp[1] = pointin2[y] then point1 := pointin2
      elif temp[1] = pointin3[y] then point1 := pointin3
      else point1 := pointin4
    fi;
```



```

if temp[2] = pointin1[y] then point2 := pointin1
  elif temp[2] = pointin2[y] then point2 := pointin2
  elif temp[2] = pointin3[y] then point2 := pointin3
  else point2 := pointin4
fi;

```

```

if temp[3] = pointin1[y] then point3 := pointin1
  elif temp[3] = pointin2[y] then point3 := pointin2
  elif temp[3] = pointin3[y] then point3 := pointin3
  else point3 := pointin4
fi;

```

```

if temp[4] = pointin1[y] then point4 := pointin1
  elif temp[4] = pointin2[y] then point4 := pointin2
  elif temp[4] = pointin3[y] then point4 := pointin3
  else point4 := pointin4
fi;

```

```

# Generate the sides bounding the polygon

```

```

line(line1, [point1, point2]);
line(line4, [point1, point3]);
line(line3, [point3, point4]);
line(line2, [point4, point2]);

```

```

# Find points 5 and 6, which define the three subelements

```

```

point(helpp1, -0.5, point2[y]);
point(helpp2, -0.5, point3[y]);
line(line5, [helpp1, point2]);
line(line6, [helpp2, point3]);
point5 := inter(line5, line4);

```

```

    point6 := inter(line6, line2);

# Integrate the input function over the lower subelement
    yy1 := solve(line4[equation],x);
    yy2 := solve(line1[equation],x);
    int1 := simplify(int(fininput, x=yy2..yy1));
    solution1 := int(int1, y=point1[y]..point2[y]);
    solution1 := simplify(solution1);

# Integrate the input function over the middle subelement
    yy3 := solve(line2[equation],x);
    yy4 := solve(line4[equation],x);
    int2 := simplify(int(fininput, x=yy3..yy4));
    solution2 := int(int2, y=point2[y]..point3[y]);
    solution2 := simplify(solution2);

# Integrate the input function over the upper subelement
    yy5 := solve(line2[equation],x);
    yy6 := solve(line3[equation],x);
    int3 := simplify(int(fininput, x=yy5..yy6));
    solution3 := int(int3, y=point3[y]..point4[y]);
    solution3 := simplify(solution3);

# Add up integrals from all subelements
    solution := solution1+solution2+solution3;

    end;

```

Using the above procedure, small script files can be written to calculate upper and lower bounds to the magnetic energy stored within a VRM model at minimum alignment. An example script file that will calculate a lower energy bound for a first order

vector potential approximation and employing the dimensions of Table 3.1 is given below.

```
# Give the basic motor dimensions, geometry and excitation
r1 := 15/1000;
r2 := 35/1000;
r3 := 55/1000;
r4 := 55.52/1000;
r5 := 85/1000;
r6 := 102/1000;
nr := 4;
ns := 6;
thetar := evalf(35*Pi/180);
thetas := evalf(30*Pi/180);
J := 1000000;
factorr := evalf(-10000000/(2*4*Pi));

# Define critical radii and angles
rav := (r3+r4)/2;
thetac := evalf((Pi-thetas)/2);
thetad := evalf(Pi/2-arcsin(rav*sin(thetas/2)/r5));
thetaf := evalf(Pi/2-Pi/ns);
thetag := 2*thetaf - thetad;
thetah := evalf(Pi/2-thetas/2+thetas-2*Pi/ns);
thetap := evalf(Pi/2-Pi/nr+thetar/2);
thetass := evalf(Pi/2-Pi/nr+arcsin(rav*sin(thetar/2)/r2));
thetat := evalf(Pi/2-Pi/(2*nr)+(arcsin(rav*sin(thetar/2)/r2))/2);

# Generate the 11 basic points, defining the geometry
point(A1,0,r2);
point(B1,0,rav);
```

```

point(C1,rav*cos(thetac),rav*sin(thetac));
point(D1,C1[x],r5*sin(thetad));
point(F1,r5*cos(thetaf),r5*sin(thetaf));
point(G1,r5*cos(thetag),r5*sin(thetag));
point(H1,rav*cos(thetah), rav*sin(thetah));
point(Q1,rav*cos(thetaf), rav*sin(thetaf));
point(P1,rav*cos(thetap), rav*sin(thetap));
point(S1,r2*cos(thetass), r2*sin(thetass));
point(T1,r2*cos(thetat), r2*sin(thetat));
midpoint(D1,F1,V1);

# Guess for first order A and get corresponding B
A := a1*x;
Bx := diff(A,y);
By := -diff(A,x);
Bsq := expand(Bx*Bx+By*By);

# Calculate the corresponding lower bound for energy
energy1 := int_elem(A1,B1,C1,T1,Bsq);
energy2 := int_elem(C1,P1,S1,T1,Bsq);
energy3 := int_elem(C1,D1,V1,P1,Bsq);
energy4 := int_elem(P1,V1,F1,Q1,Bsq);
energy5 := int_elem(Q1,F1,G1,H1,Bsq);
energy6 := int_elem(C1,D1,V1,P1,A);
energy7 := int_elem(P1,V1,F1,Q1,A);

energy := factorr*(energy1+energy2+energy3+energy4+energy5)
+J*(energy6+energy7);

# Extremize the energy bound

```

```

da1 := diff(energy,a1);
sol := solve({da1},{a1});

# Get lower energy bound
energy := subs(sol, energy);;

```

3.5 Appendix B: Generation of Inter-Element Continuity

Section 3.2.3 provides the theory for imposing continuity of tangential magnetic field intensity along an element interface. The Maple V code that will generate this condition is provided below.

```

with(geometry):
with(linalg):

# Procedure cont_cond. Calculates continuity condition for H_tangential
# at an interface defined by line l.
#
# Inputs:  point1, point2 = H-vectors whose tangential components
#          must match
#          l              = interface line
# Outputs: condition     = continuity conditions

cont_cond := proc(point1,point2,l)

    local condition, P1, P2;

# Get the projection of each of the vectors on the interface line, l

```

```
projection(point1, l, P1);  
projection(point2, l, P2);  
  
condition := array([simplify(P1[x]-P2[x]), simplify(P1[y]-P2[y])]);  
  
end;
```

Chapter 4

Thermal Analysis of the VRM

This chapter describes the application of the algebraic dual-energy method to the thermal analysis of variable reluctance machines. First the analogy between the steady-state heat conduction equations and electrostatic equations is presented. Then, based on this analogy, the existence of upper and lower thermal energy bounds is discussed. The idea of bounding is finally extended to the prediction of the hot spot within the variable reluctance motor, which is important to machine design. This addresses the problem of bounding the temperature at a point as opposed to bounding the energy of the whole system.

4.1 The Steady-State Heat Conduction Problem and its Analogy to Electrostatics

The first of several equations governing heat conduction is Fourier's law. It states that a temperature gradient causes heat to flow. The rate of this heat flow is proportional to the temperature gradient. This is mathematically expressed as

$$\mathbf{q} = -k \nabla T \quad (4.1)$$

where \mathbf{q} is the heat flux vector, k is the thermal conductivity, and T is the temperature. The negative sign in the equation indicates that heat flows from high to

low temperature. In general, k is dependent on temperature. Example values are $k_{copper} = 383W/m \cdot K$, $k_{steel} = 50W/m \cdot K$, and $k_{air} = 0.026W/m \cdot K$, at room temperature. The other important equation governing heat conduction is an energy conservation statement, expressing the balance between the energy Q generated internally to the system, and energy flow across its boundaries. This statement is

$$\nabla \cdot \mathbf{q} = Q \quad (4.2)$$

where Q is the rate of internal heat generation. Combining the above equations

$$-\nabla \cdot (k\nabla T) = Q. \quad (4.3)$$

This equation, usually referred to as the steady-state heat conduction equation, is hard to solve analytically for a wide range of multidimensional problems. Given a volume V bounded by a closed surface S , the steady-state heat conduction problem amounts to determining the temperature distribution throughout V . This distribution satisfies equation (4.3) in V , subject to prescribed boundary conditions on S . Such problems are usually solved using finite-element or finite-difference techniques. Before the analogy between the heat equations and the electrostatic Maxwell's equations is presented, it is constructive to introduce a new variable \mathbf{M} , such that

$$\mathbf{M} = -\nabla T \quad (4.4)$$

and

$$\nabla \times \mathbf{M} = \mathbf{0}. \quad (4.5)$$

\mathbf{M} is generally not found in the literature but is defined here for ease of reference.

The electrostatic Maxwell's equations are

$$\nabla \times \mathbf{E} = \mathbf{0} \Rightarrow \mathbf{E} = -\nabla\Phi \quad (4.6)$$

$$\nabla \cdot \mathbf{D} = \rho \quad (4.7)$$

$$\mathbf{D} = \epsilon \mathbf{E}. \quad (4.8)$$

Combining (4.6), (4.7) and (4.8) yields

$$-\nabla \cdot (\epsilon \nabla \Phi) = \rho \quad (4.9)$$

where Φ is the electric potential, \mathbf{E} is the electric field intensity, \mathbf{D} is the electric displacement flux density, ϵ is the permittivity, and ρ is the charge density. Table 4.1 summarizes the analogy between the heat equations and Maxwell's equations. \mathbf{M} corresponds to the electric field intensity \mathbf{E} , according to this analogy. In the absence

Problem	Potential	Material properties	Source	Flux
Heat conduction	T	k	Q	\mathbf{q}
Electrostatics	Φ	ϵ	ρ	\mathbf{D}
Steady Ohmic Conduction	Φ	σ	0	\mathbf{J}

Table 4.1: Analogy between steady-state heat conduction and electrostatics

of a source, this analogy is further exploited through the introduction of the heat resistance concept in heat transfer problems. In the one-dimensional case, the thermal resistance is defined as

$$R_{th} = \frac{\Delta T}{q}. \quad (4.10)$$

This may be looked upon as the analogue of Ohm's law in electric circuit theory, where temperature and heat flow are analogues of voltage and current respectively.

4.2 The dual-energy method extended to the thermal problem

A traditional approach to solving the thermal equations of the previous section would be the discretization of the geometry cross-section in finite elements and the calculation of the temperature distribution throughout by minimization of an appropriate functional. In the absence of a heat source, another approach would involve the introduction of thermal resistances. Knowledge of the temperature distribution would

immediately imply knowledge of the hottest point in the geometry. However, such an approach is not flexible and fast enough for design-optimization purposes. Another path is followed here, that employs the algebraic dual-energy method in the calculation of the “thermal energy” of the system. Following along the lines of this analogy, appropriate functionals may be obtained that lead to upper and lower “thermal energy” bounds and to the estimation of the highest temperature within a structure.

4.2.1 Derivation of upper and lower thermal energy bounds

The proof of this section closely follows the theoretical treatment presented in Chapter 2 for resistance and capacitance bounds. The difference here lies in the presence of the heat source Q . Consider the arbitrary geometry of Figure 4-1. It is surrounded by a closed surface S , enclosing a volume V of spatially-varying thermal conductivity k . The surface S is subdivided into surfaces S_+ , and S_\perp , so that $S = S_+ \cup S_\perp$; S_+ is the part of S kept at prescribed temperature values. S_\perp is the remaining portion of S , over which the boundary condition $\mathbf{q} \cdot d\mathbf{S} = 0$ is imposed. The “thermal energy”

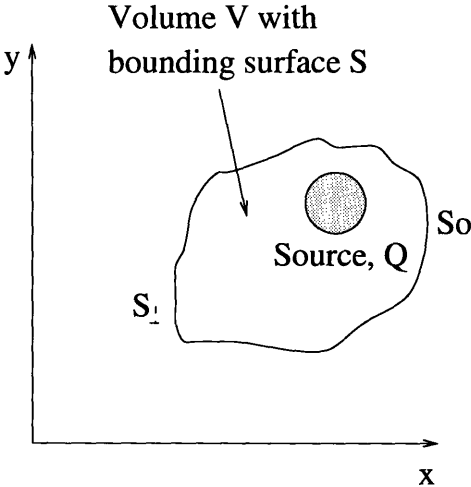


Figure 4-1: Geometry definition for “thermal energy” bounds generation

stored within the system, W_t , is obtained from

$$W_t = \frac{1}{2} \int_V \mathbf{q} \cdot \mathbf{M} \, dV = \frac{1}{2} \int_V T \, Q \, dV. \tag{4.11}$$

The second equality in (4.11) is proven as follows:

$$\begin{aligned}
W_t &= \frac{1}{2} \int_V \mathbf{M} \cdot \mathbf{q} \, dV \\
&= -\frac{1}{2} \int_V (\nabla T) \cdot \mathbf{q} \, dV \\
&= -\frac{1}{2} \int_V \nabla \cdot (T \mathbf{q}) \, dV + \frac{1}{2} \int_V T \nabla \cdot \mathbf{q} \, dV \\
&= -\frac{1}{2} \oint_S T \mathbf{q} \cdot d\mathbf{S} + \frac{1}{2} \int_V T \nabla \cdot \mathbf{q} \, dV \\
&= -\frac{1}{2} \int_{S_+} T \mathbf{q} \cdot d\mathbf{S} - \frac{1}{2} \int_{S_\perp} T \mathbf{q} \cdot d\mathbf{S} \\
&\quad + \frac{1}{2} \int_V T \nabla \cdot \mathbf{q} \, dV \\
&= \frac{1}{2} \int_V T \nabla \cdot \mathbf{q} \, dV. \tag{4.12}
\end{aligned}$$

The second equality holds because, by definition, $\mathbf{M} = -\nabla T$. The third equality makes use of the vector identity $\nabla \cdot (T \mathbf{q}) = T \nabla \cdot \mathbf{q} + (\mathbf{q} \cdot \nabla)T$. The fourth equality employs the divergence theorem. The last equality holds because $\mathbf{q} \cdot d\mathbf{S} = 0$ on S_\perp and $T = 0$ on S_+ . Hence, the two expressions in (4.11) for W_t are identical only under the particular boundary conditions defined above. It should be noted that W_t is not a physical quantity and should not be confused with the true stored system energy (heat). W_t has units of Watts $\cdot^\circ K$, as opposed to Joules or Watts for power or energy.

Analytic bounds for W_t can be obtained in a fashion similar to that for electromagnetic problems. An upper “energy” bound, W_{upper} , can be calculated by first choosing a function \mathbf{q}_U to approximate \mathbf{q} in V ; \mathbf{q}_U need only satisfy the boundary condition on S_\perp , as well as the divergence condition, $\nabla \cdot \mathbf{q}_U = Q$. The corresponding \mathbf{M}_U is computed from

$$\mathbf{M}_U = \frac{1}{k} \mathbf{q}_U. \tag{4.13}$$

\mathbf{M}_U need not be curl free and its line integral need not satisfy the boundary conditions for T on S_+ . A bound for the stored “thermal energy” is computed using the functional

$$W_{upper} = \frac{1}{2} \int_V \mathbf{q}_U \cdot \mathbf{M}_U \, dV. \tag{4.14}$$

Note that $W_{upper} = W_t$ if and only if $\mathbf{q}_U = \mathbf{q}$.

In order to prove that $W_{upper} \geq W_t$, define $\delta\mathbf{q}_U$ such that $\mathbf{q}_U = \mathbf{q} + \delta\mathbf{q}_U$. In a similar and consistent manner, define $\delta\mathbf{M}_U$ such that $\mathbf{M}_U = \mathbf{M} + \delta\mathbf{M}_U$. Then

$$\begin{aligned}
W_{upper} &= \frac{1}{2} \int_V \mathbf{M}_U \cdot \mathbf{q}_U \, dV \\
&= \frac{1}{2} \int_V (\mathbf{M} + \delta\mathbf{M}_U) \cdot (\mathbf{q} + \delta\mathbf{q}_U) \, dV \\
&= W_t + \int_V \mathbf{M} \cdot \delta\mathbf{q}_U \, dV + \frac{1}{2} \int_V k \delta\mathbf{M}_U \cdot \delta\mathbf{M}_U \, dV \\
&= W_t - \int_V \nabla T \cdot \delta\mathbf{q}_U \, dV + \frac{1}{2} \int_V k \delta\mathbf{M}_U \cdot \delta\mathbf{M}_U \, dV \\
&= W_t - \int_V \nabla \cdot (T \delta\mathbf{q}_U) \, dV + \int_V T \nabla \cdot \delta\mathbf{q}_U \, dV + \frac{1}{2} \int_V k \delta\mathbf{M}_U \cdot \delta\mathbf{M}_U \, dV \\
&= W_t - \oint_S T \delta\mathbf{q}_U \cdot d\mathbf{S} + \int_V T \nabla \cdot \delta\mathbf{q}_U \, dV + \frac{1}{2} \int_V k \delta\mathbf{M}_U \cdot \delta\mathbf{M}_U \, dV \\
&= W_t - \int_{S_+} T \delta\mathbf{q}_U \cdot d\mathbf{S} - \int_{S_\perp} T \delta\mathbf{q}_U \cdot d\mathbf{S} \\
&\quad + \int_V T \nabla \cdot \delta\mathbf{q}_U \, dV + \frac{1}{2} \int_V k \delta\mathbf{M}_U \cdot \delta\mathbf{M}_U \, dV \\
&= W_t + \frac{1}{2} \int_V k \delta\mathbf{M}_U \cdot \delta\mathbf{M}_U \, dV \\
&\geq W_t.
\end{aligned} \tag{4.15}$$

The third equality holds because, by definition, $\delta\mathbf{q}_U = k \delta\mathbf{M}_U$ and $\mathbf{q} = k \mathbf{M}$. To obtain the fourth equality, the definition $\mathbf{M} = -\nabla T$ is used. The fifth equality makes use of the vector identity $\nabla \cdot (T \delta\mathbf{q}_U) = T \nabla \cdot \delta\mathbf{q}_U + (\delta\mathbf{q}_U \cdot \nabla)T$. The sixth equality employs the divergence theorem. The last equality holds because, by construction, $\delta\mathbf{q}_U \cdot d\mathbf{S} = 0$ on S_\perp and $T = 0$ on S_+ ; moreover, by construction, $\nabla \cdot \delta\mathbf{q}_U = 0$ in the system volume.

Similarly, a lower bound for the thermal energy may be calculated by choosing a function T_L to approximate T in V . T_L satisfies the Dirichlet boundary condition on S_+ . Then, \mathbf{M}_L and \mathbf{q}_L are determined using

$$\mathbf{M}_L = -\nabla T_L \tag{4.16}$$

$$\mathbf{q}_L = k \mathbf{M}_L. \tag{4.17}$$

Note that \mathbf{q}_L will not necessarily satisfy (4.2), nor its boundary conditions. A lower bound for the stored system energy is obtained using the functional

$$W_{lower} = \int_V T_L Q dV - \frac{1}{2} \int_V \mathbf{q}_L \cdot \mathbf{M}_L dV. \quad (4.18)$$

Note that $W_{lower} = W_t$ if and only if $T_L = T$.

In order to prove that $W_{lower} \leq W_t$, define δT_L such that $T_L = T + \delta T_L$. In a similar and consistent manner, define $\delta \mathbf{M}_L$ and $\delta \mathbf{q}_L$ such that $\mathbf{M}_L = \mathbf{M} + \delta \mathbf{M}_L$ and $\mathbf{q}_L = \mathbf{q} + \delta \mathbf{q}_L$. Then,

$$\begin{aligned} W_{lower} &= \int_V T_L Q dV - \frac{1}{2} \int_V \mathbf{q}_L \cdot \mathbf{M}_L dV \\ &= \int_V (T + \delta T_L) Q dV - \frac{1}{2} \int_V (\mathbf{q} + \delta \mathbf{q}_L) \cdot (\mathbf{M} + \delta \mathbf{M}_L) dV \\ &= \int_V T Q dV - \frac{1}{2} \int_V \mathbf{M} \cdot \mathbf{q} dV + \int_V \delta T_L Q dV - \int_V \mathbf{q} \cdot \delta \mathbf{M}_L dV \\ &\quad - \frac{1}{2} \int_V k \delta \mathbf{M}_L \cdot \delta \mathbf{M}_L dV \\ &= W_t + \int_V \mathbf{q} \cdot \nabla \delta T_L dV - \frac{1}{2} \int_V k \delta \mathbf{M}_L \cdot \delta \mathbf{M}_L dV \\ &= W_t + \int_V \nabla \cdot (\delta T_L \mathbf{q}) dV - \int_V \delta T_L \nabla \cdot \mathbf{q} dV - \frac{1}{2} \int_V k \delta \mathbf{M}_L \cdot \delta \mathbf{M}_L dV \\ &= W_t + \oint_S \delta T_L \mathbf{q} \cdot d\mathbf{S} - \int_V \delta T_L \nabla \cdot \mathbf{q} dV - \frac{1}{2} \int_V k \delta \mathbf{M}_L \cdot \delta \mathbf{M}_L dV \\ &= W_t + \int_{S_+} \delta T_L \mathbf{q} \cdot d\mathbf{S} + \int_{S_\perp} \delta T_L \mathbf{q} \cdot d\mathbf{S} \\ &\quad - \int_V \delta T_L \nabla \cdot \mathbf{q} dV - \frac{1}{2} \int_V k \delta \mathbf{M}_L \cdot \delta \mathbf{M}_L dV \\ &= W_t - \frac{1}{2} \int_V k \delta \mathbf{M}_L \cdot \delta \mathbf{M}_L dV \\ &\leq W_t. \end{aligned} \quad (4.19)$$

The third equality holds because, by definition, $\delta \mathbf{q}_L = k \delta \mathbf{M}_L$ and $\mathbf{q} = k \mathbf{M}$. The fourth equality uses $\delta \mathbf{M}_L = -\nabla \delta T_L$ and $\int_V T Q dV - \frac{1}{2} \int_V \mathbf{M} \cdot \mathbf{q} dV = \frac{1}{2} \int_V T Q dV = \frac{1}{2} \int_V \mathbf{M} \cdot \mathbf{q} dV$. The fifth equality makes use of the vector identity $\nabla \cdot (\delta T_L \mathbf{q}) = \delta T_L \nabla \cdot \mathbf{q} + (\mathbf{q} \cdot \nabla) \delta T_L$. The sixth equality employs the divergence theorem. The last equality is valid because, by definition, $\mathbf{q} \cdot d\mathbf{S} = 0$ on S_\perp and $\nabla \cdot \mathbf{q} = 0$ in V ; moreover $\delta T_L = 0$ on S_+ and S_- .

4.3 The VRM Thermal Problem

The thermal analysis of the variable reluctance motor is a very complex problem. The issues considered here revolve around the calculation of the temperature distribution within the motor under steady state conditions. More specifically, given a certain heat source distribution, comprising the current losses in the stator, and a known rate of heat removal, the goal is to calculate the hottest temperature of the motor. This calculation is critical in variable reluctance motor design, since it allows the designer to account for losses in various motor parts and adopt an appropriate cooling scheme; as a result, excessive heating of the insulation and bearings may be prevented, resulting in safer and longer-lasting operation of the motor drive.

This thesis adopts a simple thermal model for the VRM and employs the algebraic dual-energy method and the idea of bounding for its solution. The goal is not the development of a sophisticated thermal model but the fast derivation of upper and lower bounds for the hot spot of the motor.

4.3.1 The VRM Thermal Model

The thermal model for the VRM geometry adopted here is given in Figure 4-2. For illustration purposes, analysis is done for a 6:4 motor cross-section, but all the results following can be easily extended to geometries with different stator:rotor pole ratios. Throughout, the following assumptions are made. First, it is assumed that no heat flows axially in the machine, which allows for two-dimensional analysis of the motor cross-section. Second, the entire machine cross-section need not be modeled if use is to be made of the existing symmetry. More specifically, only $(\frac{1}{2n_s})$ of the machine geometry need be modeled, where n_s is the number of stator poles. This assumes that excitation revolves much faster than the thermal time constant. Third, it is recognized that symmetry boundaries form adiabatic boundaries of no heat flux. Fourth, it is recognized that thermal modeling of the airgap is a hard task since one must consider laminar or turbulent air flow within the gap at various motor speeds. Here, the worst case is assumed, leading to conservative calculations; the airgap forms an adiabatic

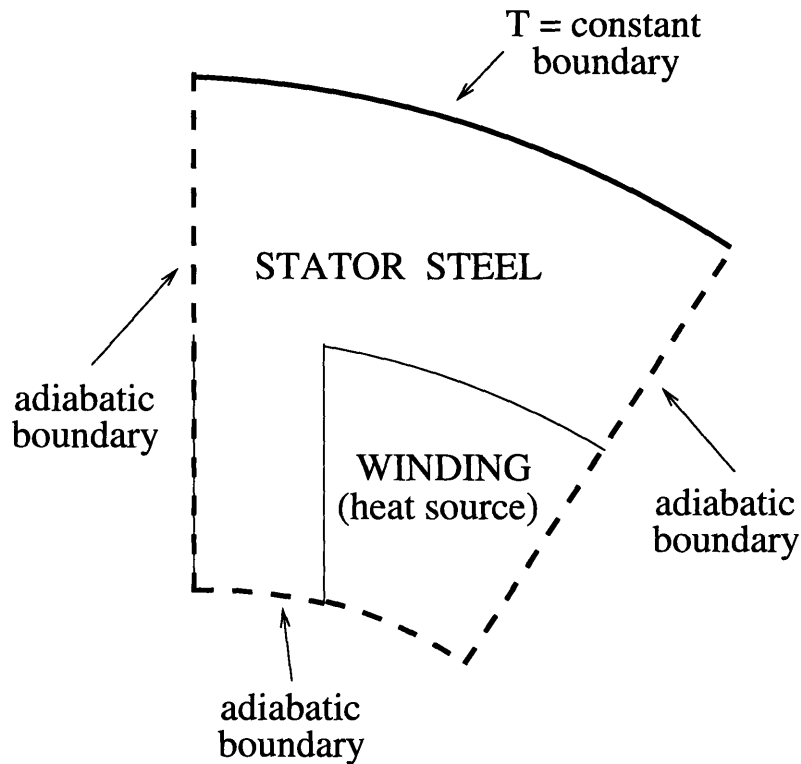


Figure 4-2: Simplified geometry of a 6:4 VRM for thermal analysis

surface, through which no heat flux flows. This assumption is also consistent with the assumption of no axial heat flux. Fifth, it is assumed that the boundary layer outside the stator may be ignored in the presence of a cooling jacket. As a result, the outer stator periphery is treated as a constant temperature surface, assumed to be zero for simplicity. Sixth, no heat is generated in the steel. Although the core losses may be high in the VRM, the temperature rise in the steel is much smaller than the temperature rise in the winding; this is because the thermal conductivity of the former is larger than the thermal conductivity of the latter. Thus, the heat loss in the steel is inconsequential. Seventh, the winding consists of a number of materials with different thermal conductivities, namely copper, wire insulation, dead air between the wire turns and often thermal epoxy, employed to attach the winding on the stator frame, increasing thermal contact. As a result, accurate thermal modeling of the winding is a very complicated task; it should accurately combine the thermal conductivities of the various materials, take into account the phase wire geometry, as well as the fact that the thermal contact between the coil and the stator steel

depends on the assumed shape of the winding. Often the winding is modeled as a single material with an effective thermal conductivity $k_{winding}$ equal to the weighted average of the thermal conductivities of the materials present. For example, for a winding consisting of air, insulation and copper,

$$k_{winding} = \frac{d_{air} + d_{Cu} + d_{insulation}}{\frac{d_{air}}{k_{air}} + \frac{d_{Cu}}{k_{Cu}} + \frac{d_{insulation}}{k_{insulation}}} \quad (4.20)$$

d is the fraction of the winding area covered by each material. Typical values for thermal conductivities at room temperature are $k_{epoxy} = 7.961 \text{ W/m} \cdot \text{K}$ (STYCAST 2651), $k_{air} = 0.028 \text{ W/m} \cdot \text{K}$ and $k_{Cu} = 383 \text{ W/m} \cdot \text{K}$ [64]. Eight, radiation is ignored. Finally, a constant current density J is assumed through the winding and defines the heat source Q for the thermal problem.

For simplicity, the geometry of Figure 4-2 is cast in Cartesian coordinates, as illustrated in Figure 4-3.

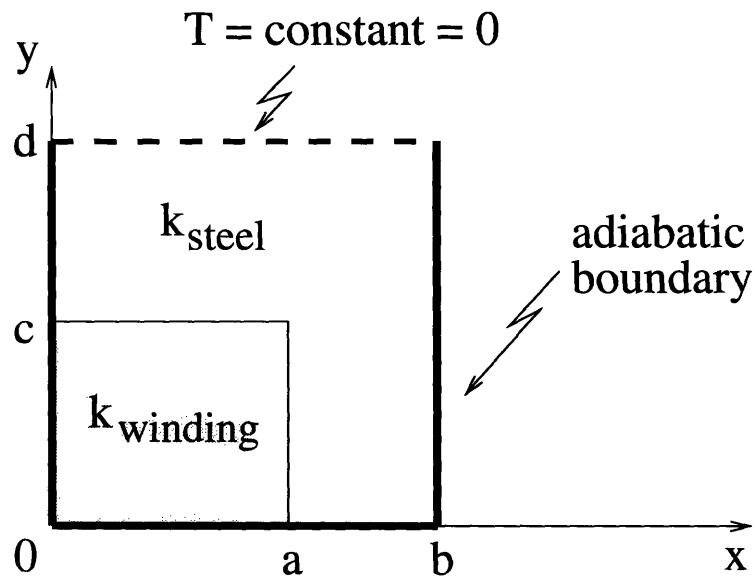


Figure 4-3: Simplified geometry of a 6:4 VRM for thermal analysis

Lower Bound Calculation

A lower bound for W_t is computed using the functional

$$W_{lower} = \int_V T_L Q \, dV - \frac{1}{2} \int_V \mathbf{q}_L \cdot \mathbf{M}_L \, dV. \quad (4.21)$$

First, the temperature is approximated throughout the geometry by a polynomial in x and y . One simple approximation is

$$T_L = a_1 + a_2 x + a_3 y. \quad (4.22)$$

Only one region covering the complete geometry is sufficient for the lower bound calculation. Using (4.22), the Dirichlet condition at $y = d$ is imposed such that

$$a_1 = -a_3 d \quad (4.23)$$

and

$$a_2 = 0. \quad (4.24)$$

Hence,

$$T_L = a_3 (y - d). \quad (4.25)$$

Next,

$$\mathbf{M}_L = -\frac{\partial T_L}{\partial x} \hat{\mathbf{x}} - \frac{\partial T_L}{\partial y} \hat{\mathbf{y}} = -a_3 \hat{\mathbf{y}} \quad (4.26)$$

and

$$\mathbf{q}_L = k \mathbf{M}_L = -k a_3 \hat{\mathbf{y}}. \quad (4.27)$$

Finally, substitution of (4.22), (4.26) and (4.27) into (4.21) yields

$$\begin{aligned} W_{lower} &= \int_V T_L Q dV - \frac{1}{2} \int_V \mathbf{q}_L \cdot \mathbf{M}_L dV \\ &= -a_3 Q b d c + a_3 Q a d c + 0.5 a_3 Q b c^2 - 0.5 a_3 Q a c^2 \\ &\quad - 0.5 k_{steel} a_3^2 a c - 0.5 k_{steel} a_3^2 b d + 0.5 k_{steel} a_3^2 b c \\ &\quad - 0.5 k_{winding} a_3^2 c b + 0.5 k_{winding} a_3^2 c a \end{aligned} \quad (4.28)$$

where $k_{winding}$ and k_{steel} are the thermal conductivities of the winding and steel, respectively. The free coefficient, a_3 , is determined by maximizing W_{lower} . Thus,

$$\frac{\partial W_{lower}}{\partial a_3} = 0 \quad (4.29)$$

which implies

$$a_3 = \frac{Qbdc - Qadc - 0.5Qbc^2 + 0.5Qac^2}{-k_{steel} ac - k_{steel} bd + k_{steel} bc - k_{winding} cb + k_{winding} ca}. \quad (4.30)$$

Substituting (4.30) into (4.28) yields

$$W_{lower} = \frac{0.125Q^2c^2 (-2.0bd + 2.0ad + bc - ac)^2}{k_{steel} ac + k_{steel} bd - k_{steel} bc + k_{winding} cb - k_{winding} ca} \quad (4.31)$$

as the desired lower bound.

Upper Bound Calculation

An upper bound for W_t can be obtained using the functional

$$W_{upper} = \frac{1}{2} \int_V \mathbf{q}_U \cdot \mathbf{M}_U dV. \quad (4.32)$$

First, the heat flux is approximated by

$$\mathbf{q}_U = (a_1 + a_2 x + a_3 y) \hat{\mathbf{x}} + (a_4 + a_5 x + a_6 y) \hat{\mathbf{y}}. \quad (4.33)$$

It is clear that at least two elements must be employed in the calculation, since in the winding region,

$$\nabla \cdot \mathbf{q}_U^W = Q \quad (4.34)$$

should be imposed, while in the stator steel

$$\nabla \cdot \mathbf{q}_U^S = 0. \quad (4.35)$$

Thus, the two approximations

$$\mathbf{q}_U^S = (a_1 + a_2 x + a_3 y) \hat{\mathbf{x}} + (a_4 + a_5 x - a_2 y) \hat{\mathbf{y}} \quad (4.36)$$

and

$$\mathbf{q}_U^W = (a_{11} + a_{12} x + a_{13} y) \hat{\mathbf{x}} + [a_{14} + a_{15} x + (Q - a_{12}) y] \hat{\mathbf{y}} \quad (4.37)$$

are employed. Next the adiabatic boundary conditions should be imposed on \mathbf{q}_U . These are that $q_x = 0$ at $x = 0$ and $x = b$, and that $q_y = 0$ at $y = 0$. Due to the large number of boundary conditions present, (4.36) and (4.37) do not provide enough free coefficients to match the boundary conditions. A very large order of approximation for \mathbf{q}_U could perhaps alleviate this problem, but this avenue is not pursued further. Instead, the problem is subdivided into four rectangular elements, as shown in Figure 4-4. Separate polynomial approximations in x and y of the form

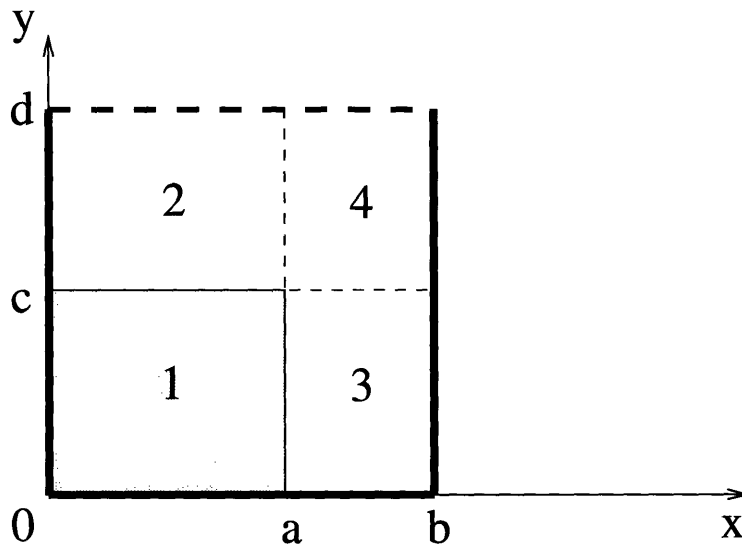


Figure 4-4: Subdivision of geometry for upper bound calculation

given in (4.36) and (4.37) are considered for \mathbf{q}_U in each element. After satisfying the divergence conditions, these approximations take the form

$$\begin{aligned}
 \mathbf{q}_U^1 &= (a_1 + a_2 x + a_3 y) \hat{\mathbf{x}} + [a_7 + a_8 x + (Q - a_2 y)] \hat{\mathbf{y}} \\
 \mathbf{q}_U^2 &= (a_{11} + a_{12} x + a_{13} y) \hat{\mathbf{x}} + (a_{17} + a_{18} x - a_{12} y) \hat{\mathbf{y}} \\
 \mathbf{q}_U^3 &= (a_{21} + a_{22} x + a_{23} y) \hat{\mathbf{x}} + (a_{27} + a_{28} x - a_{22} y) \hat{\mathbf{y}} \\
 \mathbf{q}_U^4 &= (a_{31} + a_{32} x + a_{33} y) \hat{\mathbf{x}} + (a_{37} + a_{38} x - a_{32} y) \hat{\mathbf{y}}. \quad (4.38)
 \end{aligned}$$

Imposing all adiabatic boundary conditions on (4.38), and ensuring continuity of

normal \mathbf{q}_U along element interfaces results in

$$\begin{aligned}
\mathbf{q}_U^1 &= a_2 x \hat{\mathbf{x}} + (Q - a_2) y \hat{\mathbf{y}} \\
\mathbf{q}_U^2 &= a_{12} x \hat{\mathbf{x}} + [cQ - ca_2 + a_{12}c - a_{12}y] \hat{\mathbf{y}} \\
\mathbf{q}_U^3 &= \frac{a_2 ab}{b-a} - \frac{a_2 ax}{b-a} \hat{\mathbf{x}} + \frac{a_2 ay}{b-a} \hat{\mathbf{y}} \\
\mathbf{q}_U^4 &= \frac{a_{12} a(b-x)}{b-a} \hat{\mathbf{x}} + \frac{(a_2 - a_{12})ac}{b-a} + \frac{a_{12} ay}{b-a} \hat{\mathbf{y}}.
\end{aligned} \tag{4.39}$$

Next,

$$\mathbf{M}_U = \frac{\mathbf{q}_U}{k}. \tag{4.40}$$

Finally,

$$\begin{aligned}
W_{upper} &= \frac{1}{2} \int_V \mathbf{q}_U \cdot \mathbf{M}_U dV \\
&= \frac{1}{6 k_{winding} k_{steel} (b-a)} \cdot a(-3 k_{winding} cQ a_{12} ad^2 \\
&\quad - ck_{steel} a_2^2 a^2 b + ck_{steel} a_2^2 a^3 + 2 c^3 k_{steel} Q a_2 b \\
&\quad - 2 c^3 k_{steel} Q a_2 a - c^3 k_{steel} Q^2 b + c^3 k_{steel} Q^2 a \\
&\quad - c^3 k_{steel} b a_2^2 + c^3 k_{steel} a_2^2 a + 6 k_{winding} Q a_2 ac^3 \\
&\quad - k_{winding} a_2^2 a^3 c - 3 k_{winding} Q^2 ac^3 - k_{winding} a_2^2 ac^3 \\
&\quad - 3 k_{winding} c^3 Q a_{12} a - 6 k_{winding} c^2 Q a_2 ad + 3 k_{winding} c^2 Q^2 ad \\
&\quad - 3 k_{winding} c^2 Q^2 db + 6 k_{winding} c^2 Q a_{12} ad + 6 k_{winding} c^2 Q a_2 db \\
&\quad + 3 k_{winding} Q^2 c^3 b - 3 k_{winding} a_{12}^2 c^2 db + 3 k_{winding} a_{12}^2 cd^2 b \\
&\quad + k_{winding} a_{12}^2 a^2 db + 3 k_{winding} cQ a_{12} d^2 b + 3 k_{winding} a_2^2 c^3 b \\
&\quad + k_{winding} a_{12}^2 c^3 b - 3 k_{winding} ca_2 a_{12} d^2 b + 6 k_{winding} c^2 a_2 a_{12} db \\
&\quad - k_{winding} a_{12}^2 a^2 cb - k_{winding} a_2^2 acb^2 + 2 k_{winding} a_2^2 a^2 cb \\
&\quad - k_{winding} ada_{12}^2 b^2 + k_{winding} aca_{12}^2 b^2 - 6 k_{winding} c^2 Q a_{12} db \\
&\quad - 3 k_{winding} c^2 a_2^2 db - 6 k_{winding} Q a_2 c^3 b - 3 k_{winding} c^3 a_2 a_{12} b \\
&\quad + 3 k_{winding} c^3 Q a_{12} b - k_{winding} a_{12}^2 d^3 b).
\end{aligned} \tag{4.41}$$

The two free coefficients, a_2 and a_{12} are calculated by solving the system of equations

$$\frac{\partial W_{upper}}{\partial a_i} = 0 \quad i = 2, 12. \quad (4.42)$$

Hence

$$\begin{aligned} a_2 = & -(-3c^3 k_{winding} a + 3c^3 b k_{winding} - 4c^3 b k_{steel} + 4c^3 k_{steel} a \\ & - 9c^2 b k_{winding} d - 8c^2 k_{steel} a d + 8c^2 b k_{steel} d + 9c^2 k_{winding} a d \\ & + 8c b k_{steel} a^2 + 12c a^3 k_{winding} - 4c d^2 k_{steel} b + 4c d^2 k_{steel} a \\ & - 9c d^2 k_{winding} a - 4c a^3 k_{steel} - 24c b k_{winding} a^2 + 12c b^2 k_{winding} a \\ & + 9c k_{winding} d^2 b - 4c b^2 k_{steel} a + 24b k_{winding} d a^2 - 3b d^3 k_{winding} \\ & - 12b^2 k_{winding} d a + 3a d^3 k_{winding} - 12k_{winding} a^3 d) Q c \\ & /((12b k_{winding} a^4 - 4b k_{steel} a^2 c^2 - 8b k_{steel} a^2 c d + 4b k_{steel} a^2 d^2 \\ & - 9b c^2 k_{winding} d^2 - 4k_{steel} c^2 a d^2 - 8b k_{steel} c^3 d + 8k_{steel} c^3 a d \\ & + 4b k_{steel} c^2 d^2 + 4b^2 k_{winding} c d a + 4b k_{winding} c d a^2 \\ & - 4k_{steel} c^4 a + 8k_{steel} a^3 c d - 4k_{steel} a^3 d^2 + 3b c d^3 k_{winding} \\ & + 4b^2 k_{winding} a d^2 + 9b c^3 k_{winding} d + 4b^2 k_{steel} c^2 a \\ & - 8k_{winding} a^3 c d + 4k_{winding} c^2 a d^2 + 4k_{winding} a^3 d^2 + 4k_{winding} c^4 a \\ & - 8b^2 k_{winding} c^2 a + 8b k_{winding} c^2 a^2 + 4b^2 k_{steel} a^3 - 8k_{winding} c^3 a d \\ & - 8b k_{winding} a^2 d^2 + 4b^3 k_{winding} a^2 - 3b c^4 k_{winding} + 4k_{steel} a^5 \\ & - 12b^2 k_{winding} a^3 + 4b k_{steel} c^4 - 8b k_{steel} a^4 - 4k_{winding} a^5) \end{aligned} \quad (4.43)$$

and

$$\begin{aligned} a_{12} = & -6a c Q(-k_{steel} a^3 d - c^3 k_{winding} a + c^3 k_{steel} a + k_{winding} a^3 d \\ & - 3c b^2 k_{winding} a + 3b^2 k_{winding} d a - 2c b k_{steel} a^2 + c b^2 k_{steel} a \\ & - k_{winding} d b^3 + 3c b k_{winding} a^2 - 3b k_{winding} d a^2 + c^2 k_{winding} a d \\ & - c k_{winding} a^3 + c k_{steel} a^3 - c^3 b k_{steel} + c k_{winding} b^3 - c^2 k_{steel} a d \end{aligned}$$

$$\begin{aligned}
& -c^2 b k_{winding} d + c^3 b k_{winding} - a k_{steel} b^2 d + c^2 b k_{steel} d \\
& + 2 b k_{steel} a^2 d) / (b(-4 k_{steel} c^4 a + 4 k_{winding} c^4 a \\
& + 4 k_{winding} a^3 d^2 - 3 b c^4 k_{winding} + 4 b^3 k_{winding} a^2 - 12 b^2 k_{winding} a^3 \\
& + 12 b k_{winding} a^4 - 8 b k_{steel} a^4 + 4 b k_{steel} c^4 + 4 b^2 k_{steel} a^3 \\
& + 4 k_{steel} a^5 - 4 k_{winding} a^5 + 8 k_{steel} a^3 c d + 8 k_{steel} c^3 a d \\
& - 4 k_{steel} c^2 a d^2 - 8 k_{winding} a^3 c d - 8 k_{winding} c^3 a d \\
& + 4 k_{winding} c^2 a d^2 - 8 b k_{steel} c^3 d + 4 b^2 k_{steel} c^2 a \\
& + 4 b k_{steel} c^2 d^2 + 8 b k_{winding} c^2 a^2 + 4 b^2 k_{winding} c d a \\
& + 4 b k_{winding} c d a^2 - 8 b^2 k_{winding} c^2 a - 8 b k_{winding} a^2 d^2 \\
& + 4 b^2 k_{winding} a d^2 + 4 b k_{steel} a^2 d^2 - 9 b c^2 k_{winding} d^2 \\
& + 9 b c^3 k_{winding} d + 3 b d^3 c k_{winding} - 4 b k_{steel} a^2 c^2 \\
& - 8 b k_{steel} a^2 c d - 4 k_{steel} a^3 d^2)). \tag{4.44}
\end{aligned}$$

Substituting (4.43) and (4.44) into equation (4.41), one obtains the final expression for the upper bound for W_t as

$$W_{upper} = \frac{1}{2 k_{winding}} W_1 + \frac{1}{2 k_{steel}} (W_2 + W_3 + W_4) \tag{4.45}$$

where

$$\begin{aligned}
W_1 &= \frac{1}{3} \frac{F_2^2 c^3 Q^2 a^3}{F_1^2} + \frac{2}{3} \frac{Q^2 F_2 c^4 a}{F_1} + \frac{1}{3} Q^2 a c^3 + \frac{1}{3} \frac{F_2^2 c^5 Q^2 a}{F_1^2} \\
F_1 &= 4 b k_{steel} a^2 d^2 - 8 k_{winding} a^3 c d + 4 k_{winding} c^2 a d^2 + 4 k_{winding} a^3 d^2 \\
&+ 4 b k_{steel} c^2 d^2 + 4 k_{winding} c^4 a + 8 b k_{winding} c^2 a^2 - 8 k_{winding} c^3 a d \\
&+ 4 b^2 k_{winding} a d^2 - 8 b^2 k_{winding} c^2 a - 4 b k_{steel} a^2 c^2 - 4 k_{steel} c^4 a \\
&- 8 b k_{steel} a^2 c d - 8 b k_{winding} a^2 d^2 + 4 b k_{winding} c d a^2 \\
&+ 4 b^2 k_{winding} c d a + 8 k_{steel} c^3 a d - 4 k_{steel} c^2 a d^2 \\
&+ 8 k_{steel} a^3 c d + 3 b c d^3 k_{winding} - 4 k_{steel} a^3 d^2 + 9 b c^3 k_{winding} d \\
&- 9 b c^2 k_{winding} d^2 - 8 b k_{steel} c^3 d + 4 b^2 k_{steel} c^2 a - 4 k_{winding} a^5
\end{aligned}$$

$$\begin{aligned}
& + 4b^3 k_{winding} a^2 + 4b k_{steel} c^4 - 8b k_{steel} a^4 + 4b^2 k_{steel} a^3 \\
& + 4k_{steel} a^5 - 3b c^4 k_{winding} - 12b^2 k_{winding} a^3 + 12b k_{winding} a^4 \\
F_2 = & 4c^3 k_{steel} a - 4c^3 b k_{steel} + 3c^3 b k_{winding} - 3c^3 k_{winding} a \\
& + 9c^2 k_{winding} a d - 9c^2 b k_{winding} d - 8c^2 k_{steel} a d + 8c^2 b k_{steel} d \\
& + 12c b^2 k_{winding} a - 24c b k_{winding} a^2 - 4c a^3 k_{steel} - 4c d^2 k_{steel} b \\
& + 8c b k_{steel} a^2 - 4c b^2 k_{steel} a - 9c d^2 k_{winding} a + 9c k_{winding} d^2 b \\
& + 12c a^3 k_{winding} + 4c d^2 k_{steel} a - 12k_{winding} a^3 d - 3b d^3 k_{winding} \\
& - 12b^2 k_{winding} d a + 3a d^3 k_{winding} + 24b k_{winding} d a^2
\end{aligned}$$

$$\begin{aligned}
W_2 = & 12 \frac{a^5 c^2 Q^2 F_4^2 d}{b^2 F_3^2} + 36 \frac{a^3 c^4 Q^2 F_4^2 d}{b^2 F_3^2} - 36 \frac{a^3 c^3 Q^2 F_4^2 d^2}{b^2 F_3^2} \\
& + 6 \frac{c^2 Q^2 a^2 F_4 d^2}{b F_3} + 12 \frac{a^3 c^2 Q^2 F_4^2 d^3}{b^2 F_3^2} + 6 \frac{c^3 F_5 Q^2 a^2 F_4 d^2}{F_3^2 b} \\
& - 12 \frac{c^4 F_5 Q^2 a^2 F_4 d}{F_3^2 b} + 2 \frac{c^3 Q^2 F_5 a d}{F_3} - 12 \frac{c^3 Q^2 a^2 F_4 d}{b F_3} \\
& + c^2 Q^2 a d + \frac{c^4 F_5^2 Q^2 a d}{F_3^2} - Q^2 a c^3 - \frac{F_5^2 Q^2 c^5 a}{F_3^2} \\
& - 12 \frac{a^5 c^3 Q^2 F_4^2}{b^2 F_3^2} - 2 \frac{Q^2 F_5 c^4 a}{F_3} + 6 \frac{c^5 F_5 Q^2 a^2 F_4}{F_3^2 b} \\
& + 6 \frac{c^4 Q^2 a^2 F_4}{b F_3} - 12 \frac{a^3 c^5 Q^2 F_4^2}{b^2 F_3^2}
\end{aligned}$$

$$\begin{aligned}
F_3 = & -4k_{winding} a^5 + 4k_{steel} a^5 + 4k_{winding} a^3 d^2 + 4k_{winding} c^4 a \\
& - 8b k_{winding} a^2 d^2 + 4b k_{winding} c d a^2 - 8b^2 k_{winding} c^2 a \\
& + 4b^2 k_{winding} c d a + 8b k_{winding} c^2 a^2 - 8b k_{steel} c^3 d \\
& + 4b k_{steel} c^2 d^2 + 4b^2 k_{winding} a d^2 + 4b k_{steel} a^2 d^2 \\
& - 9b c^2 k_{winding} d^2 + 9b c^3 k_{winding} d + 3b d^3 c k_{winding} \\
& - 4b k_{steel} a^2 c^2 + 4b^2 k_{steel} c^2 a - 8b k_{steel} a^2 c d \\
& + 8k_{steel} a^3 c d - 4k_{steel} c^4 a + 4b^3 k_{winding} a^2 - 8b k_{steel} a^4 \\
& - 12b^2 k_{winding} a^3 + 4b k_{steel} c^4 - 3b c^4 k_{winding} + 4b^2 k_{steel} a^3 \\
& + 12b k_{winding} a^4 + 8k_{steel} c^3 a d - 8k_{winding} a^3 c d - 4k_{steel} c^2 a d^2
\end{aligned}$$

$$- 8 k_{winding} c^3 a d + 4 k_{winding} c^2 a d^2 - 4 k_{steel} a^3 d^2$$

$$\begin{aligned} F_4 = & c k_{steel} a^3 - 3 c b^2 k_{winding} a + c^3 k_{steel} a + 3 b^2 k_{winding} d a \\ & + k_{winding} a^3 d - 3 b k_{winding} d a^2 - c^3 b k_{steel} + c^2 k_{winding} a d \\ & - c^2 k_{steel} a d - c^2 b k_{winding} d + c^3 b k_{winding} + c k_{winding} b^3 \\ & - c k_{winding} a^3 - k_{winding} d b^3 - 2 c b k_{steel} a^2 + c b^2 k_{steel} a \\ & + c^2 b k_{steel} d + 2 b k_{steel} a^2 d - a k_{steel} b^2 d - c^3 k_{winding} a \\ & - k_{steel} a^3 d + 3 c b k_{winding} a^2 \end{aligned}$$

$$\begin{aligned} F_5 = & -3 c^3 k_{winding} a - 4 c^3 b k_{steel} + 3 c^3 b k_{winding} + 4 c^3 k_{steel} a \\ & - 8 c^2 k_{steel} a d - 9 c^2 b k_{winding} d + 9 c^2 k_{winding} a d + 8 c^2 b k_{steel} d \\ & + 4 c d^2 a k_{steel} + 12 c k_{winding} a^3 + 8 c b k_{steel} a^2 - 9 c d^2 k_{winding} a \\ & - 24 c b k_{winding} a^2 + 9 c k_{winding} d^2 b - 4 c d^2 k_{steel} b \\ & + 12 c b^2 k_{winding} a - 4 c b^2 k_{steel} a - 4 c k_{steel} a^3 + 24 b k_{winding} d a^2 \\ & - 3 b d^3 k_{winding} - 12 k_{winding} a^3 d + 3 a d^3 k_{winding} - 12 b^2 k_{winding} d a \end{aligned}$$

$$\begin{aligned} W_3 = & -\frac{1}{3} \left((4 a c^3 - 4 c^3 b + 8 c^2 d b - 8 c^2 a d - 4 a^3 c + 8 c a^2 b + 4 c a d^2 \right. \\ & \left. - 4 c d^2 b - 4 c a b^2)^2 k_{steel}^2 + 2(3 c^3 k_{winding} b - 3 c^3 a k_{winding} \right. \\ & \left. - 9 c^2 k_{winding} d b + 9 c^2 a k_{winding} d + 12 c a k_{winding} b^2 \right. \\ & \left. + 9 c k_{winding} d^2 b - 24 c a^2 k_{winding} b + 12 c a^3 k_{winding} \right. \\ & \left. - 9 c d^2 k_{winding} a - 12 a^3 k_{winding} d - 12 a k_{winding} d b^2 \right. \\ & \left. + 24 a^2 k_{winding} d b - 3 b d^3 k_{winding} + 3 a d^3 k_{winding} \right) (4 a c^3 - 4 c^3 b \\ & + 8 c^2 d b - 8 c^2 a d - 4 a^3 c + 8 c a^2 b + 4 c a d^2 - 4 c d^2 b \\ & - 4 c a b^2) k_{steel} + (3 c^3 k_{winding} b - 3 c^3 a k_{winding} - 9 c^2 k_{winding} d b \\ & + 9 c^2 a k_{winding} d + 12 c a k_{winding} b^2 + 9 c k_{winding} d^2 b \\ & - 24 c a^2 k_{winding} b + 12 c a^3 k_{winding} - 9 c d^2 k_{winding} a - 12 a^3 k_{winding} d \\ & - 12 a k_{winding} d b^2 + 24 a^2 k_{winding} d b - 3 b d^3 k_{winding} + 3 a d^3 k_{winding})^2 \Big) \\ & Q^2 c^3 a^2 (a^2 - 2 b a + b^2 + c^2) / \left((4 a^2 c^2 b - 4 a c^2 b^2 - 8 a^3 c d \right. \end{aligned}$$

$$\begin{aligned}
& + 8c^3 db + 8a^2 cdb - 4c^4 b - 8ac^3 d - 4ba^2 d^2 + 8ba^4 \\
& - 4b^2 a^3 + 4ac^4 + 4c^2 a d^2 + 4a^3 d^2 - 4a^5 - 4c^2 d^2 b)k_{steel} \\
& + 4k_{winding} a^5 - 8a^2 k_{winding} c^2 b + 8a k_{winding} c^2 b^2 - 4a k_{winding} c d b^2 \\
& + 8a^3 k_{winding} c d + 8a k_{winding} c^3 d - 4a^2 k_{winding} c d b \\
& - 9k_{winding} c^3 d b + 3k_{winding} c^4 b - 4k_{winding} c^2 a d^2 - 4b^2 k_{winding} a d^2 \\
& - 4k_{winding} a^3 d^2 - 3b d^3 c k_{winding} + 9b c^2 k_{winding} d^2 \\
& + 8b k_{winding} a^2 d^2 - 12b k_{winding} a^4 + 12b^2 k_{winding} a^3 - 4a k_{winding} c^4 \\
& - 4b^3 k_{winding} a^2)^2(-b+a)
\end{aligned}$$

and

$$\begin{aligned}
W_4 &= \frac{1}{3}a^2 d \left(36 \frac{c^2 Q^2 a^2 F_7^2}{F_6^2} - 72 \frac{c^2 Q^2 a^3 F_7^2}{b F_6^2} - 108 \frac{c^3 Q^2 a^2 F_7^2 d}{b^2 F_6^2} \right. \\
& + 36 \frac{c^2 Q^2 a^4 F_7^2}{b^2 F_6^2} + 3 \frac{c^4 F_8^2 Q^2}{F_6^2} + 18 \frac{c^3 F_8 Q^2 a F_7 d}{F_6^2 b} \\
& \left. + 108 \frac{c^4 Q^2 a^2 F_7^2}{b^2 F_6^2} + 36 \frac{c^2 Q^2 a^2 F_7^2 d^2}{b^2 F_6^2} - 36 \frac{c^4 F_8 Q^2 a F_7}{F_6^2 b} \right) / \\
& (b-a) - \frac{1}{3}a^2 c \left(36 \frac{c^2 Q^2 a^2 F_7^2}{F_6^2} - 72 \frac{c^2 Q^2 a^3 F_7^2}{b F_6^2} \right. \\
& + 36 \frac{c^4 Q^2 a^2 F_7^2}{b^2 F_6^2} + 3 \frac{c^4 F_8^2 Q^2}{F_6^2} - 18 \frac{c^4 F_8 Q^2 a F_7}{F_6^2 b} \\
& \left. + 36 \frac{c^2 Q^2 a^4 F_7^2}{b^2 F_6^2} \right) / (b-a) \\
F_6 &= 4k_{steel} a^5 - 4k_{winding} a^5 - 8b k_{winding} a^2 d^2 - 12b^2 k_{winding} a^3 \\
& - 8b k_{steel} a^2 c d + 4b k_{winding} c d a^2 - 8b^2 k_{winding} c^2 a \\
& + 4b^2 k_{winding} c d a - 8b k_{steel} c^3 d + 4b^2 k_{winding} a d^2 \\
& + 8b k_{winding} c^2 a^2 - 4b k_{steel} a^2 c^2 + 4b^3 k_{winding} a^2 + 4b^2 k_{steel} a^3 \\
& - 3b c^4 k_{winding} + 12b k_{winding} a^4 + 3b c d^3 k_{winding} - 9b c^2 k_{winding} d^2 \\
& + 4b k_{steel} c^4 - 8b k_{steel} a^4 + 9b c^3 k_{winding} d + 4b k_{steel} c^2 d^2 \\
& + 4b^2 k_{steel} c^2 a + 4b k_{steel} a^2 d^2 + 4k_{winding} c^2 a d^2 \\
& + 4k_{winding} c^4 a + 4k_{winding} a^3 d^2 - 4k_{steel} c^4 a + 8k_{steel} c^3 a d
\end{aligned}$$

$$- 8 k_{winding} a^3 c d - 8 k_{winding} c^3 a d - 4 k_{steel} c^2 a d^2 + 8 k_{steel} a^3 c d$$

$$- 4 k_{steel} a^3 d^2$$

$$F_7 = c^3 b k_{winding} - c k_{winding} a^3 + 3 c b k_{winding} a^2 - 3 b k_{winding} d a^2$$

$$+ c^2 k_{winding} a d + 3 b^2 k_{winding} d a - c^2 k_{steel} a d + k_{winding} a^3 d$$

$$- k_{winding} d b^3 - a k_{steel} b^2 d - 3 c b^2 k_{winding} a - c^3 k_{winding} a$$

$$- c^2 b k_{winding} d + 2 b k_{steel} a^2 d + c k_{steel} a^3 - k_{steel} a^3 d$$

$$+ c^3 k_{steel} a + c k_{winding} b^3 - c^3 b k_{steel} + c b^2 k_{steel} a$$

$$- 2 c b k_{steel} a^2 + c^2 b k_{steel} d$$

$$F_8 = 4 c^3 k_{steel} a - 4 c^3 b k_{steel} + 3 c^3 b k_{winding} - 3 c^3 k_{winding} a$$

$$- 8 c^2 k_{steel} a d - 9 c^2 b k_{winding} d + 8 c^2 b k_{steel} d + 9 c^2 k_{winding} a d$$

$$+ 8 c b k_{steel} a^2 + 4 c d^2 k_{steel} a + 12 c b^2 k_{winding} a - 4 c k_{steel} a^3$$

$$- 9 c d^2 k_{winding} a + 9 c k_{winding} d^2 b - 24 c b k_{winding} a^2$$

$$+ 12 c k_{winding} a^3 - 4 c d^2 k_{steel} b - 4 c b^2 k_{steel} a - 12 b^2 k_{winding} d a$$

$$+ 24 b k_{winding} d a^2 - 3 b d^3 k_{winding} + 3 a d^3 k_{winding} - 12 k_{winding} a^3 d.$$

Energy Bound Average and Numerical Example

Table 4.2 provides the dimensions used for a numerical example. Substituting these

a	2.5cm
b	4.0cm
c	2.5cm
d	5.5cm
Q	100000 W/m^3
$k_{winding}$	1 $W/m \cdot K$
k_{steel}	20.5 $W/m \cdot K$

Table 4.2: Geometric and excitation values for thermal model

values into (4.31) and (4.45), yields

$$W_{lower} = 107.188 \text{ W/m} \quad (4.46)$$

$$W_{upper} = 415.298 \text{ W/m}. \quad (4.47)$$

The average of the two energy bounds is

$$W_{avg} = \frac{W_{lower} + W_{upper}}{2} = 261.243 \text{ W/m}. \quad (4.48)$$

This compares favorably with a finite element solution, obtained using QuickField [63] with 40,000 nodes. The energy computed from that analysis is

$$W_{FEA} = 368.155 \text{ W/m}. \quad (4.49)$$

The average of the two bounds is 29% lower than the FEA solution.

It is interesting to note that the equations for the bounds (4.31) and (4.45) are simple and compact. Finally, the upper bound calculation is within 13% of the finite element solution and provides a better estimate of W_t than does the average of the two bounds. As a result, the issue of bounds equidistance again becomes critical.

p-Convergence of the Algebraic Dual-Energy Method

The energy bounds of the previous section can be improved by increasing the order of the polynomial approximations for \mathbf{T}_L and \mathbf{q}_U , and hence the number of free coefficients. Maple V is employed again to analyze the p-convergence of the algebraic dual-energy method applied to the VRM thermal problem. Figure 4-5 illustrates the behavior of the bounds as the order of approximation increases. The conclusions drawn are similar to those drawn for the minimum inductance calculation in Chapter 3. The upper bound converges a lot faster than the lower bound. As was concluded in the magnetic analysis, the rates of convergence are such that, for low number of free coefficients, the average of the bounds will not provide a better value than the upper bound itself. Hence it is clear, that for a relatively small number of free coefficients, success of averaging is not guaranteed unless bounds equidistance can be assured.

In order to study equidistance, the FEA solution of (4.49) is adopted as the

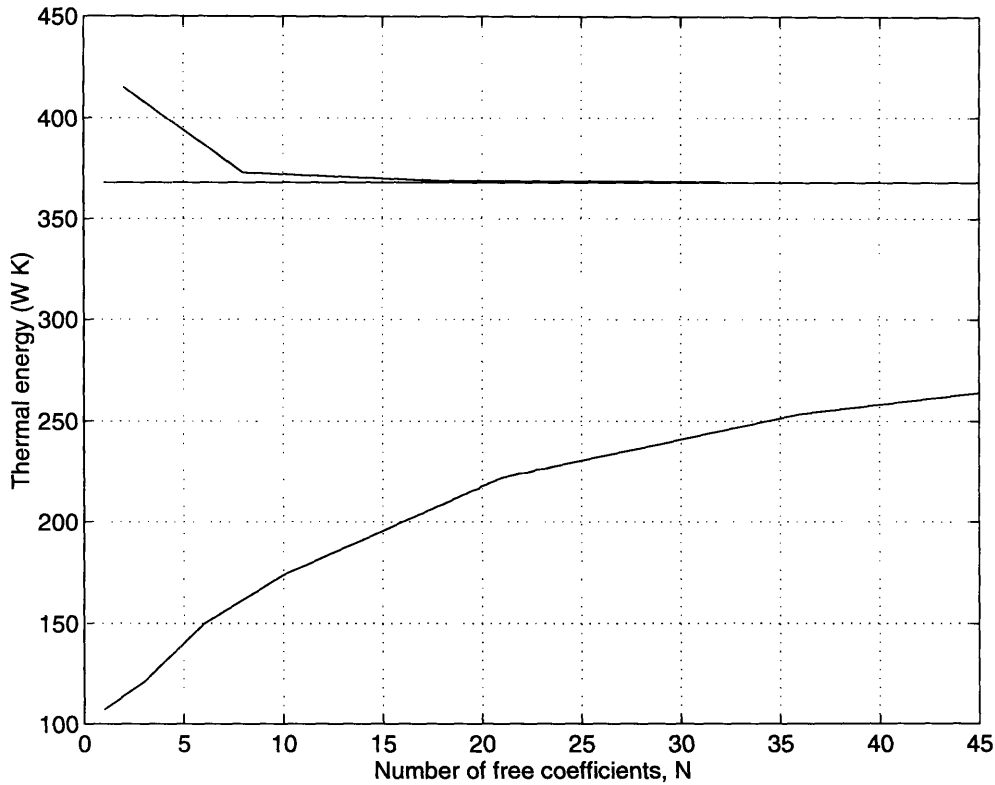


Figure 4-5: “Thermal energy” bounds convergence to FEA solution

exact stored energy. Plots of the log error-in-energy versus the log number-of-free-coefficients) yield approximately straight lines, as shown in Figures 4-6 and 4-7. This linear behavior is characteristic of p-extensions, and implies a relationship between the error in energy E and the number of coefficients N , according to

$$E = K_1 \cdot N^{K_2} \quad (4.50)$$

where K_1 and K_2 are constants to be determined. Equation (4.50) can be written as

$$|W_t - W_{bound}| = K_1 \cdot N^{K_2}. \quad (4.51)$$

Equation (4.51) contains three unknowns, namely the constants K_1 and K_2 and the unknown energy W_t . Three different sets of (W_{bound}, N) can be substituted into this

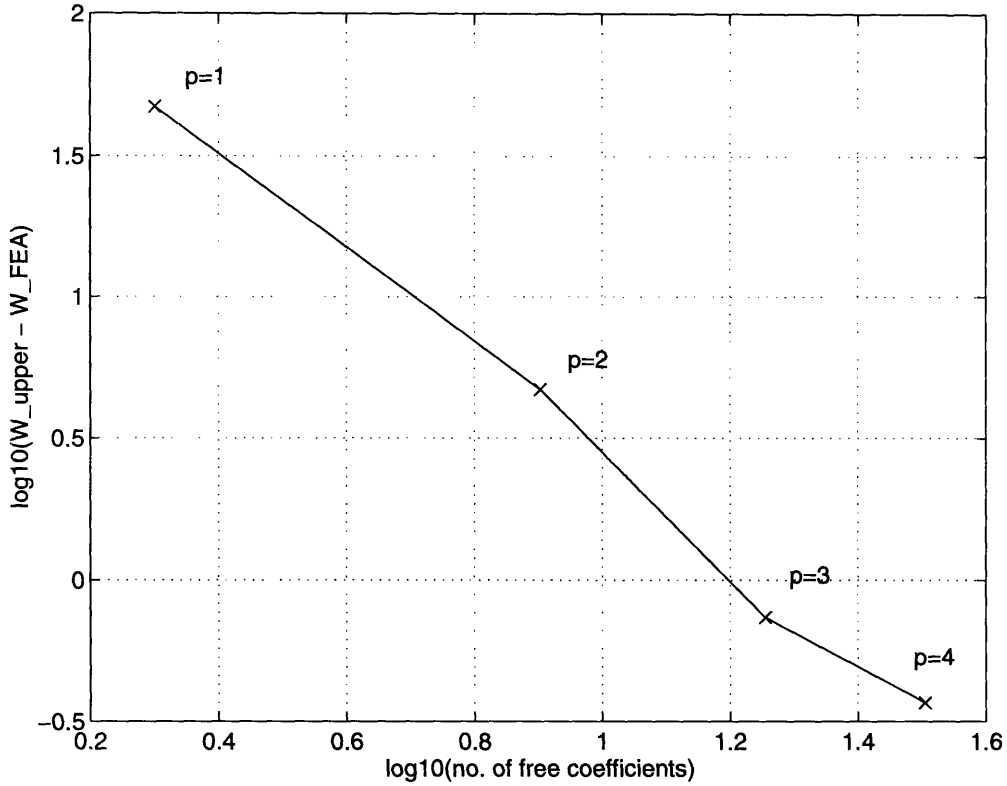


Figure 4-6: Error variation for upper “thermal energy” bound

equation, yielding three equations in the three unknowns

$$|W_t - W_{bound,i}| = K_1 \cdot N_i^{K_2} \quad i = 1..3. \quad (4.52)$$

Hence, the exact value of the stored energy can be obtained. It is important to note that this is a set of three nonlinear equations in three unknowns, and just like the magnetics case in Chapter 3, a numerical method has to be employed for their solution. For example, using the lower energy bound results with 4th, 5th and 6th orders of approximation within Matlab, yields an estimate for W_t of 368.5439 $W \cdot K$, which is 0.1% above the FEA solution.

Equation (4.50) can also be employed to estimate the number of coefficients required in the lower bound calculation, to match a given error in the upper bound or vice versa. Linear regression is employed to find the best line fit for the data points.

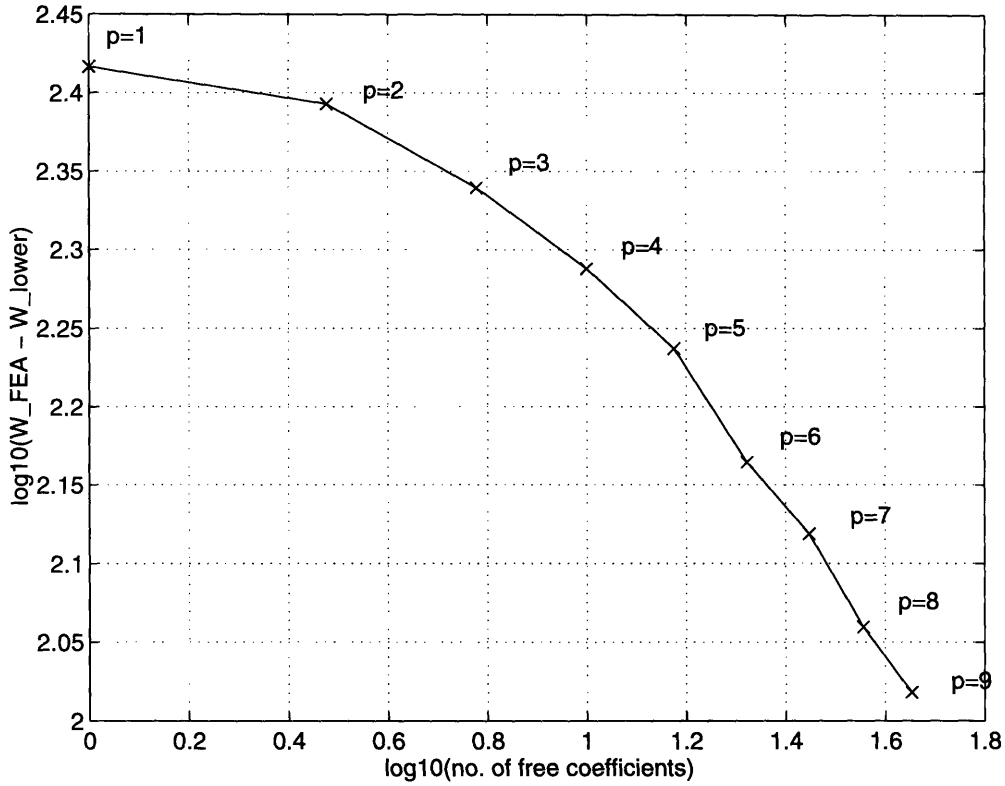


Figure 4-7: Error variation for lower “thermal energy” bound

K_1 and K_2 are found to be

$$(K_1, K_2) = (593.4717, -0.4569) \quad (4.53)$$

for the lower bound, and

$$(K_1, K_2) = (169.1999, -1.7988) \quad (4.54)$$

for the upper bound. For example, an upper bound error of $E = 105W/m$, corresponds to approximately 45 free coefficients in the lower bound calculation. To verify this, Maple V can be employed to calculate a lower bound with 45 free coefficients, yielding

$$W_{lower} = 263.918W/m. \quad (4.55)$$

This implies an error

$$E = W_{FEA} - W_{lower} = 104.237W/m \quad (4.56)$$

which is almost equal to the upper bound error of $105W/m$. A number of geometries of varying dimensions and excitations have been analyzed and the linear behavior of Figures 4-6 and 4-7 has been found to hold.

4.4 Hot Spot Temperature Estimation

The proofs of the previous section focus on the existence and calculation of bounds for the “thermal energy” of a system such as a variable reluctance motor at steady state. From the above, it cannot be concluded that the field quantities, such as $|\mathbf{q}|$ or T are bounded at a point. This is because temperature at a point is a locally determined quantity, whereas energy is globally determined. From an engineering perspective, one is not really interested in the “thermal energy” stored within the system. The hot spot of the machine is a more useful quantity, essential in determining the thermal limit of the device. This requires accurate knowledge of the temperature distribution in the motor cross-section, which is not provided and is not within the philosophy of the ADEM.

Fujita presented a theorem in the 1950s that can be employed to derive bounds to the distribution at a point [43]. Synge, Maple and Greenberg’s work in [44], [45], [46], addresses the same problem: obtaining bounds on the solution of boundary value problems and more specifically on the Dirichlet problem at any point within the region of interest. However, the method presented is not applicable to cases where the point lies on the boundary of the region. It is shown in the next section, that for the VRM thermal model adopted, the hot spot occurs on the boundary of the region under consideration. As a result, the existing methods cannot be applied in this case. A new algorithm is presented here that employs the results of the algebraic dual-energy method to estimate the value of the hot spot temperature.

4.5 VRM Hot Spot Estimation Using the ADEM

A finite element analysis study is first presented to provide more insight on the temperature distribution of the simplified VRM geometry (Figure 4-2) and determine the location of the hot spot. Following this, the ADEM is employed to obtain estimates on the hot spot temperature of the motor.

Finite Element Analysis of the VRM Thermal Model

A numerical example is considered here; its dimensions and excitation are provided in Table 4.2. Quickfield [63] is employed to determine the temperature profile for this problem. Figures 4-8, 4-9 and 4-10 provide the heat flux vector, temperature and isotherm profiles, respectively. It is clear from Figure 4-9 that the hot spot of

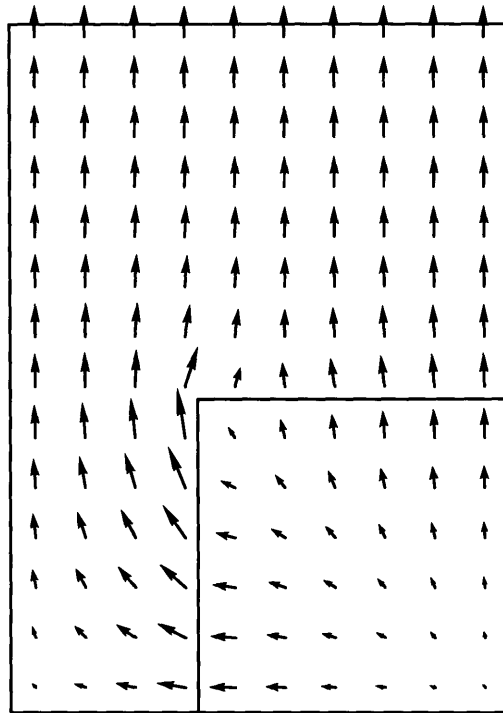


Figure 4-8: Heat flux vector plot for the simplified VRM geometry

the motor occurs at the outer corner of the winding, which is the heat source. This observation is not surprising; the temperature rise in the steel area is expected to be the least, since the thermal conductivity of steel is higher than that of the winding.

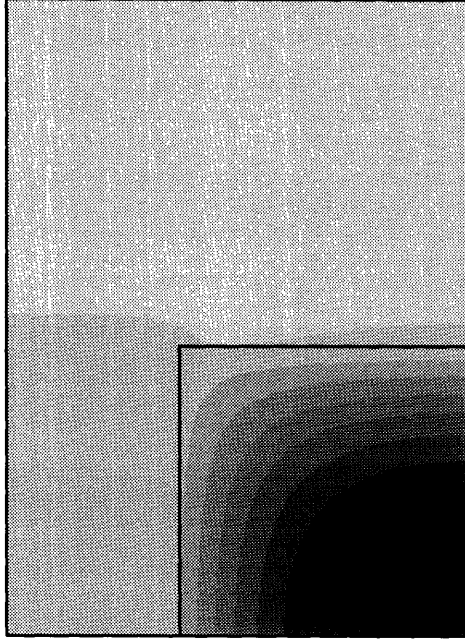


Figure 4-9: Temperature map for the simplified VRM geometry, showing a variation of 0-21.5K in steps of 2.15K. The darkest region is the hottest.

Hence, the highest temperature is expected to occur within the winding, right at the corner of the adiabatic surfaces where the heat flux cannot escape. The temperature at that corner point is found to be $T_{hot\ spot} = 21.467\ K$. The problem of obtaining estimates for this value is addressed below.

Hot Spot Estimation

Let the coordinates of the hot spot be (x^*, y^*) . For the VRM thermal problem considered here, finite element analysis of a number of geometries of different dimensions and winding areas has shown that the location of the hot spot is always at the far outer corner of the winding.

Several important observations and questions should be raised at this point. During the upper “energy” bound calculation the notion of temperature is not employed. This is because the constraint

$$\nabla \times \mathbf{M} = \mathbf{0} \tag{4.57}$$

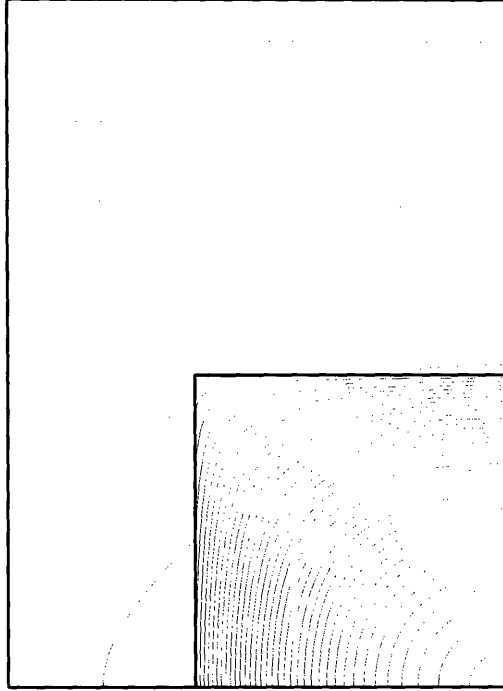


Figure 4-10: Isotherms for the simplified VRM geometry

is not imposed, and as a result, T is not defined in obtaining W_{upper} . Consequently, in considering ways to employ the algebraic dual-energy results for hot-spot bound calculations, one comes across the more subtle issue of what temperature really is in the upper bound case. In trying to overcome this problem, the basic philosophy of the method can be coupled with the thermodynamics of the physical world. More specifically, the dual-energy method considers the system as a whole. The “energy” bounds derived are bounds for the W_t of a black box, as illustrated in Figure 4-11. Moreover, for a linear physical system of thermal capacity C , a change in thermal energy (heat) ΔE will give rise to a temperature change of ΔT , so that

$$\Delta E = C \Delta T \quad (4.58)$$

Hence, one could consider the VRM thermal model as a black box with an effective thermal capacity C ; setting ΔT equal to the required hot spot temperature, ΔE provides the thermal energy stored in the system.

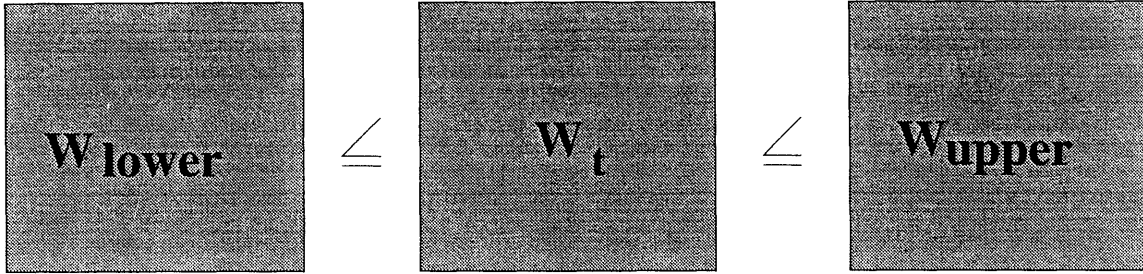


Figure 4-11: The VRM model as a black box

The observations above suggest that the ADEM “thermal energy” bounds may be employed in lieu of ΔE in an attempt to obtain bounds for the hot spot. The problem of defining temperature in the upper bound case is bypassed by considering the system as a whole. However, care should be taken at this point. The system energy in (4.58) is not the same as the “thermal energy” of the ADEM. The black box model that would be more appropriate to account for this discrepancy is

$$W_t = \frac{1}{2} \zeta T_{hot\ spot}^2 \quad (4.59)$$

This is analogous to

$$W_m = \frac{1}{2} L i^2 \quad (4.60)$$

in the magnetics case. In (4.60) the current i is known, so given upper and lower energy bounds for W_m , upper and lower bounds for the inductance L can be obtained, respectively. In (4.59), however, although upper and lower bounds are guaranteed to exist for W_t , no quantitative information on ζ is known. Moreover, (4.59) lacks the physical interpretation associated with (4.58) or (4.60), since W_t is only a numerical quantity. As a result, bounds or estimates for the hot spot temperature $T_{hot\ spot}$ cannot be easily obtained nor guaranteed. Nevertheless, the ideas and the model of (4.59) are further pursued here.

Figure 4-12 is a sample of the different geometries considered in the pursuit of hot

spot bounds and provides their corresponding hot-spot temperatures and “thermal energies” calculated using finite-element analysis. Tables 4.3, 4.4 and 4.5 summarize

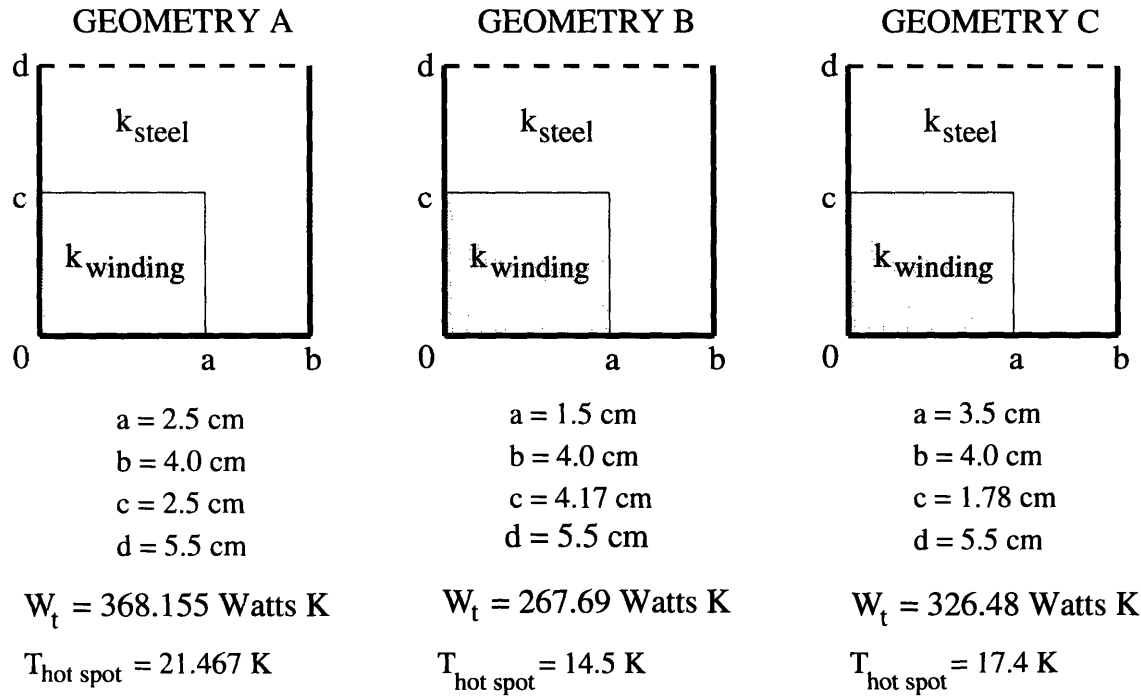


Figure 4-12: Sample of various VRM geometries considered in hot spot calculations

the results obtained for the three different geometries. “ T_L at the hot spot” in these tables is calculated by evaluating the temperature approximations T_L at the hot-spot location (x^*, y^*) . From the above results, it is apparent that $T_L(x^*, y^*)$ is a lower bound to the real hot spot $T(x^*, y^*)$, although convergence and boundedness is not guaranteed.

Based on the above observations, a simple algorithm to yield estimates to the hot spot is now given. First, following (4.59), set

$$W_{\text{lower}} = \frac{1}{2} \zeta T_{\text{hot spot},L}^2 \quad (4.61)$$

Order	W_{lower}	W_{upper}	T_L at hot spot	T_U
1	107.188	415.298	4.439	8.738
2	121.055	372.868	5.788	10.158
3	149.738	368.894	10.227	16.052
4	174.013	368.524	14.833	21.586
5	195.503	-	15.427	-
6	222.161	-	15.252	-
7	236.623	-	15.674	-
8	253.464	-	17.133	-
9	263.918	-	17.992	-

Table 4.3: Geometry A: Hot spot and “thermal energy” predictions using the ADEM

Order	W_{lower}	W_{upper}	T_L at hot spot	T_U
1	69.275	298.930	3.568	7.412
2	96.494	274.288	4.846	8.170
3	121.900	268.743	7.751	11.509
4	137.059	268.100	10.299	14.404
5	143.120	-	9.862	-
6	159.538	-	9.645	-
7	176.359	-	10.950	-
8	181.194	-	11.435	-
9	193.397	-	11.846	-

Table 4.4: Geometry B: Hot spot and “thermal energy” predictions using the ADEM

Order	W_{lower}	W_{upper}	T_L at hot spot	T_U
1	125.959	357.924	4.812	8.111
2	134.224	332.493	5.926	9.327
3	148.766	327.859	8.699	12.914
4	163.606	327.158	11.570	16.360
5	177.409	-	11.437	-
6	197.839	-	11.432	-
7	214.532	-	12.576	-
8	223.688	-	13.353	-
9	235.036	-	13.802	-

Table 4.5: Geometry C: Hot spot and “thermal energy” predictions using the ADEM

and

$$W_{upper} = \frac{1}{2} \zeta T_{hot\ spot,U}^2 \quad (4.62)$$

where $T_{hot\ spot,L}$ is the value of the temperature approximation T_L at the hot-spot location (x^*, y^*) , and $T_{hot\ spot,U}$ is the hot spot temperature corresponding to the upper bound of W_t . Dividing these two equations yields

$$\frac{W_{lower}}{W_{upper}} = \frac{T_{hot\ spot,L}^2}{T_{hot\ spot,U}^2} \quad (4.63)$$

or

$$T_{hot\ spot,U} = T_{hot\ spot,L} \sqrt{\frac{W_{upper}}{W_{lower}}}. \quad (4.64)$$

Hence, the estimated $T_{hot\ spot,U}$ essentially adopts the shape of $T_{hot\ spot,L}$, scaling it up by $\sqrt{\frac{W_{upper}}{W_{lower}}}$ and then evaluating it at the location of the hot spot.

It is important to note in (4.64) that $T_{hot\ spot,L}$, W_{upper} and W_{lower} are all determined through the application of the algebraic dual-energy method, so that (4.64) is a way of obtaining another estimate on the hot spot temperature. For the three different geometries considered above, $T_{hot\ spot,U}$ for different orders of approximation is given in Tables 4.3, 4.4 and 4.5. As the order of approximation increases, improved hot spot temperature estimates are obtained.

The algorithm obtained above is not guaranteed to provide hot spot temperature estimates of satisfactory accuracy. However, it has been successfully applied in a large number of geometries and has yielded acceptable results. It should be noted that this approach is only one avenue that could be followed in bridging the ADEM philosophy of calculating global quantities to the estimation of local quantities such as temperature. The results and conclusions drawn above apply only to the VRM thermal model considered and are strongly dependent upon the type of approximation adopted for T_L . Further research is required to remove the assumption that the hot spot location is known, and to guarantee that the value of the adopted T_L approximation at the hot spot location is always a lower bound to the real hot spot temperature.

4.6 Conclusions

In this Chapter, the algebraic dual-energy method is applied to calculate the thermal energy bounds for a simplified VRM thermal model. To do so, the analogy with electrostatic systems is employed. Analytic expressions for these bounds are easily obtained using a symbolic manipulation package, such as Maple V. The upper bound is found to converge faster to the exact solution, but its calculation is hindered by the larger number of boundary conditions that must be satisfied. The lower bound on the other hand can be obtained with a trivial, one-element approximation to the temperature throughout the geometry. The relationship between the logarithms of the error in energy and number of free coefficients is found to be algebraic, just like for the magnetics case, and can provide a criterion for bounds equidistance. From an engineering perspective, one is not really interested in the “thermal energy” stored within the system. As a result, this Chapter explores the possibility of applying the ADEM result towards the estimation of the hot spot temperature of the motor. A method is proposed that assumes prior knowledge of the hot spot location to calculate meaningful estimates on its temperature. Although the method is not entirely guaranteed, it is shown to work successfully in all cases studied.

Chapter 5

Summary, Conclusions and Suggestions for Future Work

This chapter gives a brief summary of the results and conclusions drawn from the application of the algebraic dual-energy method to the magnetic and thermal analysis of variable-reluctance motors. Suggestions for future work and research directions are provided.

5.1 Thesis Summary

This thesis explores the application of the algebraic dual-energy method (ADEM) to the magnetic and thermal analysis of the variable-reluctance motor (VRM). The motivation in considering the ADEM comes from its potential for providing both computational accuracy and speed; these are essential in design-optimization programs employed in the design and performance prediction of electric motor drives. The goal of the thesis is not the development of sophisticated design models; but given an acceptable (magnetic or thermal) model, emphasis is placed on its solution and more specifically, on the applicability and performance of the ADEM to this task.

The algebraic dual-energy method was first employed in Chapter 2 in simple problems with known analytic solutions, in order to gain a better understanding of its application, convergence behavior, and other issues associated with it. The

ADEM was then employed in the calculation of the stored magnetic energy of a simplified variable-reluctance motor geometry at the unaligned position. This was the focus of Chapter 3. By simply averaging upper and lower energy bounds, energy, and hence inductance, values were accurately computed using a small number of degrees of freedom. Analytic expressions for the bounds were obtained using Maple V, a symbolic manipulation package. The issue of equidistance of the bounds from the true solution was also addressed; this required further analysis of the rates of convergence and behavior of the bounds as the order of polynomial approximation increased. In Chapter 4, the ADEM was extended to the thermal analysis of the VRM cross-section. By employing the analogy that exists between electrostatics and steady-state heat conduction, bounds on the “thermal energy” were shown to exist and derived for several numerical examples. However, bounding this energy does not lead to bounds on the field quantities at each point in the geometry. Nonetheless, a simple algorithm was developed that uses the upper and lower “thermal energy” bounds of the ADEM, to calculate estimates for the hot spot. While not theoretically guaranteed to work, it did so in all cases studied.

5.2 Thesis Conclusions

The conclusions drawn from the application of the algebraic dual-energy method to the VRM geometry are presented in this section.

The ADEM provides an effective computational tool in the three-dimensional analysis of variable-reluctance motors. Its speed and accuracy are well suited for design-optimization programs, where initial motor design is required and it is desired to examine a large number of candidate designs. Once an optimal set of candidate designs has been obtained, three-dimensional finite element analysis can be employed as the next step in obtaining more accurate and detailed performance predictions.

The application of the algebraic dual-energy method to the VRM geometry was demonstrated in the Cartesian coordinate system and the approach was shown to provide a fast way of calculating appropriate magnetic and thermal system functionals.

However, two computational difficulties are associated with the use of polar coordinates: the equations of the stator and rotor pole sides cannot be simply described in polar form, and the polar angle θ of a point $P(x, y)$ can only be found by using inverse trigonometric functions, which are difficult to integrate analytically. The former problem is the most serious, since it gives rise to symbolic integration difficulties in the $r - \theta$ coordinate system.

In the calculation of the upper bound, the number of elements employed must be at least equal to the number of different materials and excitations present in the geometry; for the VRM minimum inductance problem, the presence of the winding excitation imposes the need for at least two elements. Two elements are also required in the “hot spot” problem since two materials of different thermal conductivities and sources are present.

Although the upper energy bounds converge faster to the exact solution, their calculation is hindered by the larger number of boundary conditions that must be satisfied. The lower bounds on the other hand can be obtained with simple, one-element approximations to the magnetic vector potential for the inductance problem, and temperature distribution for the thermal problem. The faster convergence of the upper bound can be attributed to the fact that a larger number of elements is employed in order to satisfy the larger number of boundary conditions. Moreover, the energy in this case is dependent on the correct source distribution. This is not the case for the lower bound calculations, which exhibit slower convergence rates.

Equidistance of bounds is critical to the success of the method but it is not simply guaranteed. For the simplified variable-reluctance motor geometry considered here, a posteriori error analysis employing information from the ADEM solution was used to characterize the p-convergence of the method. The rate of convergence was shown to be algebraic, implying a linear relationship between the logarithms of the error in energy and the number of free coefficients. It is this linearity that provides a criterion for bounds equidistance and yields very accurate results with very coarse approximations.

Symbolic manipulation software such as Maple V simplifies the analytic bounds

calculations considerably. The resulting bounds are functions of the problem dimensions, excitation and material properties. These expressions can be subsequently translated into C code and incorporated within a design-optimization program; this provides a fast and accurate way of extracting the minimum inductance and hot spot estimates for a VRM, avoiding dense finite element discretizations. It should be noted that the derivation of the bounds within Maple becomes more computationally involved and slow as the order of approximation increases. However, this is not a serious disadvantage since these bounds expressions need be derived only once. Then for each different design considered, the new geometry and excitation values must be substituted; the minimum inductance and hot spot values can be obtained within fractions of a second.

The field approximations considered in this thesis are polynomials in x and y . One may argue that orthogonal polynomials are a better choice, since they exhibit improved numerical properties. However, such a choice within the scope of the ADEM is strongly affected by the type and number of boundary conditions present; some types of orthogonal polynomials may not allow all pertinent boundary conditions to be satisfied. Moreover, orthogonal polynomials become advantageous when a large number of degrees of freedom is employed. The ADEM however can provide accurate results with a very small number of free coefficients.

Obtaining estimates on the hot spot temperature of the VRM is not a trivial task. The algorithm developed in this thesis is not guaranteed to work for any boundary value problem and assumes prior knowledge of the hot spot location. However, for the conservative model considered in the thesis, the type of approximations adopted, and the particular heat source distribution, the approach can provide meaningful estimates on the hot spot and was shown to work in all cases studied.

Just like with any other numerical method, the feasibility and applicability of the ADEM in VRM analysis strongly depends on two factors: the models adopted, and the computing resources available for model evaluation. In this thesis, simplified magnetic and thermal VRM models were employed. The ADEM results were evaluated against finite element analysis calculations to assess their accuracy in the particular

model solution. Comparisons with actual motor measurements will be more strongly dependent on the model, rather than the method employed for analyzing the model.

5.3 Suggestions for Future Work

A number of interesting possibilities and research challenges exist when considering further application of the algebraic dual-energy method to electric motor analysis in general, and variable-reluctance motor analysis in particular. These challenges are two-fold: challenges involved with successive improvement of the VRM minimum inductance and thermal models, and the application of the ADEM to these models; and challenges involved with applying the method to other aspects of VRM and electric motor design. Firstly, an algorithm combining symbolic integration in both Cartesian and polar coordinates would raise the integration difficulties that arise at the stator and rotor pole sides. This would allow improved geometric modeling and accuracy of results. Secondly, the thermal model could be relaxed and extended to include the airgap and the effect of air flow at different motor speeds. In addition, further research is required to remove the assumption that the hot spot location is known, and to guarantee that the value of the adopted temperature approximation at the hot spot location is always a lower bound to the real hot spot temperature. Moreover, as the capabilities of symbolic manipulation software increases, the algebraic dual-energy method can be extensively used in the calculation of the magnetization characteristics of the VRM. The model required here should take into account the presence of rotor and stator steel, as well as the linearity of the $B - H$ characteristic of the motor laminations. The application of symbolic manipulation offers an additional advantage in this case: the rotor can be allowed to “move” relative to the stator by a simple change of the geometry values within the bounds expressions. By further changing the excitation values in these expressions the $\lambda - i - \theta$ plane can be spanned. In addition, the ADEM could be employed in the estimation of the frequencies of vibration of the stator, since the vibration problem can be expressed as a strain energy/kinetic energy problem. Knowledge of these frequencies of vibration is

important in VRM design and analysis, especially in applications with strict acoustic noise emission standards [53]. Assuming a simple vibration model (such as one consisting of a circular ring [54], with the machine salient poles acting as concentrated masses), the algebraic dual-energy method can be applied to calculate bounds on the frequencies of vibration. Finally, one should not overlook the fact that the dual-energy method can be easily extended to a large number of engineering disciplines and as a result, can provide a fast, accurate and flexible alternative for the solution of boundary value problems.

Bibliography

- [1] D. E. Cameron, Ph.D. Thesis, Massachusetts Institute of Technology, to be submitted.
- [2] K. Sridhar, *Integrated Design of Electromechanical Systems*, Ph.D. Thesis, Massachusetts Institute of Technology, August 1995.
- [3] T. J. E. Miller, *Brushless Permanent-Magnet and Reluctance Motor Drives*, Oxford University Press, 1989.
- [4] T. J. E. Miller, "Switched Reluctance Drives, Tutorial Course", *IEEE IAS Conference*, 25th IAS Annual Meeting, Seattle, WA, 1990.
- [5] T. J. E. Miller, *Switched Reluctance Motors and their Control*, Magna Physics Publishing & Oxford University Press, 1993.
- [6] D. A. Torrey, *Optimal-Efficiency Constant-Speed Control of Nonlinear Variable Reluctance Motor Drives*, Ph.D. Thesis, Massachusetts Institute of Technology, March 1988.
- [7] P. Hammond, *Energy Methods in Electromagnetism*, Oxford University Press, 1986.
- [8] T. J. E. Miller, M. McGilp, "Nonlinear Theory of the Switched Reluctance Motor for Rapid Computer Aided Design", *IEE Proc.*, Vol. 137, Pt. B, No. 6, 1990, 337-347.
- [9] W. J. Gibbs, *Conformal Transformations in Electrical Engineering*, Chapman & Hall Ltd., London, 1958.

- [10] L. V. Bewley, *Two-Dimensional Fields in Electrical Engineering*, Dover Publications, Inc., New York, 1963.
- [11] P. P. Silvester, R. L. Ferrari, *Finite Elements for Electrical Engineers*, 2nd edition, Cambridge University Press, 1990.
- [12] S. R. H. Hoole, *Computer-Aided Analysis and Design of Electromagnetic Devices*, 2nd edition, Cambridge University Press, 1990.
- [13] B. Noble, "Complementary Variational Principles for Boundary Value Problems I: Basic Principles, with an Application to Ordinary Differential Equations", *MRC Technical Summary Report 473*, Mathematics Research Center, United States Army, The University of Wisconsin, November 1964.
- [14] C. Lanczos, *The variational Principles of Mechanics*, Dover Publications Inc., 4th Edition, 1970.
- [15] L. Cairo, T. Kahan, *Variational Techniques in Electromagnetism*, New York, Gordon & Breach, 1965.
- [16] K. Foster, R. Anderson, "Characteristic impedance of TEM lines by variational methods", *IEE Proc.*, Vol. 118, No. 8, August 1971.
- [17] P. Hammond, J. Penman, "Calculation of Inductance and Capacitance by Means of Dual Energy Principles", *IEE Proc.*, Vol. 123, No. 6, June 1976, 554-559.
- [18] N. Anderson, A. M. Arthurs, "A Variational Principle for Maxwell's Equations", *Int. J. Electronics*, 1978, Vol. 45, No. 3, 333-334.
- [19] N. Anderson, A. M. Arthurs, "Complementary Variational Principles for Maxwell's Equations", *Int. J. Electronics*, 1979, Vol. 47, No. 3, 229-236.
- [20] A. M. Arthurs, *Complementary Variational Principles*, Oxford University Press, 2nd edition, 1980.
- [21] N. Anderson, A. M. Arthurs, "Complementary Variational Principles for Maxwell's Equations II", *Int. J. Electronics*, 1980, Vol. 48, No. 4, 327-330.

- [22] N. Anderson, A. M. Arthurs, "Variational Principles for Maxwell's Equations II", *Int. J. Electronics*, 1981, Vol. 51, No. 1, 71-77.
- [23] J. Penman, J. R. Fraser, "Complementary and Dual Energy Finite Element Principles in Magnetostatics", *IEEE Transactions on Magnetism*, Vol. MAG-18, No. 2, March 1982, 319-324.
- [24] J. Penman, J. R. Fraser, "Error Bounded Formulations in Electromagnetism", *Polymodel 6*, Conf. on Math. Modelling, Newcastle, May 1983, 53-62.
- [25] P. Hammond, T. D. Tsiboukis, "Dual Finite-Element Calculations for Static Electric and Magnetic Fields", *IEE Proc.*, Vol. 130, Pt. A, No. 3, May 1983, 105-111.
- [26] J. Penman, J. R. Fraser, "Dual and Complementary Energy Methods in Electromagnetism", *IEEE Transactions on Magnetism*, Vol. MAG-19, No. 6, November 1983, 2311-2316.
- [27] J. Penman, J. R. Fraser, J. H. Smith, M. D. Grieve, "Complementary Energy Methods in the Computation of Electrostatic Fields", *IEEE Transactions on Magnetism*, Vol. MAG-19, No. 6, November 1983, 2288-2291.
- [28] J. Penman, J. R. Fraser, "Unified Approach to Problems in Electromagnetism", *IEE Proc.*, Vol. 131, Pt. A, No. 1, January 1984, 55-61.
- [29] P. Hammond, M. C. Romero-Fuster, S. A. Robertson, "Fast Numerical Method for Calculation of Electric and Magnetic Fields based on Potential-Flux Duality", *IEE Proc.*, Vol. 132, Pt. A, No. 2, March 1985, 84-94.
- [30] P. Hammond, Z. Qionghua, "Calculation of Poissonian Fields by Means of the Method of Tubes and Slices", *IEE Proc.*, Vol. 132, Pt. A, No. 4, July 1985, 149-156.
- [31] P. Hammond, D. Baldomir, "Dual Energy Methods in Electromagnetism Using Tubes and Slices", *IEE Proc.*, Vol. 135, Pt. A, No. 3, March 1988, 167-172.

- [32] J. A. H. Rikabi, C. F. Bryant, E. M. Freeman, "Complementary Solutions of Linear and Nonlinear Magnetostatic Problems", *IEE Proc.*, Vol. 135, Pt. A, No. 7, September 1988, 433-447.
- [33] J. A. H. Rikabi, C. F. Bryant, E. M. Freeman, "Complementary Solutions of Electrostatic Field Problems", *IEEE Transactions on Magnetics*, Vol. 25, No. 6, November 1989, 4427-4442.
- [34] D. Baldomir, P. Hammond, "Geometrical Formulation for Variational Electromagnetics", *IEE Proc.*, Vol. 137, Pt. A, No. 6, November 1990, 321-330.
- [35] J. A. H. Rikabi, C. F. Bryant, E. M. Freeman, "On the Solvability of Magnetostatic Vector Potential Formulations", *IEEE Transactions on Magnetics*, Vol. 26, No. 5, September 1990, 2866-2874.
- [36] D. A. Lowther, E. M. Freeman, "Upper and Lower Bounding - an Equivalent Circuit Viewpoint", personal communication.
- [37] J. K. Sykulski, "Computer Package for Calculating Electric and Magnetic Fields Exploiting Dual Energy Bounds", *IEE Proc.*, Vol. 135, Pt. A, No. 3, March 1988, 145-150.
- [38] Z. J. Cendes, D. N. Shenton, "Adaptive Mesh Refinement in the Finite Element Computation of Magnetic Fields", *IEEE Transactions on Magnetics*, Vol. MAG-21, No. 5, September 1985, 1811-1816.
- [39] M. Tolikas "Conformal Mapping Applications in Electromagnetics", *Area Exam Report*, E.E.C.S. Department, M.I.T, February 1994.
- [40] Maple V, Waterloo Maple Software, 160 Columbia Street West, Waterloo, Ontario, N2L 3L3, Canada.
- [41] H. A. Haus, J. R. Melcher, *Electromagnetic Fields and Energy*, Prentice-Hall International Inc., 1989, pp. 359-360.

- [42] M. Zahn, *Electromagnetic Field Theory: a problem solving approach*, R. E. Krieger Publishing Company, Inc., 1987, pp. 455-456.
- [43] H. Fujita, "Contribution to the Theory of Upper and Lower Bounds in Boundary Value Problems", *Journal of the Physical Society of Japan*, Vol. 10, No. 1, January 1955, 1-8.
- [44] C. G. Maple, "The Dirichlet Problem: Bounds at a Point for the Solution and its Derivatives", *Quarterly of Applied Mathematics*, Vol. VIII, No. 3, October 1950, 213-228.
- [45] J. L. Synge, *The Hypercircle Method in Mathematical Physics*, Cambridge University Press, 1957, pp. 155-168.
- [46] J. L. Nowinski, *Applications of Functional Analysis in Engineering*, Plenum Press, New York, 1981, pp. 153-165.
- [47] T. D. Tsiboukis, *Εφαρμογή Αμεσων Μεθόδων της Συναρτησιακής Αναλύσεως στον Υπολογισμό Αντιστάσεων, Αυτεπαγωγών και Χωρητικότητων*, Ph.D. Thesis, Aristotelio University of Thessaloniki, Greece, 1980.
- [48] M. Tolikas, J. H. Lang, J. L. Kirtley Jr., "Algebraic Dual-Energy Method Magnetic Analysis with Application to Variable Reluctance Motor Design", to be presented at the 1995 *IEEE-IAS Annual Meeting*, Orlando, Florida, 1995.
- [49] I. Babuska, O. C. Zienkiewicz, J. Cago, E. R. de Oliveira, *Accuracy Estimates and Adaptive Refinements in Finite Element Computations*, John Wiley & Sons, 1986.
- [50] B. Szabo, I. Babuska, *Finite Element Analysis*, John Wiley & Sons, 1991.
- [51] G. Strang, G. J. Fix, *An Analysis of the Finite Element Method*, Prentice-Hall, Inc., 1973.
- [52] J. H. Lang, "Lower and Upper Bounds for Three-Dimensional Linear Static Resistances, Capacitances and Inductances", M.I.T, March 1993.

- [53] D. E. Cameron, *Origin and Reduction of Acoustic Noise in Variable-Reluctance Motors*, MSc. Thesis, Massachusetts Institute of Technology, January 1990.
- [54] S. Timoshenko, *Vibration Problems in Engineering*, D. Van Nostrand Company Inc., 2nd edition, 1937, pp. 405-406.
- [55] R. K. Singal, K. Williams, "A Theoretical and Experimental Study of Vibrations of Thick Circular Cylindrical Shells and Rings", *Journal of Vibration, Acoustics, Stress and Reliability in Design*, October 1988, Vol. 110, pp. 533-537.
- [56] R. S. Girgis, S. P. Verma, "Method for Accurate Determination of Resonant Frequencies and Vibration Behaviour of Stators of Electrical Machines", *IEE Proc.*, Vol. 128, Pt. B, No. 1, January 1981, pp. 1-11.
- [57] S. P. Verma, R. S. Girgis, "Experimental Verification of Resonant Frequencies and Vibration Behaviour of Stators of Electrical Machines, Part 1-Models, Experimental Procedure and Apparatus", *IEE Proc.*, Vol. 128, Pt. B, No. 1, January 1981, pp. 12-21.
- [58] S. P. Verma, R. S. Girgis, "Experimental Verification of Resonant Frequencies and Vibration Behaviour of Stators of Electrical Machines, Part 2-Experimental Investigations and Results", *IEE Proc.*, Vol. 128, Pt. B, No. 1, January 1981, pp. 22-32.
- [59] S. J. Yang, A. J. Ellison, *Machinery Noise Measurement*, Oxford University Press, 1985.
- [60] J. H. Lienhard, *A Heat Transfer Handbook*, Prentice-Hall Inc., 1981, pp. 40-52.
- [61] F. M. White, *Heat Transfer*, Addison Wesley Publishing Co., 1984.
- [62] J. G. Kassakian, M. F. Schlecht, G. C. Verghese, *Principles of Power Electronics*, Addison-Wesley Publishing Co., 1991.
- [63] QuickField, Tera Analysis, 1994, 17114 Bircher Street, Granada Hills, CA 91344.

- [64] "Thermal and Electrical Properties of Selected Packaging Materials", *Application Bulletin*, Burr-Brown Corporation, 1991.
- [65] F. J. Vallese, *Design and Operation of High-Power Variable Reluctance Motor Based Drive Systems*, Ph.D. Thesis, Massachusetts Institute of Technology, March 1985, pp 76.
- [66] R. Krishnan, R. Arumugam, J. F. Lindsay, "Design Procedure for Switched Reluctance Motors", *IEEE Transactions on Industry Applications*, vol. 24, no. 3, May/June 1988, pp. 456-461.